12-2020

Pre-Eruptive Evolution of Izu-Bonin Boninite Melts: Mixing, Cooling, and Crystallization

Jesse L. Scholpp
Utah State University

PRE-ERUTPIVE EVOLUTION OF IZU-BONIN BONINITE MELTS: MIXING, COOLING, AND CRYSTALLIZATION

by

Jesse L. Scholpp

A thesis submitted in partial fulfillment
of the requirements for the degree

of

MASTER OF SCIENCE

in

Geology

Approved:

_____	_____
John W. Shervais, Ph.D.	Jeffrey G. Ryan, Ph.D.
Major Professor	Committee Member
_____	_____
Alexis K. Ault, Ph.D.	Dennis L. Newell, Ph.D.
Committee Member	Committee Member

_____
D. Richard Cutler, Ph.D.
Interim Vice Provost for Graduate Studies

UTAH STATE UNIVERSITY
Logan, Utah

2020

ABSTRACT

Pre-Eruptive Evolution of Izu-Bonin Boninite Melts: Mixing, Cooling, and Crystallization

by

Jesse L. Scholpp, Master of Science

Utah State University, 2020

Major Professor: John W. Shervais
Department: Geosciences

Constraining the melt evolution of boninite lavas is critical for understanding volcanism during subduction initiation. Boninite lava is found in fore-arc settings across the Izu-Bonin Mariana (IBM) subduction system, which represents the convergent margin between the Pacific and Philippine tectonic plates. Previous studies, based on ocean drilling, dredging, and submersible dives, conclude that IBM boninite volcanism follows the eruption of fore-arc basalts (FAB), beginning with eruptions from axial spreading centers with a later transition to proto-arc volcanism. Many of these earlier studies focused primarily on their unique trace element chemistry, which document fluid and melt fluxing of a highly depleted mantle wedge.

This study presents crystallization textures, mineral chemistry, interstitial glass and melt inclusion chemistry, elemental maps of phenocrysts, thermobarometry, and crystal

fractionation models for boninite lavas recovered during International Oceanic Discovery Program (IODP) Expedition 352. Crystal textures, mineral chemistry, and elemental maps suggest that boninite melts experience multiple mixing and undercooling events prior to eruption. Mixing events occur within a composite magma chamber, which contains melt lens, cumulate pile, and loosely-bound crystal mush zone. Undercooling occurs as magmas ascend through the crystal mush, between mixing events as the magma chamber cools, and during eruptions. Unique olivine and pyroxene crystal zoning patterns observed in some lavas indicate that magma mixing events occurred shortly before eruption. We propose that these mixing events destabilize the magma chamber, initiating melt devolatilization, disequilibrium crystallization, and the eruption.

Interstitial glass and melt inclusion compositions range from boninite to dacite, indicating boninite melts undergo substantial crystallization before eruption. Crystal fractionation models suggest that melt composition within the chamber range from boninite to high-Mg andesite (HMA). Melt compositions only reach andesite and dacite during the eruptive process. Multiple fractionation paths suggest that boninite subgroups follow unique crystallization paths based on source composition and architecture of the magmatic system. Thermobarometric calculations indicate that melts crystallize at temperatures of 1000-1200 ^{o}C within the magma chamber, which ranges in depth from the middle to base of the crust.

We suggest that low-Si boninite (LSB) melts erupt from a magmatic system similar to those observed at mid-ocean ridges. In contrast, high-Si boninite (HSB) melts erupt from multiple off-axis eruptive centers. Future major and trace element and isotopic

analysis will further constrain the differences between LSB and HSB melt evolution. Further analysis of mineral hosted melt inclusions will allow us to determine the evolution of subduction-related fluids and volatiles throughout boninite volcanism.

(173 pages)

PUBLIC ABSTRACT

Pre-Eruptive Evolution of Izu-Bonin Boninite Melts:

Mixing, Cooling, and Crystallization

Jesse L. Scholpp

Subduction is the geologic process in which one tectonic plate moves beneath another as it sinks into the Earth's mantle. Subduction initiation in the Izu-Bonin Marianas system is the result of a gravitational failure during which one tectonic plate (the Pacific plate) spontaneously sinks beneath another (the Philippne Sea plate). Fluids released by the sinking plate that caused the overlying mantle to melt by reducing its meltimg temperature, forming the Izu-Bonin Mariana island arc system.

The resulting melts initially have the chemical compositions that are rich in silica and magnesia, and highly depleted in other elements, refered to a boninite or high-Mg andesite. The goal of this thesis is to examine the chemical evolution of boninite lavas as they ascend from the mantle to the surface. This study intergrates observations of crystal chemistry and textures, with models that show how crystallization alters the chemistry of the melt. Melts begin crystallizing near the base of the crust (≈7-10 km below the surface) and continue to crystallize as they ascend through the crust and into a magma chamber. Separate melts interact and mix within this magma chamber, forming a single hybridized melt. In some cases, this mixing results in the eruption of boninite lavas.

Our results also indicate that low-silica boninite and high-silica boninite come from mantle sources with different chemical compositions. It is unclear whether there

was mantle source or whether the mantle source is just chemically evolving as melting continues. This question, along with questions on the chemical evolution of subduction fluids, will be examined during future chemical studies of these boninite lavas.

Acknowledgements

First, I would like to thank my advisor, Dr. John W. Shervais, for giving me the opportunity to continue my research on boninite chemistry while pursuing my graduate degree at Utah State University. I am also immensely grateful to Dr. Jeffrey G. Ryan, who has been an incredible mentor throughout my undergraduate and graduate degree pursuits. John and Jeff have been amazing advisors throughout my time in geoscience and have undoubtedly made me a much better scientist. I would also like to thank Dr. Alexis Ault and Dr. Dennis Newell, who have both been awesome mentors during my time at Utah State University. Alexis and Dennis have certainly improved my writing and critical thinking skills and were always available when I needed advice from them, which I can't thank them enough for.

Acknowledgments are due to those outside my committee for their assistance in data collection. Dr. Ciprian Stremtan from Teledyne CETAC Technologies and Dr. Martin Rittner from TOFWERK AG have been extremely helpful with the collection of chemical data on olivine and pyroxenes, which resulted in the creation of incredibly informative elemental maps. I would also like to thank Dr. Nick Bulloss of Boise State University, who provided much needed assistance during the collection of chemical data at the Boise State Center for Material Characterization (CAES).

The research was supported by NSF grants OCE-1558855 and DUE-1323275 to Jeff Ryan and OCE-1558689 to John Shervais. I would also like to acknowledge the support from Geologic Society of American MGVP division Lipman student research award.

Finally, I would like to thank my friends Stephen Hill, Kenneth Kehoe, Clay Barlow, Andrew Lonero, Bradford Mack, Aaron Lutz, and Rachel Kubina for providing moral support throughout my degree. I would also like to thank my mom, dad, and sister for supporting me and allowing me to vent during the stressful periods throughout my degree. Last but certainly not least, I would like to thank Kelly Bradbury, Hollie Richards, and Ellen Imler for keeping me on track and organized throughout my degree.

Jesse L. Scholpp

CONTENTS

LIST OF TABLES

Page

LIST OF FIGURES

Page

CHAPTER I

1. INTRODUCTION

1.1. The Izu-Bonin Marinas (IBM) Subduction System

The IBM subduction system comprises the Pacific Plate and the overriding Philippine Sea Plate (Figure 1.1). The system stretches over 3,000 km from the Izu Peninsula in Japan to the island of Palau. Subduction began around 52 Ma (Ishizuka et al. 2011a; Reagan et al. 2013) when the westernmost edge of the Pacific plate foundered along a transform fault, and seafloor spreading began to form the upper Philippine Sea plate (e.g., Wu et al. 2016).

Remnants of older terranes are found trapped within the upper plate. The oldest rocks associated with the IBM system are Cretaceous and located in the Huatung Basin on the west side of the West Philippine Basin (Hickey-Vargas et al. 2008) and the Palau Basin at the southern end of the Philippine plate (Taylor and Goodliffe 2004). Cretaceous remnant island arcs and ocean islands make up the Oki-Diato and Diato Ridges and the Amami Plateau in the northern West Philippine Basin (Hickey-Vargas 1998, 2005; Ishizuka et al. 2011b).

There are multiple back-arc basins associated with subduction in the IBM system, the oldest of which is the West Philippine Basin, which opened between ~55-52 Ma and ~30 Ma (Deschamps and Lallemand 2002; Savov et al. 2005; Ishizuka et al. 2011a, 2013). A new back-arc spreading center initiated ~25 Ma, creating the Parece Vela and Shikoku back-arc basins, contemporaneous with the collision of the Philippine Sea Plate with south-western Japan 25-14 Ma (Wu et al. 2016). This new back-arc spreading

system formed by splitting the current active arc, leaving the Kyushu-Palau ridge remnant arc (Mrozowski and Hayes 1979; Okino et al. 1998; Ishizuka et al. 2011a). The youngest back-arc basin is the Mariana Trough, which began spreading ~6 Ma and resulted in the separation of the active Mariana volcanic arc from the West Mariana Ridge remnant arc (Fryer 1995).

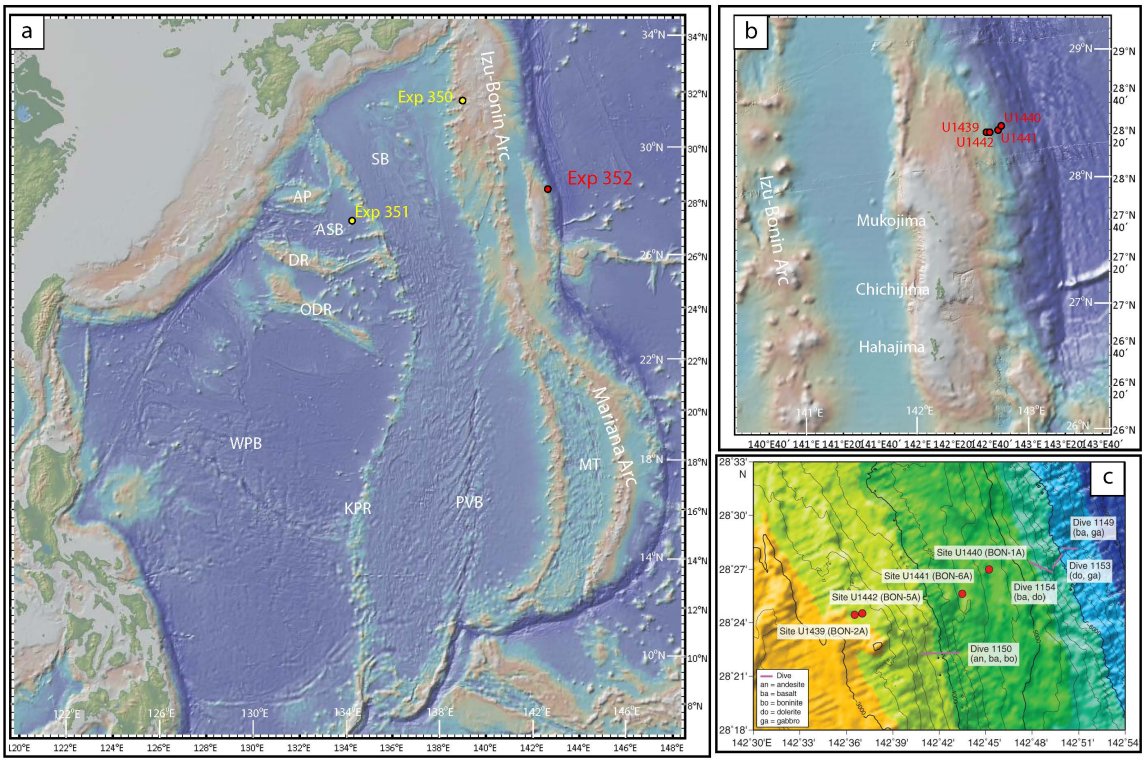

Figure 1.1
Location maps (a, b, c) based on Reagan et al. (2015) and Shervais et al. (2019). (a) The Izu-Bonin-Mariana arc system in the western Pacific and the Philippine Sea Plate. Yellow circles represent Expeditions 350 and 351 locations. Red circles represent Expedition 352 locations. KPR= Kyushu-Palau Ridge, PVB= Parece-Vela Basin, MT= Mariana Trough, WPB= West Philippine Basin, SB= Shikoku Basin, AP= Amami Plateau, ASB= Amami-Sankaku Basin, DR= Diato Ridge, ODR= Oki-Diato Ridge. (b) Location of drill sites U1439, U1440, U1441, U1442 in relation to the Bonin Islands on the Ogasawara Plateau. (c) Drill sites for IODP Expedition 352 from (Reagan et al. 2015) and dive sites of Shinkai 6500 (Ishizuka et al. 2011).

Fore-arc crust formed during subduction initiation in the early Eocene is preserved in the IBM fore-arc (Stern et al. 2012; Reagan et al. 2017), despite this long history of arc rifting and back-arc basin formation. This crust pre-dates the establishment of an active volcanic arc and subsequent back-arc basins and preserves a magmatic, structural, and tectonic record of the subduction initiation process. The magmatic record includes both boninite, a highly-refractory volcanic rock unique to subduction systems characterized by high-MgO and high-SiO2, and fore-arc basalt (FAB), Mid-Ocean Ridge Basalt-like (MORB) lava that erupts just before the onset of boninite volcanism (Reagan et al. 2010, 2017)

1.2. IODP Expedition 352

IODP Expedition 352 was located in the southern Izu-Bonin fore-arc, east of the Bonin Islands, and close to the active trench (Reagan et al. 2015). The primary objectives of IODP Expedition 352 were to (1) obtain a high-fidelity record of magmatic evolution during subduction and early arc development, (2) test the hypothesis that fore-arc basalts erupt prior to boninitic lavas, and to understand the chemical gradients across the transition, (3) determine how mantle melting processes evolve during and after subduction initiation, and (4) test the hypothesis that fore-arc created during subduction initiation is the birthplace of supra subduction zone ophiolites (Reagan et al., 2015).

Four drill sites (U1439, U1440, U1441, and U1442) were targeted for the expedition based on the results of dredging and submersible dives. The dredging and submersible dives revealed that FAB are exposed in the trench wall, topographically beneath boninites (Ishizuka et al. 2011b). Two drill sites advanced into boninites (Sites

U1439 and U1442), and two into FAB (Sites U1440 and U1441), with 20-30% core recovery in the boninites, and ≤10% in the basalts. In FAB site (U1440) and boninite site (U1439) rocks with diabasic textures were penetrated, indicating that the transition from tholeiite to boninite likely reflects a shift in the locus of magmatism, at odds with the ostensibly vertical basalt-to-boninite sequences encountered in the Troodos ophiolite (Reagan et al. 2017).

Although sites U1439 and U1442 are less than 1 km apart, they reflect remarkably different boninitic stratigraphies. Hole U1442A is dominated by Low-Si boninite (LSB), and boninitic differentiates (terminology after Reagan et al. 2015). These occur as lava flows and hyaloclastites with a sequence of High-Si boninite (HSB) hyaloclastites and lava flows in the uppermost stratigraphic section. HSB are mineralogically and chemically similar to boninites found on Chichijima and other IBM sites (e.g., Umino 1986; Arculus et al. 1992; Pearce et al. 1992; Dobson et al. 2006). In contrast, Site U1439 (U1439A and U1439C) reflects a greater lithologic diversity, with diabasic rocks that appear to represent boninite feeder dikes overlain by LSB and boninite differentiates. LSB is separated from the overlying HSB by a layer of what was described as “basaltic” boninite (Reagan et al. 2015). Also evident in the U1439C cores are what were described as “magma mingling” textures, interpreted as intercalated evolved and primitive boninitic melts (Reagan et al. 2015). Indicating that the generation and evolution of the Expedition 352 boninitic magmas are spatially and chemically complex, supporting observations by Cameron et al. (1983), Umino (1986), and Dobson et al. (2006).

Reagan et al. (2015, 2017) conclude that subduction initiation begins with

voluminous melting and production of FAB, erupting from a persistent magma chamber, much like MORB. As the subduction system evolves and the subducting plate begins to devolatilize, boninitic magmas are produced. The boninite sequence starts with the eruption of LSB, which likely begins to erupt from the magma chambers, similarly to FAB. The eruptive sequence transitions to an off-axis magmatic system as the subduction system continues to evolve, and fore-arc spreading decreases. The production of HSB begins as spreading continues to decrease. HSB continues to erupt as the fore-arc evolves, eventually transitioning to focused proto-arc volcanism, resulting in an embryonic volcanic arc. Evidence for this process is presented in Ishizuka et al. (2006), older HSB transition into younger tholeiitic and calc-alkaline volcanics, which are typical of island arc systems, on Chichijima.

$^{40}Ar/^{39}Ar$ geochronology on samples from IODP Expedition 352 shows that subduction initiation and fore-arc spreading began between ~52.5 and ~51.9 Ma with the eruption of FAB, LSB (Reagan et al. 2019). Fore-arc spreading ceased between ~51.27 and ~50.33 Ma with the transition of LSB into off-axis HSB volcanism. Using these dates, Reagan et al. (2019) calculate a spreading half-rate for the FAB and LSB >37 mm/yr. Ishizuka et al. (2006) conclude that HSB volcanism in the Bonin Islands occurred between ~48 and ~46 Ma and transitioned into arc tholeiites and calc-alkaline lavas.

1.3. Fore-Arc Crust

The early crust, which formed in the IBM system, consisted of two volcanic rock types, FAB and boninites, along with their primitive and evolved end-members. FAB is named after the type locality where they were first discovered in the IBM fore-arc, to

distinguish their depleted chemical composition relative to MORB and BAB. This depleted character is shown by lower high field strength element (HFSE) and light rare earth elements (LREE) concentrations relative to MORB, and lower Mg, Ni and Zr concentrations relative to BAB (e.g., Hickey-Vargas 2018; Shervais et al. 2019). Reagan et al. (2010) conclude that FAB is the most abundant igneous rocks in the Mariana fore-arc. The latter conclusion is supported by the conclusion that FAB in the Marianas is directly related to basalts found in the Izu (Debari et al. 1999) and Bonin (Ishizuka et al. 2011b) fore-arcs.

Shervais et al. (2019) calculate olivine-melt equilibration temperatures (Lee et al. 2009) for Expedition 352 FAB of ~1400ºC and pressures between 1.4-1.6 GPa (46-53 km). FAB may be the product of the earliest magmatic response to subduction initiation, created by upwelling and voluminous decompression melting of the upper mantle (Reagan et al., 2015, 2017, 2019; Shervais et al. 2019). This voluminous melting depletes the upper mantle wedge beneath the infant arc system that results in mantle conditions necessary for the formation of boninite melts.

Boninites are mafic to intermediate volcanic rocks with high concentrations of Mg (>8 wt%) and low concentrations of incompatible elements (Bloomer and Hawkins 1987; Taylor et al. 1994; Reagan et al. 2015, 2017). Boninite lavas form via the fluid-fluxed melting of a depleted harzburgitic mantle source (Cameron et al. 1979, 1983; Hickey and Frey 1982; Cameron 1985; Kyser et al. 1986; Pearce et al. 1992; Taylor et al. 1994; Page et al. 2008, 2009). Li et al. (2013) describe Izu-Bonin boninite and differentiates from Hahajima seamount occurring in association with adakites, which point to high-

temperature conditions and melting of the subducting slab (e.g., Yogodzinski et al. 1995, 2015; Gazel et al. 2015). Lee et al. (2009) calculate equilibration temperatures for boninites from the IBM system between 1150 and 1250ºC with pressures between 0.5 and 1.2 GPa (20-40 km), assuming 5 to 7 wt. % H_2O in the mantle.

Boninites are named after their type locality in the Bonin Islands. They are commonly found in western Pacific arc systems such as the IBM system and Tonga-Kermadec arc system (Dietrich et al. 1978; Bloomer et al. 1979; Meijer 1980; Meijer et al. 1982; Crawford 1989; Arculus et al. 1992; Dobson et al. 2006; Meffre et al. 2012) and are observed actively erupting in the Lau Basin (Falloon and Crawford 1991; Falloon et al. 1992; Resing et al. 2011). Boninites are also found in ophiolites such as Troodos (Cyprus), Samail (Oman), Thetford Mines (Canada), Betts Cove (Canada), and Koh (New Caledonia) (Cameron 1985; Kyser et al. 1986; Meffre et al. 1996; Bedard et al. 1998; Wyman 1999; Ishikawa et al. 2002, 2005; Page et al. 2008, 2009).

1.4. Petrologic Studies on Boninites and FAB

Although Johannsen (1937) reported on the high Mg/high-Si volcanic rocks in the Bonin (Ogasawara) Islands, petrologic studies of these lavas did not occur until much later (e.g., Kuroda and Shiraki, 1975). Hickey and Frey (1982) and Cameron et al. (1983) geochemically examined Chichijima island boninites, and the first full petrologic study was performed by Umino (1986). Unimo (1986) distinguished two major types and five subtypes of Chichijima boninite and argued for a dynamic magma chamber with the mixing of more- and less-evolved boninitic magmas to produce at least one of the lava subtypes, based in part on zoned pyroxene crystals. Dobson et al. (2006) conducted an

extensive study of the Chichijima volcanics, documenting related rock types ranging from Mg-rich boninite to rhyolite, and the presence of high-Ca clinopyroxene in all the Chichijima volcanic rock types.

Reagan et al. (2015, 2017) briefly discuss the mineral assemblages seen in expedition 352 boninites, stating typical phenocryst assemblage in boninites include enstatite and olivine containing Cr-spinel inclusions, with later-formed acicular crystals of low-Ca clinopyroxene (clinoenstatite to pigeonite) in a glassy or crystalline matrix. Evolved boninite differentiates may contain high-Ca clinopyroxene (augite), plagioclase, and magnetite. These mineral assemblages are similar to those described in other studies of boninite lavas (Umino 1986; Dobson et al. 2006). FAB from expedition 352 is petrologically similar to other FAB from the IBM system (Reagan et al. 2015). FAB lavas are primarily aphyric; however, when crystals are present, they consist of plagioclase, clinopyroxene, and magnetite with rare olivine phenocrysts in primitive FAB (Shervais et al. 2019).

1.5. Magma Mixing/Mingling

Magma mixing is regarded as an important petrologic process in mid-ocean ridges and volcanic arcs (Anderson 1976; Langmuir et al. 1978; Mcbirney 1979; Rhodes et al. 1979; Blake 1981; Hibbard 1981; Gerlach and Grove 1982; Sakuyama 1984; Sparks and Marshall 1986; Sinton and Detrick 1992; Humphreys et al. 2006; Ohba et al. 2007; Streck et al. 2007), with recent work suggesting mixing also affects intracontinental hot spot volcanism (Stelten et al. 2013). The processes which cause and control magma mixing/mingling have been studied most extensively at mid-ocean ridges, with more

recent work being to focus on other systems.

Mid-ocean ridge magma chambers were previously thought of as large, mostly molten, “steady-state” chambers (Cann 1974; Pallister and Hopson 1981; Stakes et al. 1984; Nicolas et al. 1988). However, petrologic studies (Langmuir et al. 1986; Bloomer et al. 1989; Sinton et al. 1991; Sinton and Detrick 1992; Costa et al. 2010) conclude that mid-ocean ridge magma chambers are likely composite magma chambers with large crystal mush zones and smaller lenses of molten magma, as the petrologic variations and mixing evidence observed at mid-ocean ridges, are difficult to produce in large well-mixed chambers. Relationships between spreading rate and the diversity of magmas created at mid-ocean ridges have also been observed, with slow to intermediate spreading ridges (<80 mm/yr) exhibiting the greatest magmatic diversity (Dungan and Rhodes 1978; Rhodes et al. 1979; Flower 1980; Sinton and Detrick 1992). The increased magmatic diversity is attributed to lower volumes of magma entering these slower systems, which can fractionate over more extended periods and mix with other magmatic lenses in the crystal mush. As a result, mixing is most evident at slow-spreading ridges, where magmas are more fractionated prior to mixing.

Magma mixing in volcanic arc systems is a more complex process than mixing at mid-ocean ridges; thus it is more difficult to determine the cause of mixing (highlighted by Streck et al. (2007) and the responses of Kelemen and Yogodzinski (2007) and Barr et al. (2007)). This complexity is due to the presence of multiple magma chambers/melt lenses and various magmatic sources to consider, including the mantle wedge, overlying continental or oceanic crust, and the subducting slab. The complex nature of melt

generation and mixing at volcanic arcs has led to the debate on how andesitic magma is generated (Tatsumi 2001; Tatsumi and Hanyu 2003; Ohba et al. 2007; Reubi and Blundy 2009; Kent et al. 2010; Ruprecht and Plank 2013; Laumonier et al. 2014; Leeman and Smith 2018). Processes that may generate andesite magmas include fractionation of a mafic melt, partial melting of the subducting slab, partial melting of a depleted mantle wedge, mixing of partial melts with the mantle wedge, and mixing of mafic and felsic magmas in the crust. However, the work Yogodzinski et al. (1994, 1995) on andesites from the Aleutian Islands, indicate that the processes which produce andesitic magmas likely vary depending on other geologic factors.

1.6. Signs of Magma Mixing/Mingling

Magma mixing/mingling can create multiple signatures in igneous rocks, which depend on the scale of observation. The most obvious of these mixing/mingling signatures are mafic enclaves in plutons and homogenizing magma textures (Castro et al. 1990; Dorais et al. 1990; Chen et al. 2009; De Campos et al. 2011; Laumonier et al. 2014; Rossi et al. 2019). These textures are common in plutonic bodies associated with collisional boundaries and subduction systems; however, they are rare in lavas. Laumonier et al. (2014) suggest that these textures are the result of magmas that interact but did not to homogenize. The ability of magmas to homogenize with one another is controlled by the viscosity, temperature, time spent in contact, volatile content, crystal abundances, and crystal sizes (Laumonier et al. 2014).

Signatures of magma mixing are evident in whole rock, melt inclusion, and mineral chemistries of igneous rocks. Whole-rock chemical trends suggestive of magma

mixing processes usually show up in the trace element concentrations and isotope ratios (Langmuir et al. 1978; Anderson 1982; Carr et al. 1990; Stelten et al. 2013). The presence of these trends suggest that the interacting magmas had completely homogenized prior to eruption. In addition to indicating that mixing has occurred, these chemical trends can also reveal which magmas are mixing, what the source of each magma is, and how much fractionation has occurred in each magma (Kay 1984; Arculus and Powell 1986).

Chemical mixing trends can occur in igneous rocks, which also contain crystals with melt inclusions or crystals that exhibit zoning. Melt inclusions can also reveal a complex mixing history with major and trace element concentrations that do not match the host rock chemistry (Anderson 1976; Conrad et al. 1983; Reubi and Blundy 2009). Plagioclase, olivine, and pyroxene crystals are commonly analyzed in mineral zoning studies which focus on how zoning relates to open-system magmatic processes (Costa and Dungan 2005; Humphreys et al. 2006; Streck et al. 2007; Streck 2008; Costa et al. 2010; Kahl et al. 2011, 2013). Although these open system processes are often related to magma mixing, it can also be associated with the eruptive sequence and magma ascent (Blundy and Cashman 2005; Blundy et al. 2006; Crabtree and Lange 2010; Waters and Lange 2017).

1.7. Mineral Zoning

Plagioclase is the most common mineral that exhibits zoning in igneous rocks. This zoning is typically manifested as oscillatory (oscillating layers of primitive and evolved crystal) or patchy (patches of primitive or evolved crystal) in nature. However,

zoning in plagioclase does not always indicate magma mixing has occurred, as oscillatory zoning can form as the result of magmatic degassing (Blundy and Cashman 2005; Blundy et al. 2006; Humphreys et al. 2006; Hattori and Sato 2015). Some studies have also suggested oscillatory zoning could also be related to sluggish diffusion kinetics near the crystal interface during periods of rapid crystallization (Ghiorso 1987; L'Heureux and Fowler 1996). This is why mineral textures such as sieve texture, resorbed zones, and patchy zoning, which are the result of disequilibrium reactions between plagioclase crystals and the host melt that require mixing to occur, are considered better indicators of magma mixing with regards to plagioclase (Pearce 1994; Humphreys et al. 2006; Streck 2008).

Although less common, olivine and pyroxene crystals are also known to exhibit zoning as a result of open-system magmatic processes (Sakuyama 1979; Barton et al. 1982; Umino 1986; Costa and Chakraborty 2004; Costa and Dungan 2005; Tomiya and Takahashi 2005; Ohba et al. 2007; Streck et al. 2007; Streck 2008; Kahl et al. 2011, 2013). Zoning is more difficult to create and preserve in these minerals as they are less sensitive to magmatic degassing and chemical diffusion through the crystal lattice occurs relatively quickly which removes the zones over time (Costa and Dungan 2005; Costa et al. 2008; Kahl et al. 2011, 2013; Shea et al. 2015a., 2015b.; Petrone et al. 2016; Petrone et al. 2018). Zoning in these crystals can also be generated by undercooling processes (temperatures or pressures lower than those in equilibrium with the crystal) (Milman-Barris et al. 2008; Shea et al. 2015a, 2015b; Ubide et al. 2019 Masotta et al. 2020). This makes distinguishing zone generated by mixing events and undercooling difficult without

elemental maps of crystals.

1.8. The Focus of This Thesis

The purpose of this study is to develop a thorough understanding of the pre-eruptive history of the boninite lavas recovered during IODP Expedition 352. We hypothesize that many boninite lavas from Expedition 352 (1) formed by magma mixing between primitive and evolved boninitic magmas, and (2) reflect multiple mantle sources from which boninite melts are produced.

Chapter 2 of this thesis examines the mineral chemistry of boninite and how it is affected by changing magmatic conditions before an eruption. Data sets presented in this chapter include photomicrographs of crystal textures in boninite lavas, major element chemistry of crystals within boninite lavas, chemical transects of zoned crystals, and single element chemical maps of crystals. These data sets provide a context from which the chemical evolution of the parent magma can be interpreted from the beginning of crystallization until eruption. The results presented in this chapter document multiple episodes of crystallization in the boninite magmas, driven by magma mixing and undercooling processes prior to eruption. Results from this chapter also document crystal contamination from magma injection into a chamber. These interpretations have implications for the magmatic architecture present during early subduction volcanism and how this magmatic architecture affects the chemical evolution of boninite lavas prior to eruption. This chapter is currently in review at *American Mineralogist*.

Chapter 3 of this thesis investigates the barometric, thermal, and chemical evolution of boninite melts from source to eruption based on chemical trends in the fresh

glass within the boninite lavas. Data sets presented in this chapter include major element chemistry of the interstitial glass, major element chemistry of melt inclusions within olivine and orthopyroxene phenocrysts, thermometry and barometry calculations on mineral and glass chemistries, and forward and reverse crystal fractionation models. The data sets indicate that boninite crystallization occurs at pressures between 1-3 kb and temperatures between 1000-1200 °C. Models show that chemical compositions of boninite lavas evolve from LSB/HSB to andesite and dacite compositions as the crystal fractionation progresses. These results imply that a composite magma chamber similar to those observed at mid-ocean ridges exists at depths of 3-10 km during boninite volcanism. Future major and trace element, isotopic, and Laser Raman analysis on interstitial glass and melt inclusions will inform whether source migration of source evolution (i.e., chemical evolution) control the transition from LSB to HSB volcanism. These analyses and interpretations will be completed before a revised version of this chapter is submitted for publication.

Chapter 4 presents the summary, conclusions, and key findings of each chapter. The thesis then concludes with a discussion section that covers additional questions raised by this research and how these questions might be answered in future research.

1.9. References

Arculus, R.J., Pearce, J.A., Murton, B.J., and Van der Laan, S.R. (1992) Igneous stratigraphy and major element geochemistry of Holes 786A and 786B. In Proceedings of the Ocean Drilling Program, Scientific Results Vol. 125, pp. 143–169. Ocean Drilling Program, College Station, TX.

Barnes, S.J., Mole, D.R., Le Vaillant, M., Campbell, M.J., Verrall, M.R., Roberts, M.P., and Evans, N.J. (2016) Poikilitic Textures, Heteradcumulates and Zoned Orthopyroxenes in the Ntaka Ultramafic Complex, Tanzania: Implications for Crystallization Mechanisms of Oikocrysts. Journal of Petrology, 57, 1171–1198.

Bédard, J.H., Lauzière, K., Tremblay, A., and Sangster, A. (1998) Evidence for forearc seafloor-spreading from the Betts Cove ophiolite, Newfoundland: oceanic crust of boninitic affinity. Tectonophysics, 284, 233–245.

Bénard, A., Nebel, O., Ionov, D.A., Arculus, R.J., Shimizu, N., and Métrich, N. (2016) Primary silica-rich picrite and high-Ca boninite melt inclusions in pyroxenite veins from the Kamchatka sub-arc mantle. Journal of Petrology, 57, 1955–1982.

Bloomer, S.H. (1979) Mariana arc-trench studies: Petrology of boninites and evidence for a" boninite series". EOS (Amer. Geophys. Union Trans.), 60, 968.

Bloomer, S.H., and Hawkins, J.W. (1987) Petrology and geochemistry of boninite series volcanic rocks from the Mariana trench. Contributions to Mineralogy and Petrology, 97, 361–377.

Cameron, W.E. (1985) Petrology and origin of primitive lavas from the Troodos ophiolite, Cyprus. Contributions to Mineralogy and Petrology, 89, 239–255.

Cameron, W.E., McCulloch, M.T., and Walker, D.A. (1983) Boninite petrogenesis: Chemical and Nd-Sr isotopic constraints. Earth and Planetary Science Letters, 65, 75–89.

Costa, F., and Chakraborty, S. (2004) Decadal time gaps between mafic intrusion and silicic eruption obtained from chemical zoning patterns in olivine. Earth and Planetary Science Letters, 227, 517–530.

Costa, F., and Dungan, M. (2005) Short time scales of magmatic assimilation from diffusion modeling of multiple elements in olivine. Geology, 33, 837–840.

Costa, F., Dohmen, R., and Chakraborty, S. (2008) Time Scales of Magmatic Processes from Modeling the Zoning Patterns of Crystals. Reviews in Mineralogy and Geochemistry, 69, 545–594.

Crabtree, S.M., and Lange, R.A. (2010) Complex Phenocryst Textures and Zoning Patterns in Andesites and Dacites: Evidence of Degassing-Induced Rapid Crystallization? Journal of Petrology, 52, 3–38.

Crawford, A.J., Falloon, T.J., and Green, D.H. (1989) Classification, petrogenesis and tectonic setting of boninites.

De Campos, C.P., Perugini, D., Ertel-Ingrisch, W., Dingwell, D.B., and Poli, G. (2011) Enhancement of magma mixing efficiency by chaotic dynamics: an experimental study. Contributions to Mineralogy and Petrology, 161, 863–881.

Dietrich, V., Emmermann, R., Oberhänsli, R., and Puchelt, H. (1978) Geochemistry of basaltic and gabbroic rocks from the West Mariana basin and the Mariana trench. Earth and Planetary Science Letters, 39, 127–144.

Dobson, P.F., Blank, J.G., Maruyama, S., and Liou, J.G. (2006) Petrology and geochemistry of boninite-series volcanic rocks, Chichi-Jima, Bonin Islands, Japan. International Geology Review, 48, 669–701.

Druitt, T.H., Costa, F., Deloule, E., Dungan, M., and Scaillet, B. (2012) Decadal to monthly timescales of magma transfer and reservoir growth at a caldera volcano. Nature, 482, 77.

Expedition 352 Scientists (2014) International Ocean Discovery Program Expedition 352 Preliminary Report: Testing subduction initiation and ophiolite models by drilling the outer Izu-Bonin Mariana fore arc. International Ocean Discovery Program, 352.

Falloon, T.J., and Crawford, A.J. (1991) The petrogenesis of high-calcium boninite lavas dredged from the northern Tonga ridge. Earth and Planetary Science Letters, 102, 375–394.

Falloon, T.J., Malahoff, A., Zonenshaina, L.P., and Bogdanova, Y. (1992) Petrology and geochemistry of back-arc basin basalts from Lau Basin spreading ridges at 15, 18 and 19 S. Mineralogy and Petrology, 47, 1–35.

Ghiorso, M.S. (1987) Chemical mass transfer in magmatic processes. 3. Crystal growths, chemical diffusion and thermal diffusion in multicomponent silicate melts. Contributions to Mineralogy and Petrology, 96, 291–313.

Grove, T.L., and Bence, A.E. (1977) Experimental study of pyroxene-liquid interaction in quartz-normative basalt 15597. In Lunar and Planetary Science Conference Proceedings Vol. 8, pp. 1549–1579.

Hickey, R.L., and Frey, F.A. (1982) Geochemical characteristics of boninite series volcanics: implications for their source. Geochimica et Cosmochimica Acta, 46, 2099–2115.

Humphreys, M.C.S., Christopher, T., and Hards, V. (2009) Microlite transfer by disaggregation of mafic inclusions following magma mixing at Soufrière Hills volcano, Montserrat. Contributions to Mineralogy and Petrology, 157, 609–624.

Ishikawa, T., Umino, S., and Kazuya, N. (2002) Boninitic volcanism in the Oman ophiolite: Implications for thermal condition during transition from spreading ridge to arc. Geology, 30, 899–902.

Ishikawa, T., Fujisawa, S., Nagaishi, K., and Masuda, T. (2005) Trace element characteristics of the fluid liberated from amphibolite-facies slab: Inference from the metamorphic sole beneath the Oman ophiolite and implication for boninite genesis. Earth and Planetary Science Letters, 240, 355–377.

Ishizuka, O., Taylor, R.N., Yuasa, M., and Ohara, Y. (2011) Making and breaking an island arc: A new perspective from the Oligocene Kyushu-Palau arc, Philippine Sea. Geochemistry, Geophysics, Geosystems, 12.

Johanssen, A. (1937) A descriptive petrography of the igneous rocks: The intermediate rocks. University of Chicago Press, 3.

Kahl, M., Chakraborty, S., Costa, F., and Pompilio, M. (2011) Dynamic plumbing system beneath volcanoes revealed by kinetic modeling, and the connection to monitoring data: An example from Mt. Etna. Earth and Planetary Science Letters, 308, 11–22.

Kahl, M., Chakraborty, S., Costa, F., Pompilio, M., Liuzzo, M., and Viccaro, M. (2013) Compositionally zoned crystals and real-time degassing data reveal changes in magma transfer dynamics during the 2006 summit eruptive episodes of Mt. Etna. Bulletin of Volcanology, 75, 692.

Kelemen, P.B., Johnson, K.T.M., Kinzler, R.J., and Irving, A.J. (1990) High-field-strength element depletions in arc basalts due to mantle–magma interaction. Nature, 345, 521–524.

Klemme, S., Blundy, J.D., and Wood, B.J. (2002) Experimental constraints on major and trace element partitioning during partial melting of eclogite. Geochimica et Cosmochimica Acta, 66, 3109–3123.

Kuroda, N., and Shiraki, K. (1975) Boninite and related rocks of Chichi-jima, Bonin Islands, Japan. Rep. Fac. Sci. Shizuoka Univ., 10, 145–155.

Kyser, T.K., Cameron, W.E., and Nisbet, E.G. (1986) Boninite petrogenesis and alteration history: constraints from stable isotope compositions of boninites from

Cape Vogel, New Caledonia and Cyprus. Contributions to Mineralogy and Petrology, 93, 222–226.

L'Heureux, I., and Fowler, A.D. (1996) Isothermal constitutive undercooling as a model for oscillatory zoning in plagioclase. The Canadian Mineralogist, 34, 1137–1147.

Li, H.-Y., Taylor, R.N., Prytulak, J., Kirchenbaur, M., Shervais, J.W., Ryan, J.G., Godard, M., Reagan, M.K., and Pearce, J.A. (2019) Radiogenic isotopes document the start of subduction in the Western Pacific. Earth and Planetary Science Letters, 518, 197–210.

Li, Y.-B., Kimura, J.-I., Machida, S., Ishii, T., Ishiwatari, A., Maruyama, S., Qiu, H.-N., Ishikawa, T., Kato, Y., Haraguchi, S., and others (2013) High-Mg Adakite and Low-Ca Boninite from a Bonin Fore-arc Seamount: Implications for the Reaction between Slab Melts and Depleted Mantle. Journal of Petrology, 54, 1149–1175.

Mao, Y.-J., Barnes, S.J., Qin, K.-Z., Tang, D., Martin, L., Su, B., and Evans, N.J. (2019) Rapid orthopyroxene growth induced by silica assimilation: constraints from sector-zoned orthopyroxene, olivine oxygen isotopes and trace element variations in the Huangshanxi Ni–Cu deposit, Northwest China. Contributions to Mineralogy and Petrology, 174, 33.

Masotta, M., Pontesilli, A., Mollo, S., Armienti, P., Ubide, T., Nazzari, M., and Scarlato, P. (2020) The role of undercooling during clinopyroxene growth in trachybasaltic magmas: Insights on magma decompression and cooling at Mt. Etna volcano. Geochimica et Cosmochimica Acta, 268, 258–276.

Meffre, S., Falloon, T.J., Crawford, T.J., Hoernle, K., Hauff, F., Duncan, R.A., Bloomer, S.H., and Wright, D.J. (2012) Basalts erupted along the Tongan fore arc during subduction initiation: Evidence from geochronology of dredged rocks from the Tonga fore arc and trench. Geochemistry, Geophysics, Geosystems, 13.

Meijer, A. (1980) Primitive Arc Volcanism and a Boninite Series: Examples from Western Pacific Island Arcs. In The Tectonic and Geologic Evolution of Southeast Asian Seas and Islands pp. 269–282. American Geophysical Union (AGU).

Meijer, A., Anthony, E., and Reagan, M. (1982) Petrology of volcanic-rocks from the fore-arc sites. Initial Reports of the Deep Sea Drilling Project, 60, 709–729.

Milman-Barris, M.S., Beckett, J.R., Baker, M.B., Hofmann, A.E., Morgan, Z., Crowley, M.R., Vielzeuf, D., and Stolper, E. (2008) Zoning of phosphorus in igneous olivine. Contributions to Mineralogy and Petrology, 155, 739–765.

Murton, B.J., Peate, D.W., Arculus, R.J., Pearce, J.A., and Van der Laan, S. (1992) Trace-element geochemistry of volcanic rocks from site 786: The Izu-Bonin

Forearc. Proceedings of the Ocean Drilling Program Scientific Results, 125, 211–235.

Ohnenstetter, D., and Brown, W.L. (1992) Overgrowth Textures, Disequilibrium Zoning, and Cooling History of a Glassy Four-Pyroxene Boninite Dyke from New Caledonia. Journal of Petrology, 33, 231–271.

Pagé, P., Bédard, J.H., Schroetter, J.-M., and Tremblay, A. (2008) Mantle petrology and mineralogy of the Thetford Mines Ophiolite Complex. Links Between Ophiolites and LIPs in Earth History, 100, 255–292.

Pagé, P., Bédard, J.H., and Tremblay, A. (2009) Geochemical variations in a depleted fore-arc mantle: The Ordovician Thetford Mines Ophiolite. Mantle Dynamics and Crust-Mantle Interactions in Collisional Orogens, 113, 21–47.

Pearce, J.A., and Reagan, M.K. (2019) Identification, classification, and interpretation of boninites from Anthropocene to Eoarchean using Si-Mg-Ti systematics. Geosphere, 15, 1008–1037.

Pearce, J.A., van der Laan, S.R., Arculus, R.J., Murton, B.J., Ishii, T., Peate, D.W., and Parkinson, I.J. (1992) Boninite and harzburgite from Leg 125 (Bonin-Mariana forearc): A case study of magma genesis during the initial stages of subduction. In Proceedings of the ocean drilling program, scientific results Vol. 125, pp. 623–659. Citeseer.

Pearce, J.A., Kempton, P.D., Nowell, G.M., and Noble, S.R. (1999) Hf-Nd element and isotope perspective on the nature and provenance of mantle and subduction components in Western Pacific arc-basin systems. Journal of Petrology, 40, 1579–1611.

Petrone, C.M., Bugatti, G., Braschi, E., and Tommasini, S. (2016) Pre-eruptive magmatic processes re-timed using a non-isothermal approach to magma chamber dynamics. Nature Communications, 7, 12946.

Petrone, C.M., Braschi, E., Francalanci, L., Casalini, M., and Tommasini, S. (2018) Rapid mixing and short storage timescale in the magma dynamics of a steady-state volcano. Earth and Planetary Science Letters, 492, 206–221.

Reagan, M.K., Ishizuka, O., Stern, R.J., Kelley, K.A., Ohara, Y., Blichert-Toft, J., Bloomer, S.H., Cash, J., Fryer, P., Hanan, B.B., and others (2010) Fore-arc basalts and subduction initiation in the Izu-Bonin-Mariana system. Geochemistry, Geophysics, Geosystems, 11.

Reagan, M.K., Pearce, J.A., Petronotis, K., and Expedition 352 Scientists (2015) Expedition 352 summary. Proceedings of the International Ocean Discovery Program, 352, 1–32.

Reagan, M.K., Pearce, J.A., Petronotis, K., Almeev, R.R., Avery, A.J., Carvallo, C., Chapman, T., Christeson, G.L., Ferré, E.C., Godard, M., and others (2017) Subduction initiation and ophiolite crust: new insights from IODP drilling. International Geology Review, 59, 1439–1450.

Reagan, M.K., Heaton, D.E., Schmitz, M.D., Pearce, J.A., Shervais, J.W., and Koppers, A.A.P. (2019) Forearc ages reveal extensive short-lived and rapid seafloor spreading following subduction initiation. Earth and Planetary Science Letters, 506, 520–529.

Resing, J.A., Rubin, K.H., Embley, R.W., Lupton, J.E., Baker, E.T., Dziak, R.P., Baumberger, T., Lilley, M.D., Huber, J.A., Shank, T.M., and others (2011) Active submarine eruption of boninite in the northeastern Lau Basin. Nature Geoscience, 4, 799.

Rossi, S., Petrelli, M., Morgavi, D., Vetere, F.P., Almeev, R.R., Astbury, R.L., and Perugini, D. (2019) Role of magma mixing in the pre-eruptive dynamics of the Aeolian Islands volcanoes (Southern Tyrrhenian Sea, Italy). Lithos, 324–325, 165–179.

Ryan, J.G. (2013) Embedding research practice activities into earth and planetary science courses through the use of remotely operable analytical instrumentation: Interventions and impacts on student perceptions and activities. Geoscience Research and Education: Teaching at Universities. New York: Springer Verlag, 149–162.

Ryan, J.G., Shervais, J.W., Li, Y., Reagan, M.K., Li, H.Y., Heaton, D., Godard, M., Kirchenbaur, M., Whattam, S.A., and Pearce, J.A. (2017) Application of a handheld X-ray fluorescence spectrometer for real-time, high-density quantitative analysis of drilled igneous rocks and sediments during IODP Expedition 352. Chemical Geology, 451, 55–66.

Saunders, K., Rinnen, S., Blundy, J., Dohmen, R., Klemme, S., and Arlinghaus, H.F. (2012) TOF-SIMS and electron microprobe investigations of zoned magmatic orthopyroxenes: First results of trace and minor element analysis with implications for diffusion modeling. American Mineralogist, 97, 532–542.

Shea, T., and Hammer, J.E. (2013) Kinetics of cooling- and decompression-induced crystallization in hydrous mafic-intermediate magmas. Journal of Volcanology and Geothermal Research, 260, 127–145.

Shea, T., Costa, F., Krimer, D., and Hammer, J.E. (2015a) Accuracy of timescales retrieved from diffusion modeling in olivine: A 3D perspective†. American Mineralogist, 100, 2026–2042.

Shea, T., Lynn, K.J., and Garcia, M.O. (2015b) Cracking the olivine zoning code: Distinguishing between crystal growth and diffusion. Geology, 43, 935–938.

Shea, T., Hammer, J.E., Hellebrand, E., Mourey, A.J., Costa, F., First, E.C., Lynn, K.J., and Melnik, O. (2019) Phosphorus and aluminum zoning in olivine: contrasting behavior of two nominally incompatible trace elements. Contributions to Mineralogy and Petrology, 174, 85.

Shervais, J.W., Reagan, M., Haugen, E., Almeev, R.R., Pearce, J.A., Prytulak, J., Ryan, J.G., Whattam, S.A., Godard, M., Chapman, T., and others (2019) Magmatic Response to Subduction Initiation: Part 1. Fore-arc Basalts of the Izu-Bonin Arc From IODP Expedition 352. Geochemistry, Geophysics, Geosystems, 20, 314–338.

Singer, B.S., Costa, F., Herrin, J.S., Hildreth, W., and Fierstein, J. (2016) The timing of compositionally-zoned magma reservoirs and mafic 'priming' weeks before the 1912 Novarupta-Katmai rhyolite eruption. Earth and Planetary Science Letters, 451, 125–137.

Sisson, T.W., and Bronto, S. (1998) Evidence for pressure-release melting beneath magmatic arcs from basalt at Galunggung, Indonesia. Nature, 391, 883–886.

Sparks, S.R.J., Sigurdsson, H., and Wilson, L. (1977) Magma mixing: a mechanism for triggering acid explosive eruptions. Nature, 267, 315–318.

Stern, R.J., and Bloomer, S.H. (1992) Subduction zone infancy: Examples from the Eocene Izu-Bonin-Mariana and Jurassic California arcs. GSA Bulletin, 104, 1621–1636.

Streck, M.J. (2008) Mineral Textures and Zoning as Evidence for Open System Processes. Reviews in Mineralogy and Geochemistry, 69, 595–622.

Taylor, R.N., Nesbitt, R.W., Vidal, P., Harmon, R.S., Auvray, B., and Croudace, I.W. (1994) Mineralogy, Chemistry, and Genesis of the Boninite Series Volcanics, Chichijima, Bonin Islands, Japan. Journal of Petrology, 35, 577–617.

Ubide, T., and Kamber, B.S. (2018) Volcanic crystals as time capsules of eruption history. Nature Communications, 9, 326.

Ubide, T., Mollo, S., Zhao, J., Nazzari, M., and Scarlato, P. (2019) Sector-zoned clinopyroxene as a recorder of magma history, eruption triggers, and ascent rates. Geochimica et Cosmochimica Acta, 251, 265–283.

Umino, S. (1986) Magma mixing in boninite sequence of Chichijima, Bonin Islands. Journal of Volcanology and Geothermal Research, 29, 125–157.

Van Malderen, S. (2017) Optimization of methods based on laser ablation-ICP-mass spectrometry (LA-ICP-MS) for 2-D and 3-D elemental mapping. PhD Thesis, Ghent University.

Van Malderen, S.J., Van Acker, T., and Vanhaecke, F. (2020) Sub-micrometer Nanosecond LA-ICP-MS Imaging at Pixel Acquisition Rates above 250 Hz via a Low-Dispersion Setup. Analytical Chemistry, 92, 5756–5764.

Waters, L.E., and Lange, R.A. (2017) An experimental study of (Fe-Mg) KD between orthopyroxene and rhyolite: a strong dependence on H2O in the melt. Contributions to Mineralogy and Petrology, 172, 42.

Whattam, S.A., Shervais, J.W., Reagan, M.K., Coulthard JR, D.A., Pearce, J.A., Jones, P., Seo, J., Putirka, K., Chapman, T., Heaton, D., and others (2020) Mineral compositions and thermobarometry of basalts and boninites recovered during IODP Expedition 352 to the Bonin forearc. American Mineralogist.

Wyman, D.A. (1999) Paleoproterozoic boninites in an ophiolite-like setting, Trans-Hudson orogen, Canada. Geology, 27, 455–458.

CHAPTER II

2. PETROLOGIC EVOLUTION OF BONINITE LAVAS FROM THE IBM FORE-ARC, IODP EXPEDITION 352: EVIDENCE FOR OPEN-SYSTEM PROCESSES DURING EARLY SUBDUCTION ZONE MAGMATISM

ABSTRACT

Boninite samples from several intervals within Hole U1439C, recovered during IODP Expedition 352, show highly variable mineral chemistries that require complex crystallization histories. Early-crystallized olivine have embayed and reacted margins, and some exhibit zoning. A few olivines have multiple zones, with both normal and reverse zoning between Fo86-92. Cr-rich spinel is found as inclusions both in olivine and low-Ca pyroxene. Large, euhedral, low-Ca pyroxene (i.e., enstatite/clinoenstatite) crystals exhibit complex sector and oscillatory zoning patterns. Smaller pyroxene grains show oscillatory zoning with cores and zones ranging from pigeonite to augite. Late crystallizing augite has highly variable Al_2O_3 contents (1.9-13.7 wt%.) and a Ca-Tschermak component (3-13 mol%), which reflects disequilibrium conditions. Oscillatory, normal, and reverse zoning in olivine and pyroxene appears to have formed in response to multi-stage magma mingling or mixing processes, which introduced additional Ca, Fe, Ti, and Al into parental boninitic melts. Sector zoning in low-Ca pyroxenes is the result of crystallization during periods of moderate undercooling between mixing events. Disequilibrium crystallization of pyroxene rims reflects rapid cooling during an eruption.

Keywords: Boninite, Magma Mixing, Olivine, Pyroxene, Zoning

Coauthors: Jeffrey G. Ryan, John W. Shervais, Ciprian Stremtan, Martin Rittner, Antonio Luna, Stephen A. Hill, Zachary D. Atlas, Bradford C. Mack

2.1. Introduction

Boninites are unusual, high SiO_2 (>52 wt%), high MgO (>8 wt%), and low TiO_2 (<0.5 wt%) mafic rocks associated with subduction processes (Pearce and Reagan 2019). They are commonly found in western Pacific arc systems such as the Izu-Bonin-Mariana (IBM) system and Tonga-Kermadec arc system (Dietrich et al. 1978; Bloomer et al. 1979; Meijer 1980; Meijer et al. 1982; Crawford 1989; Arculus et al. 1992; Dobson et al. 2006; Meffre et al. 2012) and have been observed actively erupting in the Lau Basin (Falloon and Crawford 1991; Falloon et al. 1992; Resing et al. 2011). Boninites are also found in ophiolites such as Troodos (Cyprus), Samail (Oman), Thetford Mines (Canada), Betts Cove (Canada), and Koh (New Caledonia) (Cameron 1985; Kyser et al. 1986; Meffre et al. 1996; Bedard et al. 1998; Wyman 1999; Ishikawa et al. 2002, 2005; Page et al. 2008, 2009). “Boninite-like” veins have also been found in some mantle xenoliths from Kamchatka and the West Bismarck arc (Benard et al. 2016, 2018).

Boninites associated with the Izu-Bonin fore-arc are thought to reflect magmatic processes associated with subduction initiation, in which the foundering of the old oceanic lithosphere along a fracture zone or transform boundary results in the upwelling of asthenospheric mantle (e.g., Stern and Bloomer 1992; Reagan et al. 2017). There are competing theories as to how boninite magmas form in this environment. Pearce et al. (1999) present the hypothesis that boninites form as the result of melt mixing between partial melts from gabbroic veins in the shallow mantle and melts from the upwelling asthenosphere. An alternative theory is that the mantle upwelling results in decompression melting and produces voluminous tholeiitic basalts (fore-arc basalts

(FAB); Reagan et al. 2010, 2017, 2019; Shervais et al. 2019), extensively depleting the mantle beneath the infant subduction zone. This depleted harzburgite mantle is fluxed with fluid from the downgoing slab, which causes melting and the formation of boninite magma (Li et al. 2019; Reagan et al. 2017, 2019).

Past studies of western Pacific boninites have focused on their unusual whole-rock major and trace element chemistry (Hickey and Frey 1982; Bloomer and Hawkins 1987; Falloon and Crawford 1991; Arculus et al. 1992; Murton et al. 1992; Pearce et al. 1992, 1999; Dobson et al. 2006). Detailed petrologic studies of complete boninite volcanic sections are comparatively rare due to limited land-based exposures, and unreliable recovery during dredging and submersible dives),. IODP Expedition 352 cored over 800 m of the basement at two different sites, with over 460 m of boninite and high-Mg andesite core recovered (Reagan et al. 2015, 2017). We have studied a suite of Expedition 352 boninites from Hole U1439C, using thin-section petrography and mineral chemistry, to place constraints on the petrologic development of these lavas. Our results point to a significant role for open-system magmatic processes, both among different boninitic lava types, and with spatially associated basalts or boninitic differentiates.

2.2. Past mineralogical and petrologic studies of Izu-Bonin boninites

Johannsen (1937) reported on high-Mg/high-Si volcanic rocks in the Bonin (Ogasawara) Islands; however, systematic petrologic and geochemical studies of these lavas did not occur until much later (e.g., Kuroda and Shiraki 1975; Hickey and Frey 1982; Cameron et al. 1983). Meijer (1980, 1982) proposed the existence of a boninite suite associated with fore-arc volcanism based on discoveries by the Deep Sea Drilling

Program (DSDP) and dredging. The first full petrologic study was performed by Umino (1986), who distinguished two major types and five subtypes of boninite, and, based in part on zoned pyroxene crystals, argued for a dynamic magma chamber with the mixing of more- and less-evolved boninitic magmas to produce at least one of the lava subtypes. Taylor et al. (1994) examined trace element compositions in Chichijima boninite, noting their unusually low Ti/Zr and Sm/Zr ratios, which were inferred to reflect chemical inputs from an amphibolitic, probably slab-related, source. Dobson et al. (2006) conducted an extensive study of the Chichijima volcanics, documenting related rock types ranging from Mg-rich boninite to rhyolite, and the presence of high-Ca clinopyroxene in all the Chichijima volcanic rock types. Li et al. (2013) described boninite and differentiates from Hahajima seamount occurring in association with adakites, which point to high-temperature conditions on the slab. ODP Leg 125 (Hole 786A) drilled a boninitic volcanic sequence in a basement high near the Izu-Bonin trench at Site 786, NE of Sumisu-Jima island, that appeared to be lithologically and compositionally similar to both ChichiJima Island boninites, and to Mariana boninites encountered during DSDP Site 458 (Meijer et al. 1982; Arculus et al. 1992).

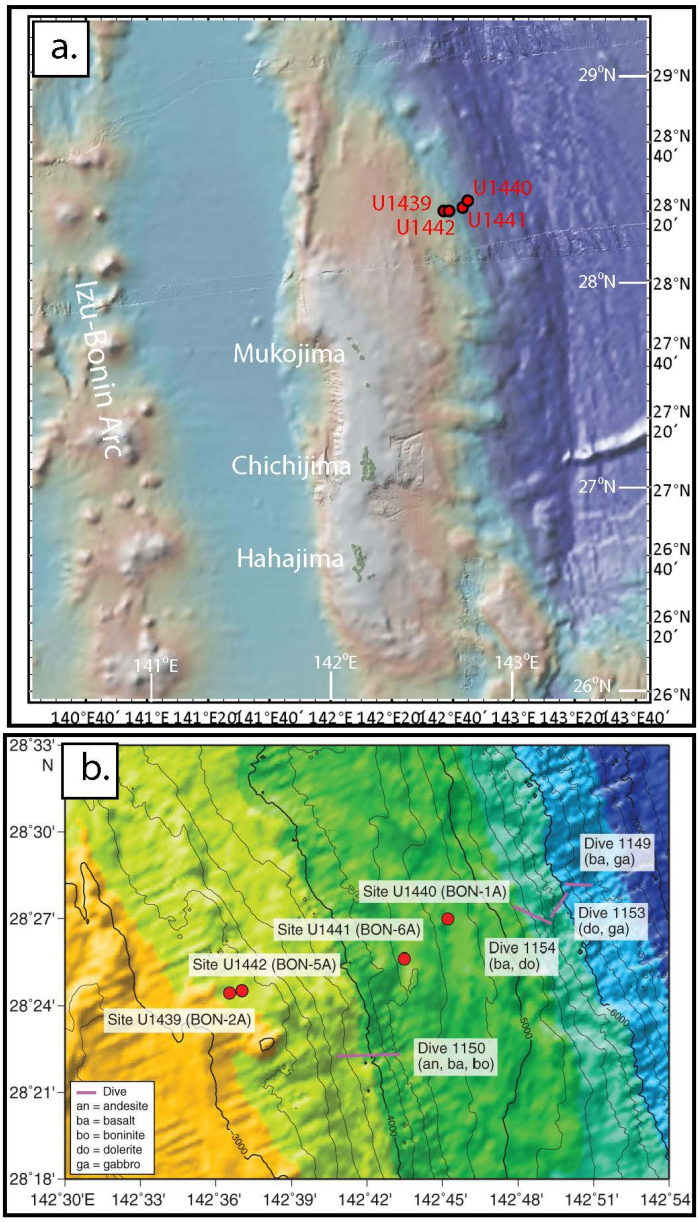

Figure 2.1
Location maps (a., b.) based on Reagan et al. (2015) and Shervais et al. (2019). (a.) Location of drill-sites U1439, U1440, U1441, U1442 in relation to the Bonin Islands on the Ogasawara Plateau. (b.) Drill sites for IODP Expedition 352 from (Reagan et al. 2015) and dive sites of Shinkai 6500 (Ishizuka et al. 2011).

2.3. IODP Expedition 352

A primary objective of IODP Expedition 352 was to recover a complete stratigraphic section through the igneous crust exposed near the trench in the Izu-Bonin fore-arc, as identified during a series of Shinkai dive expeditions (e.g., Ishizuka et al. 2011). Four sites were drilled, two into boninites (Sites U1439 and U1442), and two into fore-arc basalts (FAB) (Sites U1440 and U1441), with 20-30% recovery in the boninites, and ≤10% in the basalts (Reagan et al. 2015; Figures 2.1 and 2.2). In one fore-arc basalt site (U1440) and one boninite site (U1439), rocks with diabasic textures were penetrated, indicating that the transition from tholeiite to boninite likely reflects a shift in the locus of magmatism, at odds with the ostensibly vertical basalt-to-boninite sequences encountered in the Troodos ophiolite (Reagan et al. 2017).

Sites U1439 and U1442, though less than 1 km apart, reflect remarkably different stratigraphies (Figure 2.1). Hole U1442A is dominated by distinctive low-Si boninite (LSB), and boninitic differentiates (terminology after Pearce and Reagan 2019), occurring as lava flows and hyaloclastites, capped with a sequence of late-stage high-Si boninite (HSB) hyaloclastites and lava flows, which are mineralogically and chemically similar to those found on Chichijima and other IBM sites. In contrast, Site U1439 (Holes U1439A and U1439C) reflects greater lithologic diversity, with diabasic rocks that appear to represent boninite feeder dikes overlain by LSB and differentiates, which are themselves separated from overlying HSB by a layer of what was described as “basaltic” boninite (Reagan et al. 2015, Figure 2.2). Also evident in the U1439C cores are what were described as “magma mingling” textures, interpreted as intercalated evolved and

primitive boninitic melts (Reagan et al. 2015), pointing to complexities in the generation and evolution of the Expedition 352 boninitic magmas.

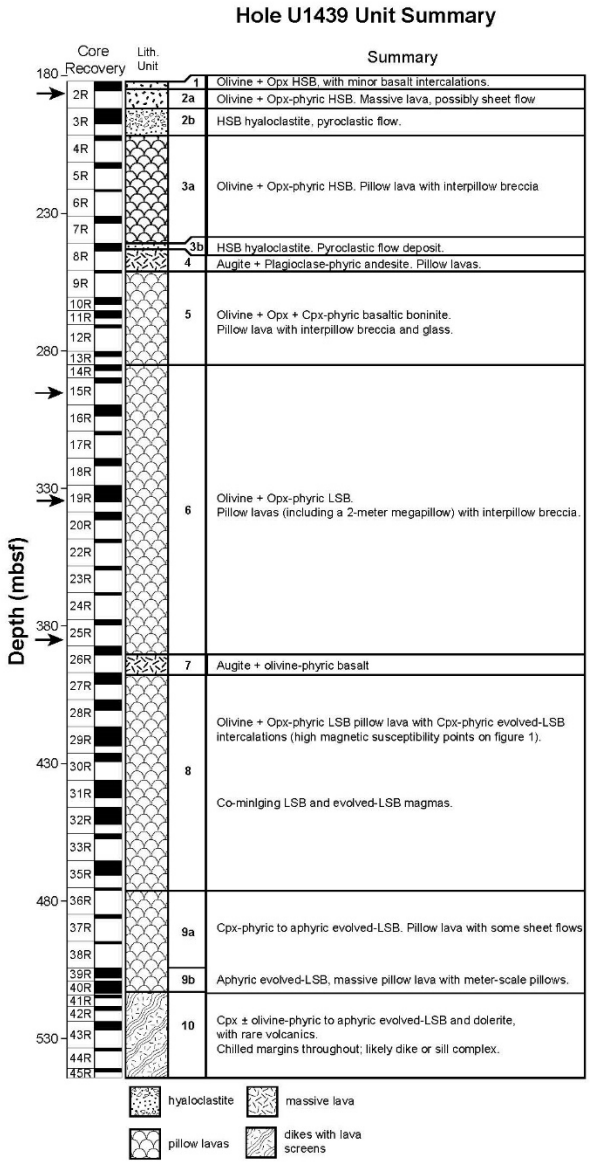

Figure 2.2
Core summary from hole U1439C based on Reagan et al. (2015). Arrows to the left of the figure, point to the core section which samples U1439C-2R3W 2-3, U1439C-15R1W 8-10, U1439C-19R2W 46-48, and U1439C-25R2W 18-19 came from.

2.4. Samples and Methods

The IODP Expedition 352 boninite sequences were initially targeted for examination as part of a multi-year, course-based undergraduate research experience (CURE) for University of South Florida Geology undergraduates, overseen by co-author Ryan as part of an ongoing educational investigation into the use of research microbeam instrumentation in geoscience courses (see Ryan 2013). Boninite samples were selected to provide representative coverage of the different lithologies at each site and were also chosen to be comparatively crystal-rich, to facilitate petrographic and microprobe examination of the different crystallizing phases encountered in the samples. Thirty samples from Holes U1442A, U1439A, and U1439C were obtained from the IODP Core Repository at Kochi, Japan specifically for classroom study, and an additional fifteen samples came from the samples requested by co-author Ryan for post-cruise geochemical study. Polished thin-sections were prepared from each of the samples for polarized-light petrographic analysis. Initial petrographic analyses of the samples were conducted during the course by participating students, who also helped to identify petrographically interesting samples for subsequent mineral chemistry studies.

Micro-imaging and mineral chemistry measurements were conducted using the JEOL 8900R Superprobe EPMA system of the Florida Center for Analytical Electron Microscopy (FCAEM) at Florida International University and the Cameca SXfive of the Center for Material Characterization at Boise State University. Samples were explored in electron backscatter mode, with quick energy dispersive spectrometer (EDS) measurements to identify major mineral phases. For quantitative WDS mineral analyses,

operating conditions were a 15kV accelerating voltage and a 20 nA beam current, with a spot size of 1-2 μm on the JEOL 8900R Superprobe and 5-10 μm on the Cameca SXfive. The elements Si, Al, Fe, Mg, Ca, Mn, Na, K, Ti, and Cr, were routinely measured on all samples on both instruments. For the JEOL 8900R Superprobe, a selection of mineral standards from SPI, Inc., and Micro-Analysis Consultants, Ltd. were used to calibrate WDS measurements of unknowns (fayalite, olivine, Cr-diopside, An65 plagioclase, kaersutite, augite, enstatite, and chromite: see Table A.1. for compositions). Typically, a mixed suite of standards (sometimes including the USGS BHVO-1 basaltic glass standard) were used to conduct initial characterizations, followed by re-calculation or re-analysis using a smaller set of compositionally matched standards after minerals were identified. For the Cameca SXfive a selection of synthetic mineral standards, as well as, natural mineral and glass standards from the Smithsonian Institute and SPI, Inc. were used to calibrate WDS measurements of unknowns (San Carlos Olivine, Chromite, Anorthite, Diopside, Syn Tephroite, Syn Fayalite, Syn Rutile, Amelia Albite, and Basaltic Glass VG-2: see Table A.1. for compositions). EPMA measurements were used to confirm microscope-based phase identifications, to identify important minor phases (Cr rich spinels, and rare ilmenites and apatites), and to characterize the mineral zoning and overgrowth textures that were encountered in some of the samples. Given our selection bias toward highly phyric samples, measurements on boninite glasses were often not possible. In those cases where it was, a 50 μm spot size was used to minimize Na volatility, and data were calibrated using a mixture of basaltic and high-silica glasses (USGS BHVO-1; USNM rhyolite glass).

Elemental Maps were created using the Cameca SXfive of the Center for Material Characterization at Boise State University and the TOFWERK ICP-TOF 2R at TOFWERK AG in Switzerland. The instrumental setup used for the laser ablation inductively coupled mass spectrometry imaging (LA ICP-MS) experiments consisted of a laser ablation system (excimer ArF 193 nm wavelength, Analyte G2) equipped with an ultra-fast laser ablation chamber (van Malderen et al., 2020) and interfaced with a time-of-flight mass spectrometer (icpTOF 2R). The coupling of the two instruments was carried out via an Aerosol Rapid Introduction System (ARIS), which allowed the acquisition of full pulse signals of less than 3 ms (FW0.1M). The instrumental operating conditions are listed in the supplemental data (Table A.2.). The resulting images were generated using the HDIP software (van Malderen, 2017).

2.5. Results

2.5.1.Petrography

The Expedition 352 boninite and boninitic differentiates examined for this study are variably phenocryst-rich and show some first-order similarities to the Chichijima suites examined by Umino (1986) and Dobson et al. (2006) (Table 2.1 & 2.2). The common phenocryst assemblage in the boninites examined in this study is low-Ca pyroxene (enstatite and clinoenstatite) + olivine, with later-formed acicular crystals of low-Ca pyroxene (enstatite and clinoenstatite to pigeonite) and high-Ca pyroxene in a glassy or crystalline matrix (Figure A.1). Some enstatite crystals were enclosing small olivine grains, indicating that these enstatites crystallized at the expense of olivine. Some

HSB samples lack olivine, consisting exclusively of low-Ca pyroxene and groundmass clinopyroxene in a glassy or crystalline matrix. In more differentiated samples (high-Mg andesites and dacites), the primary crystallizing phases are augitic clinopyroxene and plagioclase, with rare grains of ilmenite and apatite. Olivine grains are typically rounded and embayed, indicating partial resorption associated with the growth of enstatite and clinoenstatite at lower pressures. Olivine xenocrysts were observed in sample U1439C-25R2W18-19; these xenocrysts are much larger (>6 mm) than the primary olivine phenocrysts (≤1.5 mm) observed in this sample and exhibit resorbed textures. Red to purple chromium-rich spinel is a common accessory mineral in boninite, often found enclosed within larger olivine and (rarely) enstatite and clinoenstatite crystals (but never within pigeonite grains), and as free grains within the sample matrices (Figure A.1). Melt inclusions with vapor bubbles and crystals nucleating from the walls of the inclusion have also been observed in some samples (Figure A.2c.-2f.).

Table 2.1. Normal Magma End-member Assemblages

End member	Phenocrysts	Minor minerals	Matrix	Secondary Minerals
HSB	Orthopyroxene ± Olivine	Cr-spinel	Clinopyroxene	± Zeolite & Calcite
LSB	Olivine + Orthopyroxene	Cr-spinel	Clinopyroxene ± Plagioclase	± Zeolite & Calcite
HMA	Plagioclase + Clinopyroxene	Magnetite + Ilmenite	Clinopyroxene + Plagioclase	± Zeolite & Calcite

[a] End-members: High-Si Boninite (HSB), Low-Si Boninite (LSB), High-Mg Andesite (HMA)

2.5.2.Mineral chemistry

Table 2.2 presents typical major element compositions for the Expedition 352 boninite phenocryst phases. Enstatite and clinoenstatite phenocrysts vary from En80-86, with Wo3-5 (Figure 2.3), broadly similar to those reported on Chichijima by Umino (1986). We do not see enstatite rimming clinoenstatite, as was reported by Dobson et al. (2006), but instead find that most of our low-Ca pyroxene phenocrysts are homogeneous, with optical characteristics suggestive in most cases of enstatite. The more calcic clinopyroxene compositions in our samples are pigeonite (En70±3 Fs12±0.6 Wo16±2) and augite (En42±9 Fs14±4 Wo36±4.5). Augite from the most differentiated high-Mg andesite is typically En50±3 Fs7±0.8 Wo42±2, in association with late-crystallized An81-83 plagioclase.

Olivine phenocryst compositions range from Fo86-92, similar to those reported at Chichijima by Umino (1986) and Dobson et al. (2006). Olivine xenocrysts in sample U1439C-25R2W18-19 exhibit consistent compositions of Fo88 (Table 2.3.), while olivine phenocrysts from the sample have compositions between Fo89-92. Cr-spinel grains contain 8-10 wt% Al_2O_3, 11-13 wt% MgO, 18-24 wt% Feo, and 56-60 wt% Cr_2O_3 (Table 2.2.).

Table 2.2. Normal Mineral Compositions Observed In Lavas

Sample	Mineral	SiO2 (wt%)	TiO2 (wt%)	Al2O3 (wt%)	Cr2O3 (wt%)	FeO (wt%)	MgO (wt%)	MnO (wt%)	NiO (wt%)	CaO (wt%)	Na2O (wt%)	K2O (wt%)	P2O5 (wt%)	Total (wt%)	Wo	En	Fs	Fo	An	Mg#	Cr#
U1439A-21X-1-W 2-3	En	57.18	0.00	0.67	0.42	7.70	32.33	0.07	0.07	1.24	0.04	0.01	0.00	99.73	2.38	86.12	11.50	-	-	88.22	29.34
U1439A-21X-1-W 2-3	En	56.44	0.00	1.19	0.61	8.74	31.68	0.09	0.10	1.54	0.02	0.00	0.00	100.39	2.93	84.06	13.01	-	-	86.60	25.60
U1439A-21X-1-W 2-3	CLEN	55.51	0.00	2.10	0.31	10.56	27.90	0.11	0.08	4.27	0.05	0.00	0.00	100.89	8.32	75.62	16.06	-	-	82.48	8.95
U1439A-21X-1-W 2-3	PIG	52.64	0.36	4.02	0.19	10.87	22.72	0.11	0.08	9.85	0.09	0.02	0.00	100.94	19.72	63.29	16.98	-	-	78.84	3.00
U1439A-21X-1-W 2-3	Cr-Sp	0.31	0.02	8.62	60.14	19.33	10.54	0.16	0.14	0.04	0.00	0.01	0.00	99.31	-	-	-	-	-	49.28	82.39
U1439A-21X-1-W 2-3	Cr-Sp	0.12	0.13	8.40	58.16	23.62	11.13	0.18	0.13	0.06	0.05	0.00	0.00	101.97	-	-	-	-	-	45.64	82.29
U1439C-33R-1-W, 137-140	Cr-Sp	0.13	0.08	9.71	56.72	19.36	13.48	0.30	0.00	0.12	0.09	0.00	0.00	99.99	-	-	-	-	-	55.37	79.67
U1439C-33R-1-W, 137-140	Ol	39.72	0.00	0.07	0.08	8.51	52.41	0.14	0.00	0.15	0.02	0.01	0.00	101.12	-	-	-	91.65	-	91.65	44.28
U1439C-29R-2-W 93-94	AUG	50.59	0.15	2.69	0.96	3.92	18.38	0.14	0.00	23.16	0.17	0.00	0.00	100.14	44.71	49.38	5.90	-	-	89.32	19.31
U1439C-29R-2-W 93-94	AUG	50.13	0.00	2.13	0.60	3.87	20.51	0.13	0.00	23.00	0.20	0.03	0.00	100.59	42.16	52.30	5.54	-	-	90.42	15.82
U1439C-34G-1-W 45-46	Ol	41.42	0.00	0.00	0.12	8.87	50.06	0.05	0.40	0.14	0.00	0.00	0.00	101.05	-	-	-	90.96	-	90.96	100.00
U1439C-34G-1-W 45-46	AUG	49.72	0.44	6.85	0.09	8.40	15.33	0.06	0.02	18.15	0.17	0.03	0.00	99.27	39.42	46.34	14.25	-	-	76.49	0.88
U1439C-34G-1-W 45-46	CLEN	56.03	0.00	1.40	0.76	8.90	29.19	0.10	0.04	3.59	0.04	0.00	0.00	100.04	7.01	79.40	13.59	-	-	85.39	26.84
U1439C-34G-1-W 45-46	CLEN	56.31	0.00	1.29	0.49	8.51	30.45	0.12	0.04	2.81	0.03	0.02	0.00	100.06	5.42	81.76	12.82	-	-	86.44	20.46
U1439C-34G-1-W 45-46	Cr-Sp	0.13	0.15	10.61	57.73	18.12	13.37	0.14	0.13	0.06	0.00	0.00	0.00	100.44	0.17	56.72	43.11	-	-	56.82	78.50
U1442A-56R-2-W 33-50	PLAG	49.81	0.00	31.37	0.00	0.65	0.24	0.03	0.00	15.33	2.38	0.05	0.00	99.87	-	-	-	-	87.53	39.56	-
U1442A-56R-2-W 33-50	PLAG	50.34	0.02	31.20	0.02	0.53	0.26	0.00	0.00	15.70	2.44	0.02	0.06	100.58	-	-	-	-	87.64	46.80	0.04
U1442A-56R-2-W 33-50	PLAG	51.37	0.03	31.20	0.00	0.61	0.24	0.03	0.00	15.36	2.27	0.52	0.04	101.66	-	-	-	-	86.68	41.62	0.00
U1442A-30R-3-W 121-122	PLAG	51.80	0.00	30.93	0.01	0.67	0.28	0.01	0.00	15.76	2.13	0.25	0.08	101.91	-	-	-	-	88.35	42.75	0.02
U1442A-30R-3-W 121-122	PLAG	50.41	0.02	31.38	0.00	0.66	0.31	0.00	0.00	16.22	2.42	0.05	0.00	101.47	-	-	-	-	87.98	45.61	-
U1442A-48R-1-W 97-98	PIG	53.88	0.02	2.82	0.84	7.03	23.30	0.13	0.01	11.47	0.09	0.00	0.00	99.60	23.23	65.66	11.11	-	-	85.53	16.71
U1442A-48R-1-W 97-98	PIG	54.43	0.14	2.08	0.30	9.21	26.15	0.12	0.03	7.07	0.10	0.00	0.03	99.64	13.96	71.84	14.20	-	-	83.50	8.78

[a] Minerals: Olivine (Ol), Cr-Spinel (Cr-SP), Enstatite (En), Clinoenstatite (CLEN), Pigeonite (PIG), Augite (AUG), Plagioclase (PLAG).

[b] Mineral end-member components: Enstatite (En), Wollastonite (Wo), Ferrosilite (Fs),Forsterite (Fo), Anorthite (An)

[c] Mg#=100*(Mg/(Mg+Fe)), Cr#= 100* (Cr/(Cr+Al))

Table 2.3. Unzoned Olivine Compositions

Sample	Mineral	SiO2 (wt%)	TiO2 (wt%)	Al2O3 (wt%)	Cr2O3 (wt%)	FeO (wt%)	MgO (wt%)	MnO (wt%)	CaO (wt%)	Na2O (wt%)	K2O (wt%)	Total (wt%)	Fo	Fa
25R2	Ol Xeno	41.309	0.002	0.008	0.040	10.763	45.731	0.166	0.196	0.000	0.003	98.218	88.337	11.663
25R2	Ol Xeno	41.670	0.002	0.023	0.052	10.767	46.882	0.181	0.198	0.006	0.005	99.786	88.587	11.413
25R2	Ol Xeno	41.593	0.006	0.018	0.042	10.543	46.453	0.160	0.208	0.002	0.004	99.028	88.706	11.294
25R2	Ol Xeno	40.491	0.000	0.010	0.028	10.908	48.319	0.078	0.143	0.008	0.009	99.994	88.759	11.241
25R2	Ol Xeno	40.995	0.045	0.000	0.056	10.629	47.997	0.091	0.165	0.016	0.018	100.012	88.950	11.050
15R1	OL Pheno	40.555	0.000	0.000	0.017	12.994	46.926	0.077	0.170	0.000	0.000	100.739	86.555	13.445
15R1	OL Pheno	41.076	0.000	0.000	0.110	12.375	47.016	0.086	0.155	0.000	0.002	100.820	87.134	12.866
15R1	OL Pheno	41.703	0.001	0.068	0.290	11.586	46.450	0.190	0.159	0.125	0.123	100.695	87.725	12.275
15R1	OL Pheno	41.329	0.001	0.054	0.083	11.767	47.383	0.150	0.137	0.033	0.015	100.951	87.772	12.228
15R1	OL Pheno	40.664	0.002	0.019	0.064	11.810	47.674	0.157	0.140	0.004	0.000	100.534	87.798	12.202
15R1	OL Pheno	43.442	0.010	1.251	0.055	12.001	43.099	0.170	0.239	0.293	0.284	100.843	86.489	13.511
19R2	OL Pheno	41.978	0.000	0.012	0.061	10.441	48.192	0.217	0.157	0.000	0.000	101.058	89.163	10.837
19R2	OL Pheno	42.364	0.025	0.039	0.054	10.040	48.445	0.167	0.190	0.000	0.000	101.324	89.585	10.415
2R3	OL Pheno	42.247	0.000	0.021	0.115	10.944	48.009	0.196	0.115	0.018	0.011	101.676	88.662	11.338
2R3	OL Pheno	42.166	0.000	0.032	0.076	11.654	47.073	0.209	0.147	0.000	0.016	101.373	87.805	12.195

[a] Mineral: Olivine Xenocryst (Ol Xeno), Olivine Phenocryst (Ol Pheno).

[b] Samples: U1439C-25R-2-W 18-19 (25R2), U1439C-15R-1-W 8-10 (15R1), U1439C-19R-2-W 46-48 (19R2), U1439C-2R-3-W 2-3 (2R3).

[c] Olivine End-member Components: Forsterite (Fo), Fayalite (Fa).

2.5.3.Mineral zoning and overgrowths

A subset of the samples examined in the study (four of 45: samples U1439C-2R3W 2-3, U1439C-15R1W 8-10, U1439C-19R2W 46-48, and U1439C-25R2W 18-19) showed unusual mineral zoning/overgrowth textures (these will be referred to as 2R3, 15R1, 19R2, and 25R2 for brevity). These samples were all from the volcanic units in Hole U1439C and encompass both the HSB and LSB boninite subtypes (Reagan et al. 2015; 2017). These four samples contain olivine, enstatite, and clinoenstatite as phenocrysts in a groundmass dominated by acicular clinopyroxene (pigeonite to augite) in glass (Figure A.2.).

Most of the larger pyroxene phenocrysts show overgrowths, evident both optically and in electron backscatter imaging, with low-Ca pyroxene cores, and calcic overgrowths (Table A.3.; Figure A.2.). Some of the larger orthopyroxene grains and even a few of the large olivines appear to be serving as nucleation sites for clinopyroxene growth. Large low-Ca pyroxene grains in samples 2R3 and 15R1 exhibit oscillatory zoning optically and in backscatter electron images (BSE).

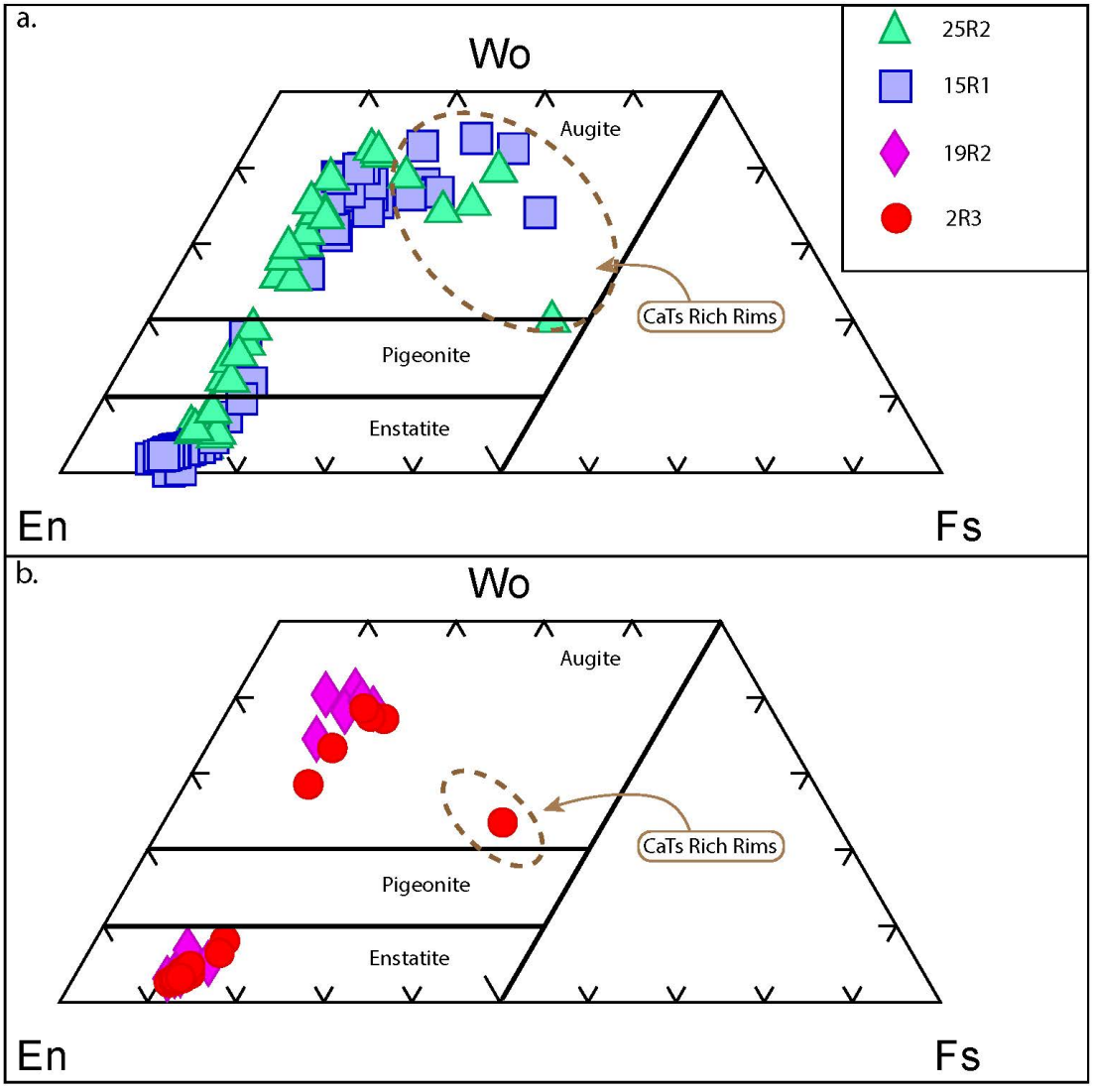

Figure 2.3
Pyroxene Quadrilateral with pyroxenes from samples samples U1439C-2R3W 2-3 (2R3), U1439C-15R1W 8-10 (15R1), U1439C-19R2W 46-48 (19R2), and U1439C-25R2W 18-19 (25R2) plotted. Enstatite (En), Wollastonite (Wo), Ferrosilite (Fs), and Ca-Tschermak (CaTs). Pyroxenes that have anomalous Al concentration show a trend towards ferrosilite and can be seen in the brown dashed circle. Data can be found in Tables (A.3. & A.4.).

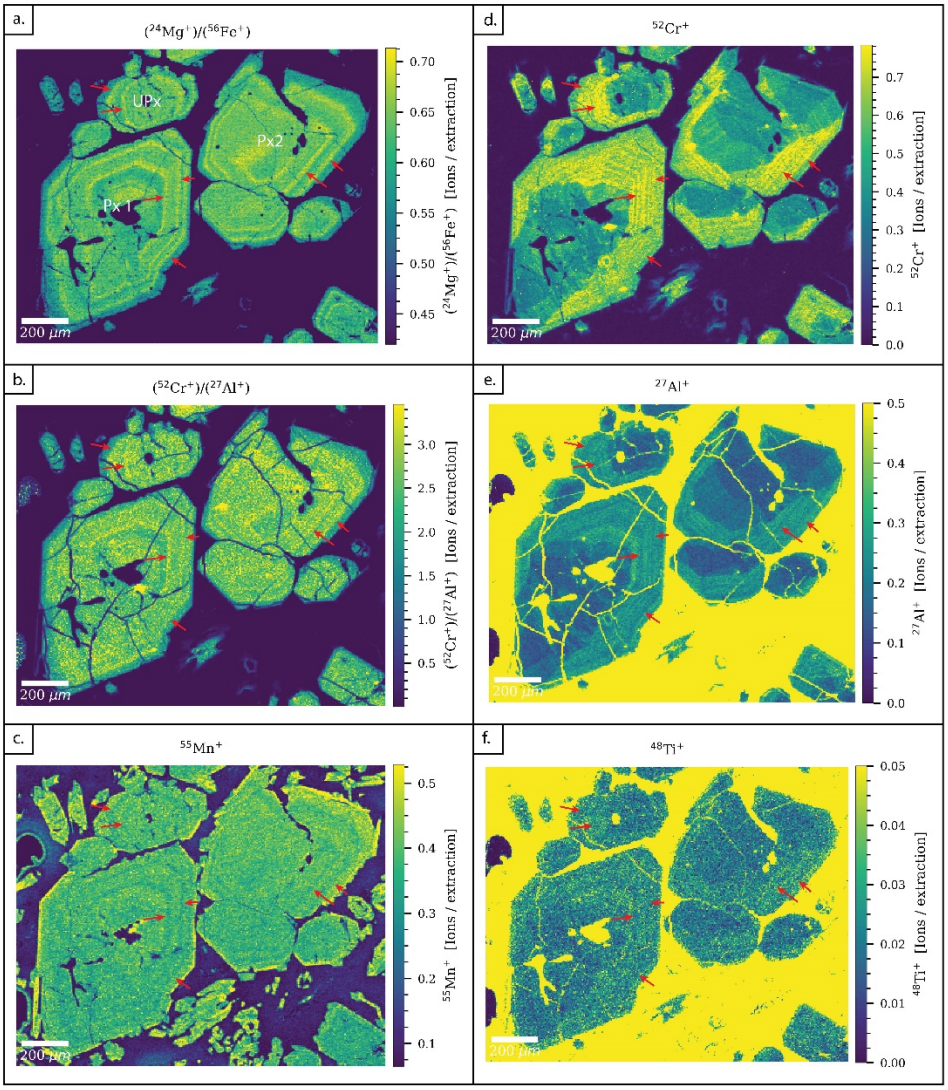

Figure 2.4
Elemental maps of low-Ca pyroxene phenocrysts from sample 15R1. Red arrows in elemental maps point to zones enriched in Mg & Cr and depleted in Fe, Al, Mn, and Ti. Labels (Px 1) and (Px 2) in map (a.) refer to the label used in (Table A.3.) and (Figures 2.6 & A.3.) to identify the individual pyroxene grains. Label (UPx) in map (a.) refers to the label used in (Figure 2.6) as an across grain chemical transect was not made for this pyroxene grain. Unanalyzed Pyroxene (UPx). Elemental maps were produced using LA-ICP-TOF.

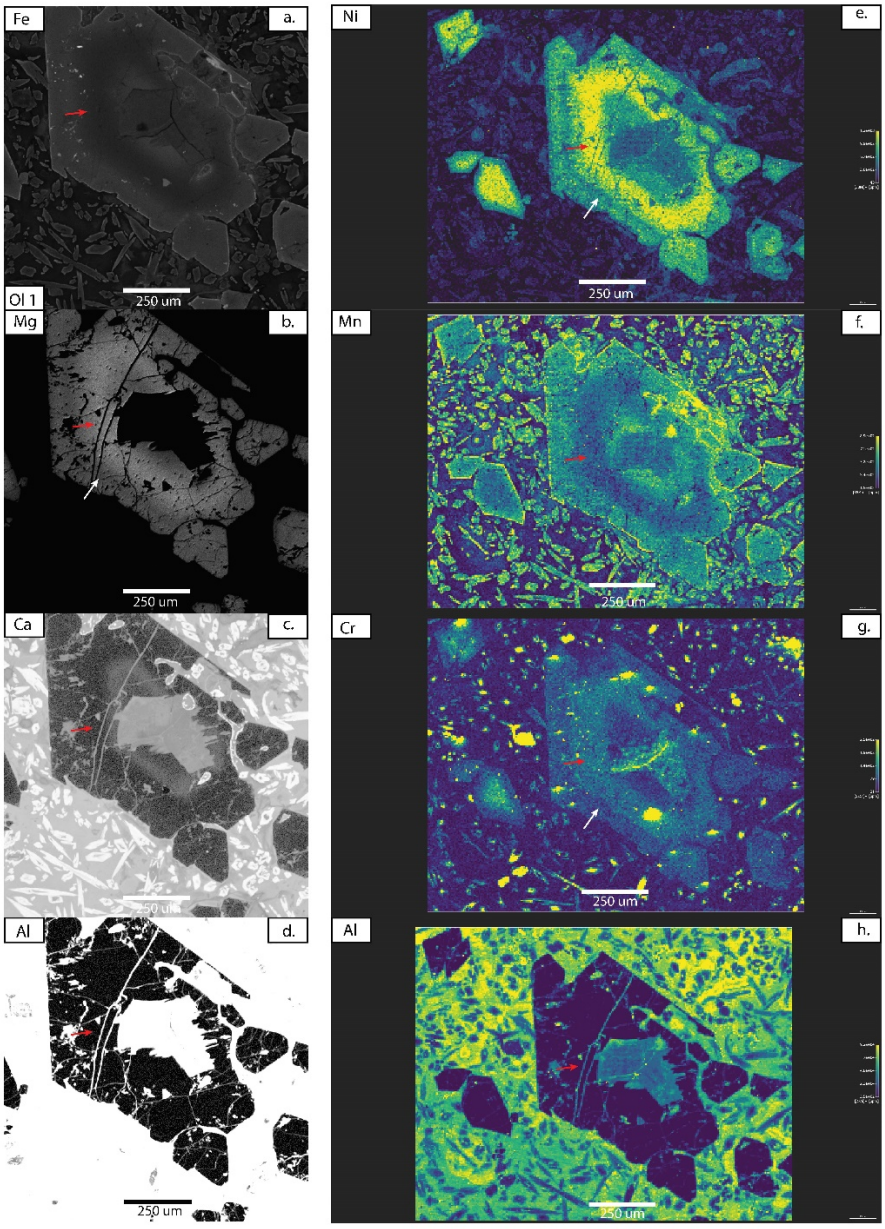

Figure 2.5
Elemental maps of zoned olivine phenocrysts from sample 25R2. Red arrows in elemental maps point to zones enriched in Mg, Cr, and Ni and depleted in Fe, Mn, and Ca. White arrows on maps (b.), (e.), and (g.) points at a zone between the core and rim of this grain, which is more depleted in Mg, Ni, and Cr than the rim of the grain. Label (Ol 1) in the bottom left-hand corner of map (a.) refers to the label used in (Table A.5.) and (Figure A.4) to identify the individual olivine grains. Elemental maps (a.), (b.), (c.), and (d.) were produced using EPMA. Elemental maps (e.), (f.), (g.), and (h.) were generated using LA-ICP-TOF.

A subset of the calcic overgrowths exhibit anomalous enrichments in Al_2O_3 (typical pyroxenes ~4.0 wt%: anomalous overgrowths ~13.5 wt%), as well as high TiO_2 contents. When plotted on the pyroxene quadrilateral (Figure 2.3) cores, standard rims/overgrowths, and aluminous overgrowths from samples 19R2 and 2R3 form three distinct clusters. Samples 15R1 and 25R2 differ from the other samples in this study as pyroxene compositions observed in these samples are more continuous from enstatite to augite (Figure 2.3., data can be found in Table A.3. & A.4.). EPMA and ICP-TOF analyses revealed multiple zoning patterns. Small groundmass pyroxenes in sample 25R2 exhibit the most complex zoning patterns with oscillatory, sector, and patchy zoning patterns appearing in many of these crystals. Groundmass pyroxenes that show oscillatory zoning often contain magnesian cores and calcic rims/overgrowths; however, reverse zoning patterns have also been observed (Figure A.3). Groundmass pyroxenes in samples 2R3, 15R1, and 19R2 exhibit patchy and sector zoning with no evident oscillatory zoning. Some of the larger pyroxene grains in sample 15R1 oscillatory zoning with minor changes in En and Fs components. Mn appears to be following Fe in these oscillatory zoned pyroxenes. These larger pyroxenes also exhibit sector zoning patterns with enriched Cr, Al, and Ti concentrations in sector zones (Figure 2.4). Large pyroxene grains in sample 2R3 display oscillatory zoning with minor changes in En and Fs components; however, sector zoning is not observed in this sample.

In sample 25R2, many olivine grains exhibit oscillatory zoning, with Fo 92-91 cores and less magnesian Fo 90-86 rims (Table 2.5., Figure A.4). Sample 25R2 also included multiple olivine grains with reverse oscillatory zoning, from Fo 88-87 cores to

Fo 91-90 inner-rims, and then to Fo 88-87 outer rims (Figure A.4). This zoning is most apparent in Fe, Mg, Ni, Mn, Cr, and Ca element maps (Figures 2.5 & A.5). In these zones, Mg, Ni, and Cr exhibit a positive correlation with each other, while Fe, Mn, and Ca also show a positive correlation with each other. These two elemental groups exhibit an inverse correlation with each other. Olivine zoning was not observed in any samples other than 25R2.

2.6. Discussion

2.6.1. Mineralogical and Mineral Chemistry Variations

The majority of the Expedition 352 boninite samples examined in this study and recent studies (e.g., Whattam et al. 2020) exhibit phenocryst and matrix mineral compositions consistent with fractional crystallization. The most common phenocryst assemblages encountered are enstatite ± olivine, sometimes enclosing Cr-spinel, with groundmass pigeonite and, in some cases, late-forming augitic clinopyroxene. Plagioclase is only encountered as a matrix phase in the highly differentiated high-Mg andesites/dacites, and always in association with augite. These assemblages are consistent with the progressive crystallization of magnesian boninite parental magmas, as has been documented by Umino (1986), Arculus et al. (1992), and Dobson et al. (2006).

However, a subset (~10%) of our samples, all at different stratigraphic levels, preserve phenocrysts and groundmass crystals that show unusual, complex zoning and overgrowth textures (Figure A.2). While both Umino (1986) and Dobson et al. (2006) report textural evidence for rapid crystallization (i.e., skeletal and feathery morphologies

in microphenocrysts of clinopyroxene), neither study reports pyroxene overgrowth textures in their Chichijima boninite suites, and neither study reports pyroxene compositions with Al_2O_3 or TiO_2 contents as high as those encountered in the Al-rich overgrowths in our Expedition 352 samples. The only study to report textures similar to those observed in this subset of boninite samples from expedition 352 is Ohnenstetter and Brown (1992). The rocks examined in that study were recovered from a glassy boninite dike in New Caledonia and exhibit similar pyroxene zoning, overgrowth textures, and crystal morphologies. The key differences between the samples from that study and the samples from this study are: (1.) the lack of olivine in the boninite dyke, (2.) oscillatory zoning in the boninite dyke is only observed in microphenocrysts of orthopyroxene and skeletal clinoenstatite crystals, (3.) the appearance of tschermakitic amphibole overgrowths on the pyroxene grains.

2.6.2.The Formation of Ca-Tschermak Pyroxenes

The subset of samples, which are the focus of this study, all contain late crystallizing clinopyroxene overgrowths, which are appropriately classified as overgrowths and not growth zones. These are easily distinguished by their elevated Al and Ti contents and are similar to late crystallizing clinopyroxenes observed in experimental studies on quartz normative lunar basalts (Grove and Bence 1977) and studies of natural boninite samples (Ohnenstetter and Brown 1992; Dobson et al. 2006). These overgrowths are believed to form due to the lack of Al-rich phases like plagioclase crystallizing prior to eruption. The melt thus becomes enriched in Al and Ti, which is then incorporated into the pyroxenes during rapid crystallization caused by undercooling,

similar to the way in which tschermakitic amphiboles formed in the New Caledonia boninite dike (i.e., Ohnenstetter and Brown 1992). It should also be noted that these pyroxene overgrowths often become more Al and Ti-rich towards the rim. This phenomenon is likely due to the rapid crystallization of pyroxene, depleting the crystal interface in compatible elements, and enriching it with incompatible and slow-diffusing elements like Al and Ti. During this rapid crystallization process, Al substitutes into the tetrahedral site in place of Si, while Ti substitutes into the M1 site to charge balance the crystal (Ubide et al. 2019; Masotta et al. 2020).

The fact that tschermakitic amphibole formed in a boninite dike from but not in the expedition 352 samples is most likely due to the different conditions that the dike and lavas would have experienced during cooling and emplacement. The key difference was most likely the difference in depth at with the lavas were crystallizing. At low pressures, amphiboles will not form, and the lack of amphibole in the lavas indicates that crystallization was likely occurring at pressures below 2-3 kb (Rutherford and Hill 1993; Carmichael 2002; Davidson et al. 2007; Ridolfi et al. 2010). Water contents must have still been high enough the suppress plagioclase crystallization since plagioclase is not observed in any of these samples. Thus, it is unlikely that lower water contents in the lavas would have much of an effect on the formation of amphibole.

2.6.3.Pyroxene Zoning

Pyroxene can exhibit normal, reverse, sector, oscillatory, or patchy zoning depending on the magmatic conditions in which it forms (Streck 2008). Normal zoning in pyroxenes is related to fractional crystallization of the parent melt or high degrees of

undercooling during crystallization (Shea and Hammer 2013; Benard et al. 2018), whereas reverse zoning is associated with reversals in magma composition (e.g., magma mixing) or abrupt changes in crystallization conditions (Streck 2008; Saunders et al. 2012; Petrone et al. 2016, 2018; Singer et al. 2016). Previous studies suggest that oscillatory zoning in pyroxenes can be driven by rapid crystallization and undercooling (Ohnenstetter and Brown 1992; Benard et al. 2018), based on plagioclase crystallization models (i.e., Ghiorso 1987; L'Heureux and Fowler 1996). In these models, less compatible elements (e.g., Cr, Al, Ti) are enriched near the crystal interface and then incorporated into the crystal as crystallization continues. This process repeats as more compatible elements (e.g., Mg, Ca) diffuse toward the interface, and less compatible elements are incorporated into the crystal, resulting in oscillatory zoning. However, some studies hypothesize that oscillatory zoning in pyroxenes is related to magma mixing events (i.e., Petrone et al. 2016, 2018; Ubide and Kamber 2018; Ubide et al. 2019). Sector zoning in pyroxene forms in response to modest degrees of undercooling (e.g., Shea and Hammer 2013; Ubide and Kamber 2018; Ubide et al. 2019; Masotta et al. 2020). Patchy zoning in pyroxenes is related to changes in pressure, temperature, and H_2O content in the melt (Crabtree and Lange 2010; Shea and Hammer 2013; Waters and Lange 2017).

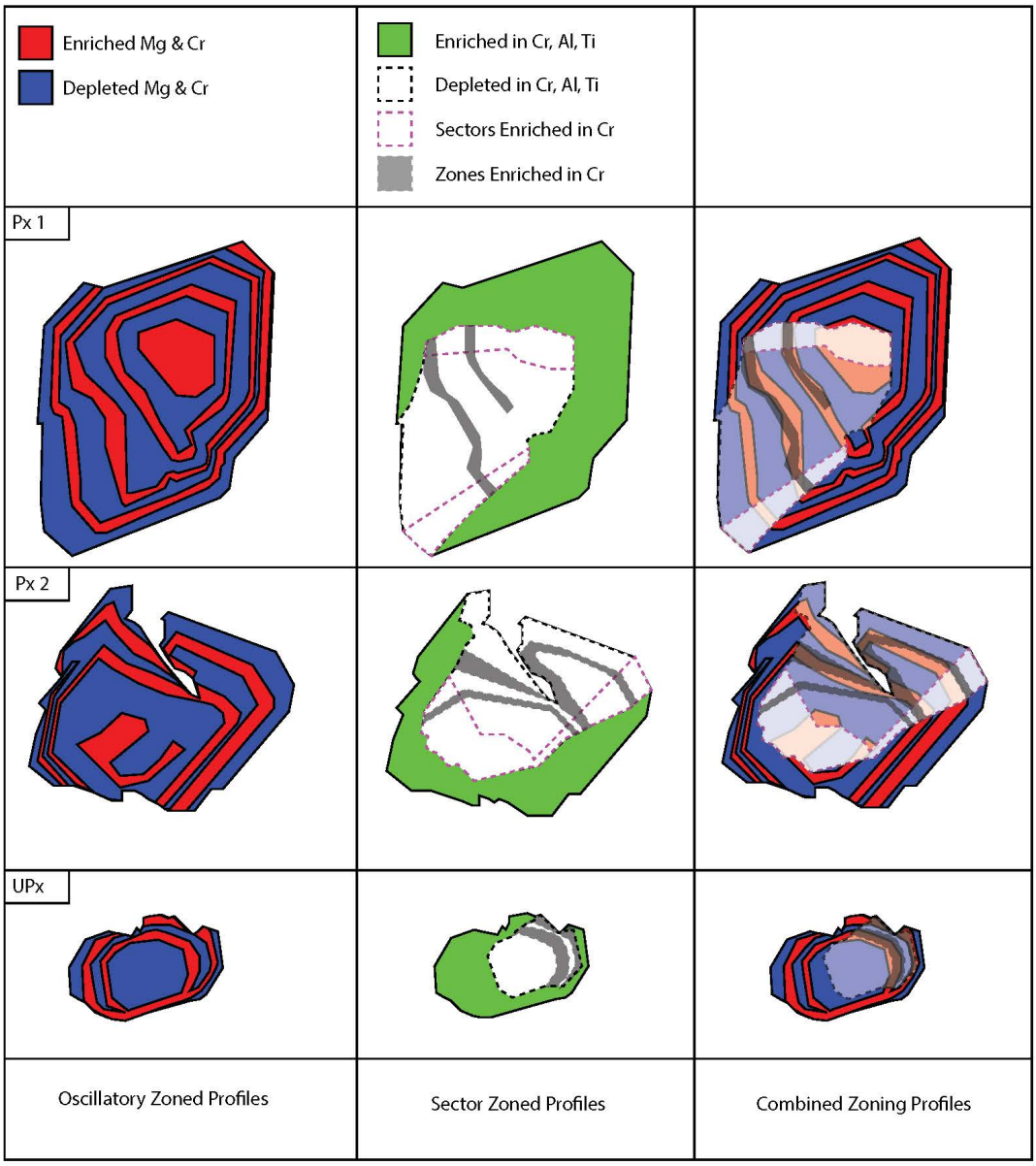

Figure 2.6
Drawn models of the zoning patterns observed in low-Ca pyroxene phenocrysts from sample 15R1 (shown in Figure 2.4). Drawings in the first column highlight the oscillatory zoning patterns observed in Mg and Cr. Drawings in the second column highlight the sector zoning pattern observed in Cr, Al, and Ti. Drawings in the last column combine the zoning profiles so they can be compared with each other. Labels (Px 1) and (Px 2) refer to the labels used in (Table A.3.), (Figure 2.4), and (Figure A.3) to identify the individual pyroxene grains. Label (UPx) refers to the label used in (Figure 2.4) as an across grain chemical transect was not made for this pyroxene grain. Unanalyzed Pyroxene (UPx).

Samples from this study contain examples of each of these pyroxene zoning patterns, indicating that these samples experienced a wide range of crystallizing conditions during their formation. The appearance of groundmass pyroxenes with low-Ca cores and calcic overgrowths in each sample is likely related to rapid crystallization driven by undercooling upon ascent and eruption. As undercooling can be caused by changes in temperature or pressure, we suggest that the undercooling events that generated the calcic overgrowths were the result of a change in pressure and likely changed the H_2O composition of the melt (e.g., Shea and Hamer 2013; Waters and Lange 2017). This process would have resulted in conditions perfect rapid nucleation of pyroxene and the formation of patchy and sector zoning patterns observed in groundmass pyroxenes from this study. These events most likely occurred during or shortly before the eruption of these lavas, as the ascent to the surface would have to result in a change in pressure.

Two of the samples from this study (2R3 and 15R1) contain zoned low-Ca pyroxene phenocrysts. Single element maps of multiple pyroxene phenocrysts in sample 15R1 reveal complex sector and oscillatory zoning patterns, which vary from element to element. Some divalent cations (e.g., Mg, Fe, Mn) exhibit oscillatory zoning patterns while Al, Cr, and Ti exhibit sector zoning patterns (with some variation in the Cr zoning patterns) (Figures 2.4 and 2.6). Sector zoning of Al, Cr, and Ti has been observed in recent studies (i.e., Barnes et al. 2016; Ubide and Kamber 2018; Mao et al. 2019; Ubide et al. 2019; Masotta et al. 2020) and has been attributed the sluggish kinetic effects on pyroxene crystallization during moderate degrees of undercooling ($\Delta T<32$ ºC).

Chemical data from the sector zoned pyroxenes in this study revealed a positive correlation between Al, Cr, and Ti in most of the sector zones. Similar relationships are observed in undercooled boninite dikes from New Caledonia (Ohnenstetter and Brown 1992). Thus, it is likely that undercooling did drive much of the crystallization in these low Ca pyroxenes, resulting in sector zoning due to the crystal kinetics, substitution, and charge balancing processes discussed in Ubide et al. (2019). However, correlations between the Mg/Fe and Cr/Al ratios in these crystals suggest that these pyroxene grains have experienced a more complex crystallization history than consistent undercooling. Elemental maps reveal that high Mg/Fe and Cr/Al oscillations are also correlated with Cr enriched and Al depleted zones, which cut across the sector zones (Figure 2.6). These oscillations suggest changes occurred in the magmatic system at multiple points in time, which led to the sector zoning patterns to stop briefly, and enriched the melt at the crystal interface with Mg and Cr. Based on the observations from previous studies (Petrone et al. 2016, 2018; Singer et al. 2016; Ubide and Kamber 2018; Ubide et al. 2019; Masotta et al. 2020), magma mixing between primitive and evolved boninite endmembers could cause an increase in temperature and enrich the melt in Mg and Cr (Figure 2.7).

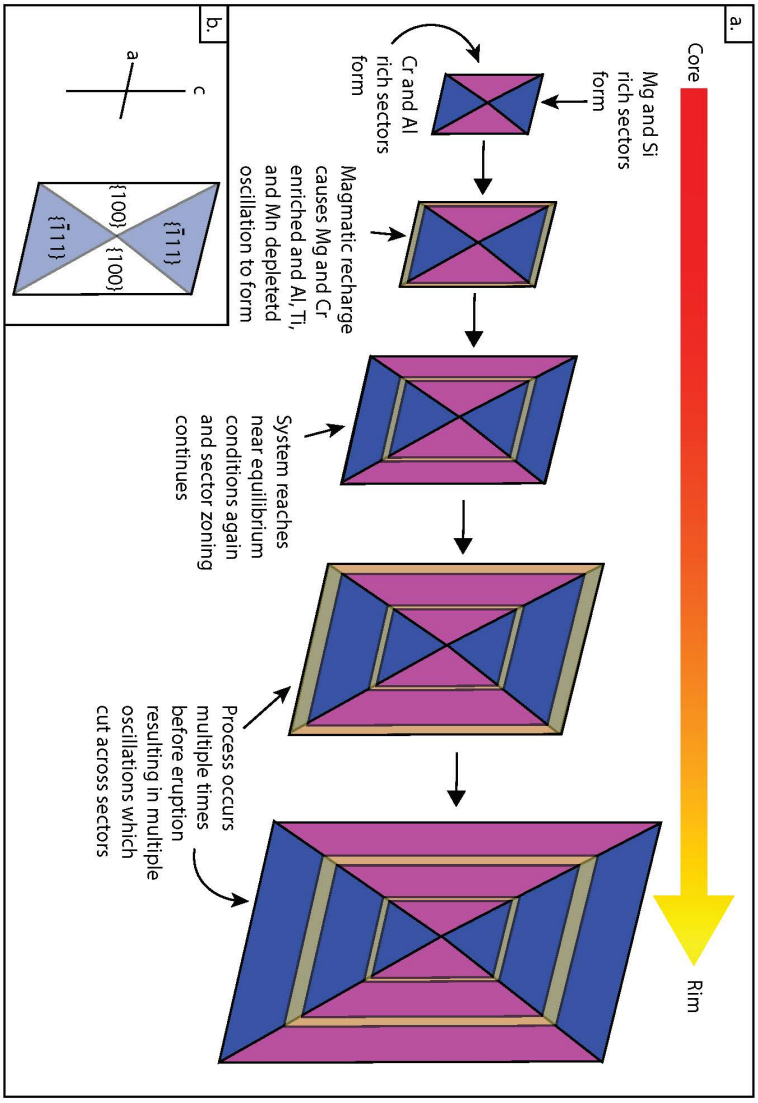

Figure 2.7
Idealized crystallization model for the development of complex pyroxene zoning patterns observed in this study. (a.) Idealized pyroxene crystallization history showing the development of the sector and oscillatory zoning profiles as the crystal grows in an open igneous system. Progression from core to rim is indicated above the models. Crystal shape and sector zones based on the 2D model in (b.) (b.) Hypothetical 2D model of the crystal of a pyroxene crystal (cutting through the center of the crystal) revealing the sector zoning pattern along the a- and c- axis (the {-111} and {100} prism forms). Modified from Ubide et al. (2019). Note this model is not meant to show the exact zoning profiles observed in pyroxenes from sample 15R1 (Figure 2.4) as we do not know the exact angle in which those crystals were cut and polished during sample preparation. This model is only meant to show what the zoning profile would look like in a perfectly cut crystal, based on the hypothesized open-system processes from this paper.

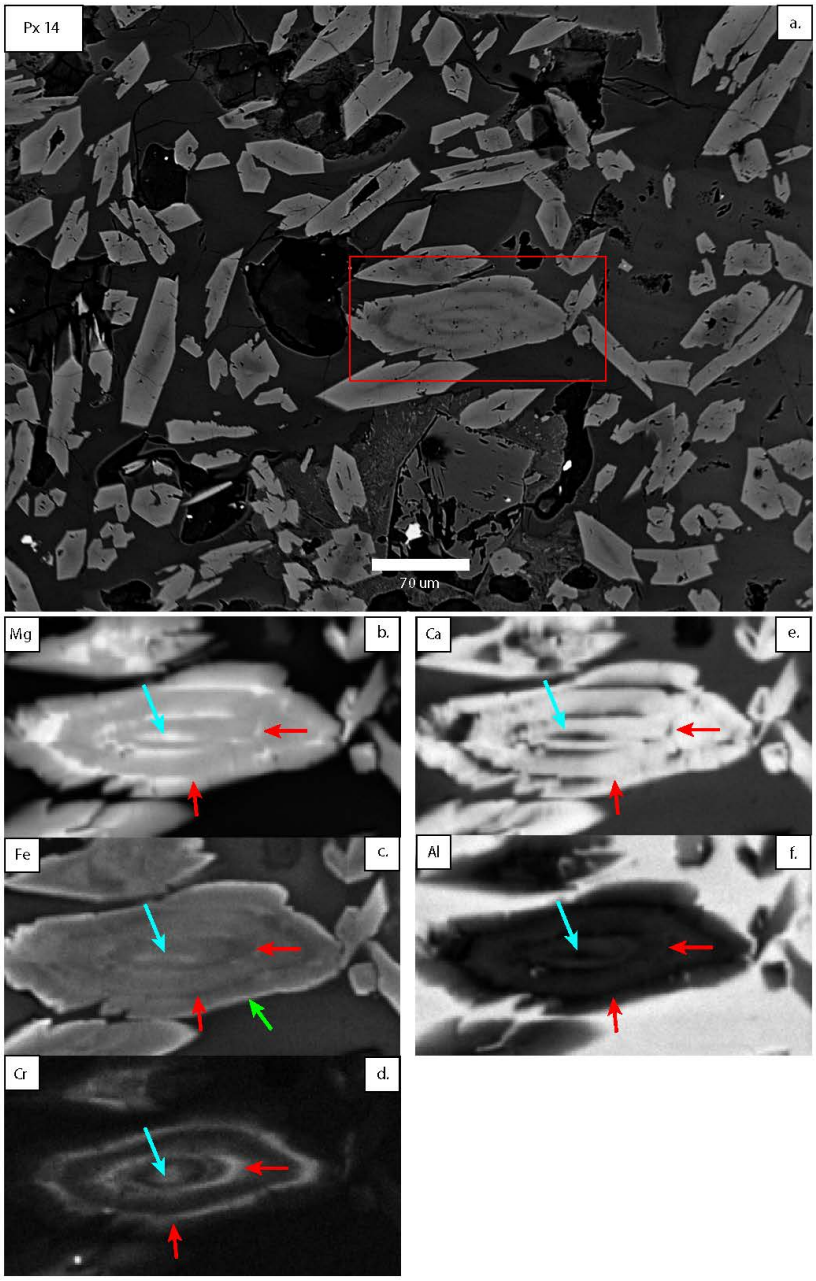

Figure 2.8
BSE image and elemental maps of zoned groundmass clinopyroxene from sample 25R2. The red box in the BSE image (a.) shows the area which was analyzed in elemental maps (b.), (c.), (d.), (e.), and (f.). Red Arrows in the elemental maps point to Mg & Cr enriched zones in the pyroxene. Blue arrows in the elemental maps point to Mg, Fe, and Cr rich core of the grain, which is depleted in Ca and Al. Green arrow in elemental map (c.) points to Fe enrichment around the edge of the grain. Label (Px 14) in the top right-hand corner of map (a.) refers to the label used in (Table A.3.) and (Figure A.3) to identify the individual pyroxene grains.

Oscillatory zoning is also observed in some of the groundmass pyroxene grains from sample 25R2. Since zoning indicates that other groundmass pyroxenes formed during an undercooling event, this may indicate the oscillatory zoning in pyroxenes can be driven by rapid crystallization and undercooling as is suggested by Ohnenstetter and Brown (1992) and Benard et al. (2018). If this process were controlling the oscillatory zoning in sample 25R2, we would expect incompatible elements like Cr and Al to exhibit a positive correlation with each other. However, the opposite is observed: Cr follows Mg, and Al follows Fe and Ca (Figure 2.8). This kind of chemical relationship is what one would expect during mixing events, in which the crystals are interacting with multiple injections of magmas. Such patterns have been interpreted as mixing effects in both experimental and natural studies on pyroxene zoning (Ubide and Kamber 2018; Ubide et al. 2019; Masotta et al. 2020). This indicates that sample 25R2 contains two groups of groundmass pyroxenes, a group that formed during a magma mixing event and a group that formed during an undercooling event shortly before or during the eruption.

2.6.4.Olivine Zoning and Xenocrysts

Olivine zoning usually appears as normal or reverse zoning in the Mg-Fe composition. However, oscillatory zoning can also be observed in minor elements (i.e., P, Al, and Cr) (Costa and Chakraborty 2004; Costa and Dungan 2005; Costa et al. 2008; Milman-Barris et al. 2008; Kahl et al. 2011, 2013; Shea et al. 2015a., 2015b., 2019). Olivine grains from this study appear to be unique in the way that they exhibit oscillatory zoning in both major (i.e., Mg and Fe) and minor elements (i.e., Ca, Cr, Mn, and Ni) (Figure 2.5, Figures A.4 & A.5). Our elemental maps reveal two elemental zoning groups

(Group 1 (Mg, Ni, Cr), Group 2 (Fe, Mn, Ca)), which exhibit an inverse correlation (i.e., as group 1 concentrations increase, group 2 concentrations decrease). Our elemental maps reveal oscillatory zoning patterns with respect to Fo content, which is also evident in the compositional transect collected across this grain (Figure 2.5, Figures A.4 & A.5).

Oscillatory zoning in olivine with respect to elements such as P, Al, and Cr is thought to be caused too rapid crystallization, which enriches the boundary layer in minor elements because they are incompatible in olivine and slow diffusing (Milman-Barris et al. 2008; Shea et al. 2015b., 2019). Shea et al. (2015b.) suggest that a similar process might also cause oscillations in the Fo content of olivine, which are then lost due to the rapid diffusion of Mg and Fe during re-equilibration. However, if rapid crystallization was the cause for the Fo oscillations in the olivines examined in this study, then Cr abundance patterns should correlate with those of Fe, Ca, and Mn, instead of with more compatible and fast diffusing elements like Mg and Ni. It should also be noted that Al zoning was not observed in any of the olivine grains from this study, further supporting the hypothesis that this zoning was not caused by rapid crystallization (Figure 2.5). Based on our geochemical observations, and other shipboard and post-cruise observations on Expedition 352 samples (Reagan et al. 2015; 2017; see 2.6.6. below), it is probable that the olivine zoning in this sample records magma mixing events which episodically enriched the melts in Mg, Ni, and Cr.

The large, xenocrystic olivines observed in sample 25R2 likely came from a cumulate pile within an evolving boninitic magmatic system. That these xenocrysts have a consistent composition of Fo 88 suggests that they formed in equilibrium with a melt

more evolved melt than its current host. The smaller, zoned olivines in 25R2, with Fo 92-91 cores and rims at ≈ Fo 88, were likely carried into the magma chamber in a more primitive boninite melt. Zoning developed in these grains as a byproduct of this mixing event, resulting in rims that approach the compositions of the xenocrysts. A similar process can also account for the reverse zoned olivines, which were likely growing suspended in the magma chamber or the cumulate pile, as reflected in their Fo 88-87 cores. The rims of these olivines approach but never reach compositions as magnesian as olivine cores from the primitive boninite melt, due most likely to the hybridized composition of the mixed magma that they interacted with.

2.6.5.Magma Mixing

Mineral chemistry and mineral zoning patterns observed in this study indicate that boninite crystallization occurs in a dynamic and continuously evolving magmatic system. In this magmatic system, crystallization occurs as the magma ascends, and the pressure and temperature decrease (i.e., undergoing undercooling driven crystallization). This process causes sector and patchy zoning in the groundmass pyroxenes, as well as, the sector zoning patterns in the large low-Ca pyroxenes from 15R1. However, periodically this system also experiences mafic (i.e., primitive boninite magma) re-charge events within a magma chamber, resulting in mixing between primitive and evolved magmas. These re-charge events increase the temperature of the magma chamber (i.e., decreasing the amount of undercooling) and enrich the evolving magma in elements (e.g., Mg, Ni, Cr). This results in the oscillatory zoning patterns observed in groundmass pyroxenes from sample 25R2 and large low-Ca pyroxenes from samples 15R1 and 2R3. Re-charge

events also cause normal, reverse, and oscillatory zoning in olivine and resorption textures on the rims olivine xenocryst.

Zoning patterns created by mixing events are often used to determine the time between mixing events and eruptions. Mg-Fe diffusion across pyroxene and olivine zoning profiles has been used in other studies to place constraints on the time between mixing events and eruptions (Costa and Dungan 2005; Costa et al. 2008; Kahl et al. 2011, 2013; Saunders et al. 2012; Shea et al. 2015a., 2015b.; Petrone et al. 2016, 2018; Singer et al. 2016). Data from the transects conducted in this study are not detailed enough to calculate reliable times; however, some inferences can be made based on the elements which show zoning in the olivines. Mg and Fe are considered fast diffusing elements in olivine (Costa and Chakraborty 2004; Costa et al. 2008; Shea et al. 2015a., 2015b.) and redistribute rapidly through crystals during solid-state re-equilibration with the evolving host magma. This high diffusivity is likely why the olivine xenocrysts do not exhibit zoning, as these crystals appear to have resided in the magma chamber for an extended period of time and have thus re-equilibrated with the host magma in the chamber. Thus, the presence of complex Mg-Fe oscillatory, normal, and reverse zoning in olivine phenocrysts, as we have found in this study, indicates that the events which produced them occurred shortly before eruption before the crystals had time to re-equilibrate with the melt. Based on calculations of olivine residence time from previous studies, in which less complex zoning was observed in the olivine grains (i.e., Costa and Dungan 2005; Kahl et al. 2011, 2013; Shea et al. 2015a., 2015b.), we suggest that the mixing events which led to these zoning features occurred within a couple of months to a couple of

years before the eruption. While this hypothesis will require more detailed analyses of olivines to confirm, the likely short duration between mixing and eruption provides evidence that mafic recharge events may have driven the eruption of lavas through this section of the U1439C core.

2.6.6.Insights from Petrography, Stratigraphy, and Petrology

Shipboard portable x-ray fluorescence (PXRF) chemostratigraphic data (Ryan et al. 2017) document high chemical variability in specific horizons of the U1439C core that are suggestive of mingled or mixed melts. These "mixing" horizons in the core show a reasonable alignment with the stratigraphic positions of the samples exhibiting anomalous mineral zoning (Figure A.6). Complex interactions among rising boninitic melts are also suggested by some of the macro-scale fabrics found in the Hole U1439C and U1442A cores. Both cores preserve long (10 cm – 1 m scale) sections that demonstrate magma mingling fabrics, in which two different boninite melts are vertically intertwined, with visual evidence for interaction along with their margins (Reagan et al. 2015; 2017; Figure A.7). As well, at the scale of standard thin sections, we see evidence for interaction, and incomplete mixing between more and less phenocryst-rich boninitic melts (e.g., Reagan et al. 2015, Figure A.8).

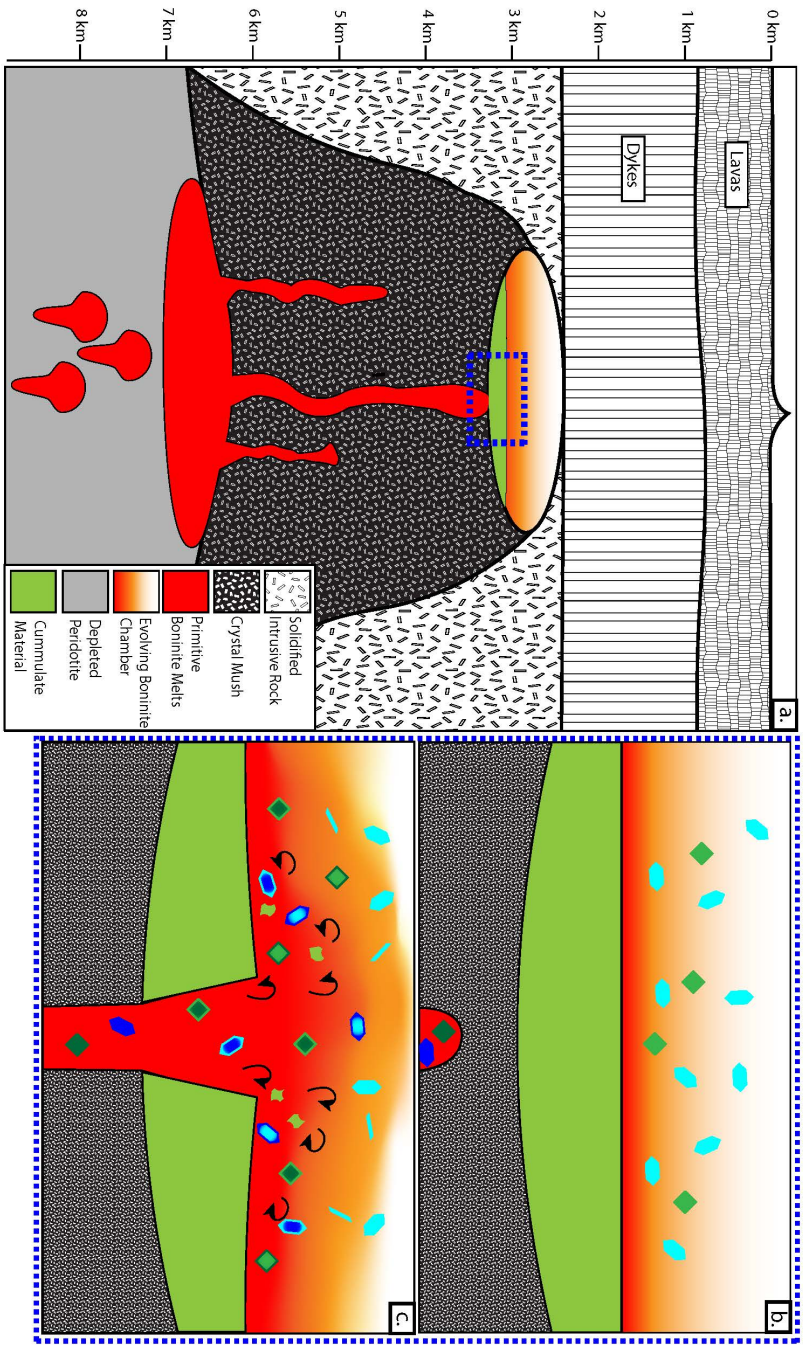

Figure 2.9
Boninite magma chamber and mixing model. Primitive boninite melts pond beneath the fore-arc crust before ascending through a crystal mush zone (a.) Primitive melts begin to crystallize as they migrate through the crystal mush, ascending towards a fractionating magma chamber with a cumulate pile (b.). Primitive melts enter the chamber and dislodging cumulate material (c.). Primitive plume ascends into the evolved magma chamber resulting in magma mixing, along with reverse and normal zoning patterns (c.).

These observations, combined with the data from this study, indicate that magma mixing plays a significant role in the evolution of boninite magmas. The high chemical variability of some core sections observed in chemostratigraphic data suggests that magmas at significantly different points in the fractionation process were present in the magma chamber and erupt together. Petrologic and chemical evidence from olivine and pyroxene indicate that mixing events occur within a magma chamber and, in some cases, may occur multiple times. The lack of amphibole crystallization in the samples suggests that melts were crystallizing at pressures below 2-3 kb (i.e., shallower than 6-9 km). The observation of macro- and microscale magma mingling interfaces, as well as preserved Fe-Mg oscillations in olivine grains, show that mixing events occur shortly before or during eruptions.

We believe that this evidence shows that boninite magma chambers are located at shallow depths in the middle to the upper crust. Chemical zoning within these chambers, along with mixing events, could account for the chemical variability observed in chemostratigraphy. These chambers also contain crystal cumulate piles that are overturned during mixing events, resulting in xenocryst crystal contamination (Figure 2.9).

2.7. Conclusions

The appearance of high Al and Ti pyroxene overgrowths in these samples is significant evidence that these lavas experienced high levels of undercooling just prior to or during eruption. This undercooling is likely related to the ascent to the surface during an eruption, as this process would undoubtedly result in pressure and temperature

changes and devolatilization of the magma (i.e., the pressure and temperature changes along with the devolatilization cause undercooling driven crystallization in the magma) (e.g., Grove and Bence 1977; Ohnenstetter and Brown 1992; Crabtree and Lange 2010; Shea and Hammer 2013; Waters and Lange 2017). Sector zoning in low Ca pyroxenes provides further support to the hypothesis that undercooling controlled a large portion of crystallization observed in this study. This fact is not surprising as undercooling is expected to occur as magmas ascend to the surface and erupt. Whattam et al. (2020) suggest that boninite melts ascend to the surface rapidly since crystallization occurs at similar temperatures to fore-arc basalts collected during expedition 352, but at much lower pressures. Thus, the boninite melts ascend fast enough that they experience little to no heat loss until they are near the surface, perfect for crystallization driven by undercooling that results from changing pressures.

Oscillatory zoned pyroxenes and olivines in these samples indicate that undercooling is not have been the only process affecting these crystals prior to eruption. These pyroxene patterns probably formed during magma mixing events, which altered the temperature and chemical composition of the melts. The mixing events most likely occurred between boninitic melts which were at different stages of crystallization, resulting in less drastic chemical changes than those observed in recent pyroxene zoning studies (e.g., Barnes et al. 2016; Mao et al. 2019; Ubide and Kamber 2018; Ubide et al. 2019; Masotta et al. 2020). More drastic chemical changes, like those observed in oscillatory zoned groundmass pyroxenes from sample 25R2, are probably due to mixing with more evolved melts (e.g., high-Mg andesite or andesite melts) or in cases where

mixing causes undercooling and the crystals are affected by both processes simultaneously.

Olivine zoning in sample 25R2, as well as the presence of olivine xenocrysts, is the most substantial evidence for mixing in this study. These zoned olivines and xenocrysts suggest that this sample came from a magma chamber that contained evolved boninite magma and a cumulate pile rich in olivine. Primitive magma injected into this magma chamber led to partial mixing of the two melts, resulting in oscillatory, normal, and reverse zoning observed in this study. The mixing event occurred shortly before eruption due to the preservation of zoning in fast diffusing elements like Mg, Fe, and Ni. Observed magma mingling interfaces in the core and thin sections indicate that mixing often occurred shortly before or during eruptions. These combined observations show that boninite eruptions were often driven by magma re-charge and mixing events.

Boninite magma chambers likely located at shallow depths in the middle to the upper crust, as amphibole would have formed if chambers were located deeper. Chemical zoning within these chambers, along with mixing events, probably cause chemical variability observed in chemostratigraphy. Crystal cumulate piles are overturned during mixing events, resulting in xenocryst crystal contamination (Figure 2.9). Large mixing events most likely destabilize the magma chamber, resulting in devolatilization and eruption (e.g., Sparks et al. 1977; De Campos et al. 2011; Kahl et al. 2011, 2013; Druitt et al. 2012; Petrone et al. 2018; Rossi et al. 2019). Small mixing events lack the energy to destabilize the chamber, resulting in repeated oscillations (i.e., patterns like those observed in low-Ca pyroxenes from samples 2R3 and 15R1) as minerals are affected by

multiple small mixing events.

This study highlights the importance of elemental maps and chemical transects in studies of zoning minerals in igneous systems. These tools allow us to interpret complex zoning patterns in which patterns may vary for each element. This study also highlights the complexity of magmatic evolution prior to eruption. The processes which affect crystal chemistry may vary between samples, so thorough analysis must be conducted for each sample to interpret the pre-eruptive history of lavas correctly.

2.8. Acknowledgments

Thanks go to Tom Beasley and postdoctoral fellows Sven Holbik and Chris Vidito for invaluable logistical support on the FCAEM EPMA and SEM systems, both for Ryan and all of his GLY 3311C students. Thanks also to the staff at the Kochi Core Repository for their creative aid in identifying suitable Expedition 352 boninite samples for classroom petrographic and EPMA analysis. This project was supported by NSF grants OCE-1558855 and DUE-1323275 to Jeff Ryan and OCE-1558689 to Shervais.

2.9. References

Arculus, R.J., Pearce, J.A., Murton, B.J., and Van der Laan, S.R. (1992) Igneous stratigraphy and major element geochemistry of Holes 786A and 786B. In Proceedings of the Ocean Drilling Program, Scientific Results Vol. 125, pp. 143–169. Ocean Drilling Program, College Station, TX.

Barnes, S.J., Mole, D.R., Le Vaillant, M., Campbell, M.J., Verrall, M.R., Roberts, M.P., and Evans, N.J. (2016) Poikilitic Textures, Heteradcumulates and Zoned Orthopyroxenes in the Ntaka Ultramafic Complex, Tanzania: Implications for Crystallization Mechanisms of Oikocrysts. Journal of Petrology, 57, 1171–1198.

Bédard, J.H., Lauzière, K., Tremblay, A., and Sangster, A. (1998) Evidence for forearc seafloor-spreading from the Betts Cove ophiolite, Newfoundland: oceanic crust of boninitic affinity. Tectonophysics, 284, 233–245.

Bénard, A., Nebel, O., Ionov, D.A., Arculus, R.J., Shimizu, N., and Métrich, N. (2016) Primary silica-rich picrite and high-Ca boninite melt inclusions in pyroxenite veins from the Kamchatka sub-arc mantle. Journal of Petrology, 57, 1955–1982.

Bloomer, S.H. (1979) Mariana arc-trench studies: Petrology of boninites and evidence for a" boninite series". EOS (Amer. Geophys. Union Trans.), 60, 968.

Bloomer, S.H., and Hawkins, J.W. (1987) Petrology and geochemistry of boninite series volcanic rocks from the Mariana trench. Contributions to Mineralogy and Petrology, 97, 361–377.

Cameron, W.E. (1985) Petrology and origin of primitive lavas from the Troodos ophiolite, Cyprus. Contributions to Mineralogy and Petrology, 89, 239–255.

Cameron, W.E., McCulloch, M.T., and Walker, D.A. (1983) Boninite petrogenesis: Chemical and Nd-Sr isotopic constraints. Earth and Planetary Science Letters, 65, 75–89.

Carmichael, I.S. (2002) The andesite aqueduct: perspectives on the evolution of intermediate magmatism in west-central (105–99 W) Mexico. Contributions to Mineralogy and Petrology, 143, 641–663.

Costa, F., and Chakraborty, S. (2004) Decadal time gaps between mafic intrusion and silicic eruption obtained from chemical zoning patterns in olivine. Earth and Planetary Science Letters, 227, 517–530.

Costa, F., and Dungan, M. (2005) Short time scales of magmatic assimilation from diffusion modeling of multiple elements in olivine. Geology, 33, 837–840.

Costa, F., Dohmen, R., and Chakraborty, S. (2008) Time Scales of Magmatic Processes from Modeling the Zoning Patterns of Crystals. Reviews in Mineralogy and Geochemistry, 69, 545–594.

Crabtree, S.M., and Lange, R.A. (2010) Complex Phenocryst Textures and Zoning Patterns in Andesites and Dacites: Evidence of Degassing-Induced Rapid Crystallization? Journal of Petrology, 52, 3–38.

Crawford, A.J., Falloon, T.J., and Green, D.H. (1989) Classification, petrogenesis and tectonic setting of boninites.

Davidson, J., Turner, S., Handley, H., Macpherson, C., and Dosseto, A. (2007) Amphibole "sponge" in arc crust? Geology, 35, 787–790.

De Campos, C.P., Perugini, D., Ertel-Ingrisch, W., Dingwell, D.B., and Poli, G. (2011) Enhancement of magma mixing efficiency by chaotic dynamics: an experimental study. Contributions to Mineralogy and Petrology, 161, 863–881.

Dietrich, V., Emmermann, R., Oberhänsli, R., and Puchelt, H. (1978) Geochemistry of basaltic and gabbroic rocks from the West Mariana basin and the Mariana trench. Earth and Planetary Science Letters, 39, 127–144.

Dobson, P.F., Blank, J.G., Maruyama, S., and Liou, J.G. (2006) Petrology and geochemistry of boninite-series volcanic rocks, Chichi-Jima, Bonin Islands, Japan. International Geology Review, 48, 669–701.

Druitt, T.H., Costa, F., Deloule, E., Dungan, M., and Scaillet, B. (2012) Decadal to monthly timescales of magma transfer and reservoir growth at a caldera volcano. Nature, 482, 77.

Expedition 352 Scientists (2014) International Ocean Discovery Program Expedition 352 Preliminary Report: Testing subduction initiation and ophiolite models by drilling the outer Izu-Bonin Mariana fore arc. International Ocean Discovery Program, 352.

Falloon, T.J., and Crawford, A.J. (1991) The petrogenesis of high-calcium boninite lavas dredged from the northern Tonga ridge. Earth and Planetary Science Letters, 102, 375–394.

Falloon, T.J., Malahoff, A., Zonenshaina, L.P., and Bogdanova, Y. (1992) Petrology and geochemistry of back-arc basin basalts from Lau Basin spreading ridges at 15, 18 and 19 S. Mineralogy and Petrology, 47, 1–35.

Ghiorso, M.S. (1987) Chemical mass transfer in magmatic processes. 3. Crystal growths, chemical diffusion and thermal diffusion in multicomponent silicate melts. Contributions to Mineralogy and Petrology, 96, 291–313.

Grove, T.L., and Bence, A.E. (1977) Experimental study of pyroxene-liquid interaction in quartz-normative basalt 15597. In Lunar and Planetary Science Conference Proceedings Vol. 8, pp. 1549–1579.

Hickey, R.L., and Frey, F.A. (1982) Geochemical characteristics of boninite series volcanics: implications for their source. Geochimica et Cosmochimica Acta, 46, 2099–2115.

Humphreys, M.C.S., Christopher, T., and Hards, V. (2009) Microlite transfer by disaggregation of mafic inclusions following magma mixing at Soufrière Hills volcano, Montserrat. Contributions to Mineralogy and Petrology, 157, 609–624.

Ishikawa, T., Umino, S., and Kazuya, N. (2002) Boninitic volcanism in the Oman ophiolite: Implications for thermal condition during transition from spreading ridge to arc. Geology, 30, 899–902.

Ishikawa, T., Fujisawa, S., Nagaishi, K., and Masuda, T. (2005) Trace element characteristics of the fluid liberated from amphibolite-facies slab: Inference from the metamorphic sole beneath the Oman ophiolite and implication for boninite genesis. Earth and Planetary Science Letters, 240, 355–377.

Ishizuka, O., Taylor, R.N., Yuasa, M., and Ohara, Y. (2011) Making and breaking an island arc: A new perspective from the Oligocene Kyushu-Palau arc, Philippine Sea. Geochemistry, Geophysics, Geosystems, 12.

Johanssen, A. (1937) A descriptive petrography of the igneous rocks: The intermediate rocks. University of Chicago Press, 3.

Kahl, M., Chakraborty, S., Costa, F., and Pompilio, M. (2011) Dynamic plumbing system beneath volcanoes revealed by kinetic modeling, and the connection to monitoring data: An example from Mt. Etna. Earth and Planetary Science Letters, 308, 11–22.

Kahl, M., Chakraborty, S., Costa, F., Pompilio, M., Liuzzo, M., and Viccaro, M. (2013) Compositionally zoned crystals and real-time degassing data reveal changes in magma transfer dynamics during the 2006 summit eruptive episodes of Mt. Etna. Bulletin of Volcanology, 75, 692.

Kelemen, P.B., Johnson, K.T.M., Kinzler, R.J., and Irving, A.J. (1990) High-field-strength element depletions in arc basalts due to mantle–magma interaction. Nature, 345, 521–524.

Klemme, S., Blundy, J.D., and Wood, B.J. (2002) Experimental constraints on major and trace element partitioning during partial melting of eclogite. Geochimica et Cosmochimica Acta, 66, 3109–3123.

Kuroda, N., and Shiraki, K. (1975) Boninite and related rocks of Chichi-jima, Bonin Islands, Japan. Rep. Fac. Sci. Shizuoka Univ., 10, 145–155.

Kyser, T.K., Cameron, W.E., and Nisbet, E.G. (1986) Boninite petrogenesis and alteration history: constraints from stable isotope compositions of boninites from Cape Vogel, New Caledonia and Cyprus. Contributions to Mineralogy and Petrology, 93, 222–226.

L'Heureux, I., and Fowler, A.D. (1996) Isothermal constitutive undercooling as a model for oscillatory zoning in plagioclase. The Canadian Mineralogist, 34, 1137–1147.

Li, H.-Y., Taylor, R.N., Prytulak, J., Kirchenbaur, M., Shervais, J.W., Ryan, J.G., Godard, M., Reagan, M.K., and Pearce, J.A. (2019) Radiogenic isotopes document the start of subduction in the Western Pacific. Earth and Planetary Science Letters, 518, 197–210.

Li, Y.-B., Kimura, J.-I., Machida, S., Ishii, T., Ishiwatari, A., Maruyama, S., Qiu, H.-N., Ishikawa, T., Kato, Y., Haraguchi, S., and others (2013) High-Mg Adakite and Low-Ca Boninite from a Bonin Fore-arc Seamount: Implications for the Reaction between Slab Melts and Depleted Mantle. Journal of Petrology, 54, 1149–1175.

Mao, Y.-J., Barnes, S.J., Qin, K.-Z., Tang, D., Martin, L., Su, B., and Evans, N.J. (2019) Rapid orthopyroxene growth induced by silica assimilation: constraints from sector-zoned orthopyroxene, olivine oxygen isotopes and trace element variations in the Huangshanxi Ni–Cu deposit, Northwest China. Contributions to Mineralogy and Petrology, 174, 33.

Masotta, M., Pontesilli, A., Mollo, S., Armienti, P., Ubide, T., Nazzari, M., and Scarlato, P. (2020) The role of undercooling during clinopyroxene growth in trachybasaltic magmas: Insights on magma decompression and cooling at Mt. Etna volcano. Geochimica et Cosmochimica Acta, 268, 258–276.

Meffre, S., Falloon, T.J., Crawford, T.J., Hoernle, K., Hauff, F., Duncan, R.A., Bloomer, S.H., and Wright, D.J. (2012) Basalts erupted along the Tongan fore arc during subduction initiation: Evidence from geochronology of dredged rocks from the Tonga fore arc and trench. Geochemistry, Geophysics, Geosystems, 13.

Meijer, A. (1980) Primitive Arc Volcanism and a Boninite Series: Examples from Western Pacific Island Arcs. In The Tectonic and Geologic Evolution of Southeast Asian Seas and Islands pp. 269–282. American Geophysical Union (AGU).

Meijer, A., Anthony, E., and Reagan, M. (1982) Petrology of volcanic-rocks from the fore-arc sites. Initial Reports of the Deep Sea Drilling Project, 60, 709–729.

Milman-Barris, M.S., Beckett, J.R., Baker, M.B., Hofmann, A.E., Morgan, Z., Crowley, M.R., Vielzeuf, D., and Stolper, E. (2008) Zoning of phosphorus in igneous olivine. Contributions to Mineralogy and Petrology, 155, 739–765.

Murton, B.J., Peate, D.W., Arculus, R.J., Pearce, J.A., and Van der Laan, S. (1992) Trace-element geochemistry of volcanic rocks from site 786: The Izu-Bonin Forearc. Proceedings of the Ocean Drilling Program Scientific Results, 125, 211–235.

Ohnenstetter, D., and Brown, W.L. (1992) Overgrowth Textures, Disequilibrium Zoning, and Cooling History of a Glassy Four-Pyroxene Boninite Dyke from New Caledonia. Journal of Petrology, 33, 231–271.

Pagé, P., Bédard, J.H., Schroetter, J.-M., and Tremblay, A. (2008) Mantle petrology and mineralogy of the Thetford Mines Ophiolite Complex. Links Between Ophiolites and LIPs in Earth History, 100, 255–292.

Pagé, P., Bédard, J.H., and Tremblay, A. (2009) Geochemical variations in a depleted fore-arc mantle: The Ordovician Thetford Mines Ophiolite. Mantle Dynamics and Crust-Mantle Interactions in Collisional Orogens, 113, 21–47.

Pearce, J.A., and Reagan, M.K. (2019) Identification, classification, and interpretation of boninites from Anthropocene to Eoarchean using Si-Mg-Ti systematics. Geosphere, 15, 1008–1037.

Pearce, J.A., van der Laan, S.R., Arculus, R.J., Murton, B.J., Ishii, T., Peate, D.W., and Parkinson, I.J. (1992) Boninite and harzburgite from Leg 125 (Bonin-Mariana forearc): A case study of magma genesis during the initial stages of subduction. In Proceedings of the ocean drilling program, scientific results Vol. 125, pp. 623–659. Citeseer.

Pearce, J.A., Kempton, P.D., Nowell, G.M., and Noble, S.R. (1999) Hf-Nd element and isotope perspective on the nature and provenance of mantle and subduction components in Western Pacific arc-basin systems. Journal of Petrology, 40, 1579–1611.

Petrone, C.M., Bugatti, G., Braschi, E., and Tommasini, S. (2016) Pre-eruptive magmatic processes re-timed using a non-isothermal approach to magma chamber dynamics. Nature Communications, 7, 12946.

Petrone, C.M., Braschi, E., Francalanci, L., Casalini, M., and Tommasini, S. (2018) Rapid mixing and short storage timescale in the magma dynamics of a steady-state volcano. Earth and Planetary Science Letters, 492, 206–221.

Reagan, M.K., Ishizuka, O., Stern, R.J., Kelley, K.A., Ohara, Y., Blichert-Toft, J., Bloomer, S.H., Cash, J., Fryer, P., Hanan, B.B., and others (2010) Fore-arc basalts

and subduction initiation in the Izu-Bonin-Mariana system. Geochemistry, Geophysics, Geosystems, 11.

Reagan, M.K., Pearce, J.A., Petronotis, K., and Expedition 352 Scientists (2015) Expedition 352 summary. Proceedings of the International Ocean Discovery Program, 352, 1–32.

Reagan, M.K., Pearce, J.A., Petronotis, K., Almeev, R.R., Avery, A.J., Carvallo, C., Chapman, T., Christeson, G.L., Ferré, E.C., Godard, M., and others (2017) Subduction initiation and ophiolite crust: new insights from IODP drilling. International Geology Review, 59, 1439–1450.

Reagan, M.K., Heaton, D.E., Schmitz, M.D., Pearce, J.A., Shervais, J.W., and Koppers, A.A.P. (2019) Forearc ages reveal extensive short-lived and rapid seafloor spreading following subduction initiation. Earth and Planetary Science Letters, 506, 520–529.

Resing, J.A., Rubin, K.H., Embley, R.W., Lupton, J.E., Baker, E.T., Dziak, R.P., Baumberger, T., Lilley, M.D., Huber, J.A., Shank, T.M., and others (2011) Active submarine eruption of boninite in the northeastern Lau Basin. Nature Geoscience, 4, 799.

Ridolfi, F., Renzulli, A., and Puerini, M. (2010) Stability and chemical equilibrium of amphibole in calc-alkaline magmas: an overview, new thermobarometric formulations and application to subduction-related volcanoes. Contributions to Mineralogy and Petrology, 160, 45–66.

Rossi, S., Petrelli, M., Morgavi, D., Vetere, F.P., Almeev, R.R., Astbury, R.L., and Perugini, D. (2019) Role of magma mixing in the pre-eruptive dynamics of the Aeolian Islands volcanoes (Southern Tyrrhenian Sea, Italy). Lithos, 324–325, 165–179.

Rutherford, M.J., and Hill, P.M. (1993) Magma ascent rates from amphibole breakdown: An experimental study applied to the 1980–1986 Mount St. Helens eruptions. Journal of Geophysical Research: Solid Earth, 98, 19667–19685.

Ryan, J.G. (2013) Embedding research practice activities into earth and planetary science courses through the use of remotely operable analytical instrumentation: Interventions and impacts on student perceptions and activities. Geoscience Research and Education: Teaching at Universities. New York: Springer Verlag, 149–162.

Ryan, J.G., Shervais, J.W., Li, Y., Reagan, M.K., Li, H.Y., Heaton, D., Godard, M., Kirchenbaur, M., Whattam, S.A., and Pearce, J.A. (2017) Application of a handheld X-ray fluorescence spectrometer for real-time, high-density quantitative analysis of drilled igneous rocks and sediments during IODP Expedition 352. Chemical Geology, 451, 55–66.

Saunders, K., Rinnen, S., Blundy, J., Dohmen, R., Klemme, S., and Arlinghaus, H.F. (2012) TOF-SIMS and electron microprobe investigations of zoned magmatic orthopyroxenes: First results of trace and minor element analysis with implications for diffusion modeling. American Mineralogist, 97, 532–542.

Shea, T., and Hammer, J.E. (2013) Kinetics of cooling- and decompression-induced crystallization in hydrous mafic-intermediate magmas. Journal of Volcanology and Geothermal Research, 260, 127–145.

Shea, T., Costa, F., Krimer, D., and Hammer, J.E. (2015a) Accuracy of timescales retrieved from diffusion modeling in olivine: A 3D perspective†. American Mineralogist, 100, 2026–2042.

Shea, T., Lynn, K.J., and Garcia, M.O. (2015b) Cracking the olivine zoning code: Distinguishing between crystal growth and diffusion. Geology, 43, 935–938.

Shea, T., Hammer, J.E., Hellebrand, E., Mourey, A.J., Costa, F., First, E.C., Lynn, K.J., and Melnik, O. (2019) Phosphorus and aluminum zoning in olivine: contrasting behavior of two nominally incompatible trace elements. Contributions to Mineralogy and Petrology, 174, 85.

Shervais, J.W., Reagan, M., Haugen, E., Almeev, R.R., Pearce, J.A., Prytulak, J., Ryan, J.G., Whattam, S.A., Godard, M., Chapman, T., and others (2019) Magmatic Response to Subduction Initiation: Part 1. Fore-arc Basalts of the Izu-Bonin Arc From IODP Expedition 352. Geochemistry, Geophysics, Geosystems, 20, 314–338.

Singer, B.S., Costa, F., Herrin, J.S., Hildreth, W., and Fierstein, J. (2016) The timing of compositionally-zoned magma reservoirs and mafic 'priming' weeks before the 1912 Novarupta-Katmai rhyolite eruption. Earth and Planetary Science Letters, 451, 125–137.

Sisson, T.W., and Bronto, S. (1998) Evidence for pressure-release melting beneath magmatic arcs from basalt at Galunggung, Indonesia. Nature, 391, 883–886.

Sparks, S.R.J., Sigurdsson, H., and Wilson, L. (1977) Magma mixing: a mechanism for triggering acid explosive eruptions. Nature, 267, 315–318.

Stern, R.J., and Bloomer, S.H. (1992) Subduction zone infancy: Examples from the Eocene Izu-Bonin-Mariana and Jurassic California arcs. GSA Bulletin, 104, 1621–1636.

Streck, M.J. (2008) Mineral Textures and Zoning as Evidence for Open System Processes. Reviews in Mineralogy and Geochemistry, 69, 595–622.

Taylor, R.N., Nesbitt, R.W., Vidal, P., Harmon, R.S., Auvray, B., and Croudace, I.W. (1994) Mineralogy, Chemistry, and Genesis of the Boninite Series Volcanics, Chichijima, Bonin Islands, Japan. Journal of Petrology, 35, 577–617.

Ubide, T., and Kamber, B.S. (2018) Volcanic crystals as time capsules of eruption history. Nature Communications, 9, 326.

Ubide, T., Mollo, S., Zhao, J., Nazzari, M., and Scarlato, P. (2019) Sector-zoned clinopyroxene as a recorder of magma history, eruption triggers, and ascent rates. Geochimica et Cosmochimica Acta, 251, 265–283.

Umino, S. (1986) Magma mixing in boninite sequence of Chichijima, Bonin Islands. Journal of Volcanology and Geothermal Research, 29, 125–157.

Van Malderen, S. (2017) Optimization of methods based on laser ablation-ICP-mass spectrometry (LA-ICP-MS) for 2-D and 3-D elemental mapping. PhD Thesis, Ghent University.

Van Malderen, S.J., Van Acker, T., and Vanhaecke, F. (2020) Sub-micrometer Nanosecond LA-ICP-MS Imaging at Pixel Acquisition Rates above 250 Hz via a Low-Dispersion Setup. Analytical Chemistry, 92, 5756–5764.

Waters, L.E., and Lange, R.A. (2017) An experimental study of (Fe-Mg) KD between orthopyroxene and rhyolite: a strong dependence on H2O in the melt. Contributions to Mineralogy and Petrology, 172, 42.

Whattam, S.A., Shervais, J.W., Reagan, M.K., Coulthard JR, D.A., Pearce, J.A., Jones, P., Seo, J., Putirka, K., Chapman, T., Heaton, D., and others (2020) Mineral compositions and thermobarometry of basalts and boninites recovered during IODP Expedition 352 to the Bonin forearc. American Mineralogist.

Wyman, D.A. (1999) Paleoproterozoic boninites in an ophiolite-like setting, Trans-Hudson orogen, Canada. Geology, 27, 455–458.

CHAPTER III

3. THE EVOLUTION OF BONINITE MELTS FROM THE IBM FORE-ARC: EVIDENCE FOR CRUSTAL MAGMA RESERVOIRS

ABSTRACT

Boninite lavas recovered during IODP Expedition 352 contain interstitial glass and mineral hosted melt inclusions, which provide a unique perspective on boninite crystal fractionation and the magmatic architecture present during boninite volcanism. Electron Probe Microanalyzer (EPMA) major element analysis of interstitial glass and melt inclusions reveal a chemical trend that ranges in composition from boninite to andesite and dacite. Fourier Transform Infrared Spectrometry (FTIR) analysis on vesiculated produce H_2O concentrations of ~1.5 wt%, interpreted as the minimum melt concentration since H_2O was clearly lost during eruption. Forward and reverse fractional crystallization modeling indicates that boninite crystallization occurred at pressures between 1-3 kb and temperatures between 1000-1300 °C. Olivine-spinel, olivine-liquid, and two-pyroxene thermometry and barometry produce temperatures between 1000-1200 °C and pressures between 1-3 kb. Chemical evolution pathways generated by crystallization models reveal separate trends for LSB and HSB lavas, supporting the hypothesis that LSB volcanism occurs at axial spreading centers while HSB volcanism occurs off-axis (Reagan et al. 2015, 2017, 2019; Shervais et al. submitted). We conclude that LSB lavas erupt from a system similar to those observed a mid-ocean ridge spreading centers while HSB lavas erupt from non-localized off-axis melt lenses.

3.1. Introduction

Boninites are mafic to intermediate volcanic rocks with high concentrations of Mg (>8 wt%) and low concentrations of HFE and other incompatible elements (Bloomer and Hawkins 1987; Taylor et al. 1994; Reagan et al. 2015, 2017; Pearce and Reagan 2019). Although boninite-like rocks have been connected to multiple tectonic settings throughout geologic history, post-Archean boninites are thought to specifically be related to subduction settings (Pearce and Reagan 2019). These boninite magmas form during fluid-fluxed melting of a depleted mantle source, resulting in there magnesian and silica-rich compositions (Cameron et al. 1979, 1983; Hickey and Frey 1982; Cameron 1985; Kyser et al. 1986; Pearce et al. 1992; Taylor et al. 1994; Page et al. 2008, 2009). While boninites are commonly found in ophiolites such as Troodos (Cyprus), Samail (Oman), Thetford Mines (Canada), Betts Cove (Canada), and Koh (New Caledonia) (Cameron 1985; Kyser et al. 1986; Meffre et al. 1996; Bedard et al. 1998; Wyman 1999; Ishikawa et al. 2002, 2005; Page et al. 2008, 2009), they can also be found in western Pacific arc systems such as the IBM (Izu-Bonin Mariana) system and Tonga-Kermadec arc system (Dietrich et al. 1978; Bloomer et al. 1979; Meijer 1980, 1982; Meijer et al. 1982; Crawford 1989; Arculus et al. 1992; Dobson et al. 2006; Meffre et al. 2012).

Evidence of magma mixing from past studies of boninite volcanism indicates that boninite melts enter a system in which primitive and evolved melts are interacting (Umino 1986; Bloomer and Hawkins 1987; Reagan et al. 2015, 2017; Scholpp et al. in review). However, it is currently unclear what the magmatic system during boninite volcanism looks like and at what depths the magma chamber (or site of magmatic

interactions) is located. It is also unclear how this magmatic system is evolving as the locus of magmatism shifts from on axial magmatism from a spreading center to off-axis magmatism as the system transition to a proto-arc (Reagan et al. 2015, 2017, 2019; Shervais et al. submitted).

We use a variety of tools to constrain the depth and temperatures of the magmatic system present during boninite volcanism and how this system changes as the locus of magmatism changes. These include forward modeling of primitive glass compositions, and reverse fractionation modeling of evolved interstitial glass and melt inclusions, to constrain the fractionation pathways and depth of the magmatic system during boninite magmatism, mineral exchange equilibria to constrain magmatic temperatures, and FTIR to constrain water content of the melts. Our goal is to constrain the depth and temperatures of the magmatic system present during boninite volcanism and how this system changes (architecturally and chemically) as the locus of magmatism changes.

3.1.1.Geologic Setting

International Oceanic Discovery Program (IODP) Expedition 352 targeted the southern Izu-Bonin fore-arc, east of the Bonin Islands, and close to the active trench (Reagan et al. 2015). The primary objectives of IODP Expedition 352 were to obtain a high-fidelity record of magmatic evolution during subduction and early arc development, understand the chemical evolution of magmas during subduction initiation and test the hypothesis that fore-arc created during subduction initiation is the birthplace of supra subduction zone ophiolites (Reagan et al. 2015). Reagan et al. (2015, 2017, 2019) contend that subduction initiation is associated with voluminous melting and production

of fore-arc basalts (FAB), erupting from a persistent magma chamber much like mid-ocean ridge basalts (MORB). The boninite sequence begins with the eruption of Low-Si Boninite (LSB), likely erupting from the magma chambers, like FAB. The eruptive sequence is said to transition to off-axis magmatism as the subduction system continues to evolve, and fore-arc spreading shuts down. The eruption of High-Si Bonininte (HSB) begins as spreading decreases. HSB magmatism eventually transitions to focused proto-arc volcanism, resulting in an embryonic volcanic arc.

3.2. Samples and Methods

Samples in this study came from Holes U1439C, and U1442A drilled during IODP Expedition 352, both of which sampled thick sections of boninite volcanics. Samples from Hole U1439C were the primary focus of this study; however, three samples from Hole U1442A were analyzed to determine the water content in boninite lavas, due to their glass rich and crystal poor compositions. Samples from hole U1439C were analyzed using an electron probe micro-analyzer (EPMA) to determine the major element compositions of the minerals, interstitial glass, and melt inclusion glass.

3.2.1.EPMA Methods

Mineral, interstitial glass, and melt inclusion chemistry was analyzed using the JEOL 8900R Superprobe EPMA system of the Florida Center for Analytical Electron Microscopy (FCAEM) at Florida International University and the Cameca SXfive of the Center for Material Characterization at Boise State University. For quantitative WDS mineral analyses, operating conditions were a 15kV accelerating voltage and a 20 nA

beam current, with a spot size of 1-2 μm (for mineral analysis) and 10-20 μm (for glass analysis) on the JEOL 8900R Superprobe and 5-10 μm on the Cameca SXfive. The elements Si, Al, Fe, Mg, Ca, Mn, Na, K, Ti, and Cr, were routinely measured on all samples and on both instruments. For the JEOL 8900R Superprobe, a selection of mineral standards from SPI, Inc., and Micro-Analysis Consultants, Ltd. were used to calibrate WDS measurements (fayalite, olivine, Cr-diopside, An65 plagioclase, kaersutite, augite, enstatite, and chromite: see Table A.1. for compositions). Typically, a mixed suite of standards (sometimes including the USGS BHVO-1 basaltic glass standard) were used to conduct initial characterizations, followed by re-calculation or re-analysis using a smaller set of compositionally matched standards after minerals were identified. For the Cameca SXfive a selection of synthetic mineral standards, as well as, natural mineral and glass standards from the Smithsonian Institute and SPI, Inc. were used to calibrate WDS measurements of unknowns (San Carlos Olivine, Chromite, Anorthite, Diopside, Syn Tephroite, Syn Fayalite, Syn Rutile, Amelia Albite, and Basaltic Glass VG-2: see Table A.1. for compositions). EPMA measurements were used to confirm microscope-based phase identifications, to identify important minor phases (Cr-rich spinels, rare ilmenites, and apatites), and to characterize the mineral zoning and overgrowth textures that were encountered in some of the samples.

3.2.2. FTIR Methods

Glassy samples were extracted from several Expedition 352 boninite samples. As all the samples were highly phyric, even the most glassy samples included some olivine and pyroxene crystals, with no preferred orientations evident. Each sample was coarsely

crushed in an alumina crucible with a sapphire mortar to obtain 1-2 mm pieces. The glassy chips were then secured to a mounting disc with Crystalbond 509 epoxy (SPI Supplies), where they were sanded flat to ~200 μm thickness as measured by caliper. Samples were then polished in progressively finer and finer media, turned over, and the process was repeated on the other side to attain wafers with thicknesses of ≤150μm ≥90μm. Final polishing was completed using 1.0 μm and 0.3 μm alumina polishing powder suspended in 18 MΩ deionized water. The wafers were then cleaned with acetone and rinsed with DI before measurement. FTIR measurements were made at the University of South Florida, using a Bruker IFS 66 FTIR system in transmission mode using a Globar IR source and KBr beam splitter. Absorbance spectra were obtained from 1024 sweeps, and data was reduced following the methods of Ihinger et al. (1994) and Dixon et al. (1995). Spectra were obtained at thickness measurement points for several areas not obstructed by crystals and averaged to determine the H2O wt.% at 3530 cm-1 and 1630 cm-1, respectively, using calculations derived from Dixon et al. (1995) and Dixon and Clague (2001).

3.2.3.Forward and Reverse Crystallization Modelling

Forward and reverse petrogenetic modeling calculations were conducted using the Petrolog3 software from Danyushevsky and Plechov (2011). The crystallization models of Ariskin et al. (1993) (initially created for modeling with the COMAGMAT software from Ariskin et al. 1993) were used for both forward and reverse models. This model was chosen because it allowed all crystal phases present in the samples to be modeled without having to use multiple crystallization models.

Forward and Reverse modeling are based on thermodynamic models of multiple mineral species. In forward models, primitive (i.e., less chemically evolved) melt compositions are input with an estimated pressure. The Petrolog3 software then determines what mineral species would be in equilibrium with that melt at the given pressure. The model then determines the change in melt composition after the crystallization of a given percentage of that mineral species (in our models this was set to 0.01%). The model software repeats this process multiple times, simulating crystallization of a melt. Reverse modelling follows a similar procedure; however, in reverse models an evolved composition is input with an estimated pressure. The mineral species and chemical composition observed in the sample is also added to a reverse model. The model determines the equilibrium melt and mineral composition based on all of the input parameters provided. The software then adds a given percentage (this was again set to 0.01% for our models) of the equilibrium mineral back into the melt and calculates its effect on the melt composition. This process is repeated, effectively recreating the primitive melt composition and providing a chemical evolution path.

3.2.4.Thermometry and Barometry

Olivine-spinel geothermometry calculations from Balhaus et al. (1990) and Jiangping et al. (1995) were used to determine mineral equilibrium temperatures of olivine and spinel pairs. The two-pyroxene geothermometry calculations of Brey and Kohler (1990) and the two-pyroxene thermobarometry Putirka (2008) were used to determine the equilibrium temperatures and pressures of adjacent pyroxene zones (i.e., zones within a pyroxene phenocryst). Olivine-liquid geothermometry from Putirka et al.

(2007) were used to determine the equilibrium temperatures of olivine in the host melt.

3.3. Results

3.3.1. Petrography and Mineral Chemistry

All samples in this study are classified as LSB or HSB per the nomenclature of the Expedition 352 Science Team (Reagan et al. 2017). These samples contain the common boninite phenocryst assemblage low-Ca pyroxene (enstatite ± clinoenstatite) + olivine, with later-formed acicular crystals of low-Ca pyroxene (enstatite and clinoenstatite to pigeonite) and clinopyroxene (augite) in a glassy or crystalline matrix. Olivine grains are typically rounded and embayed, suggesting partial resorption. Some high-silica boninite samples lack olivine, consisting exclusively of low-Ca pyroxene and groundmass clinopyroxene. Olivine compositions range from Fo 87-92, similar to those reported at Chichijima by Umino (1986) and Dobson et al. (2006), while the enstatite and clinoenstatite phenocrysts vary from Mg# 80-88, with <5% CaO, broadly similar to those reported on Chichijima by Umino (1986) (Tables 3.1 & 3.2). The more calcic clinopyroxene compositions in our samples are pigeonite (Mg# 75-65) and augite (Mg# 70-30).

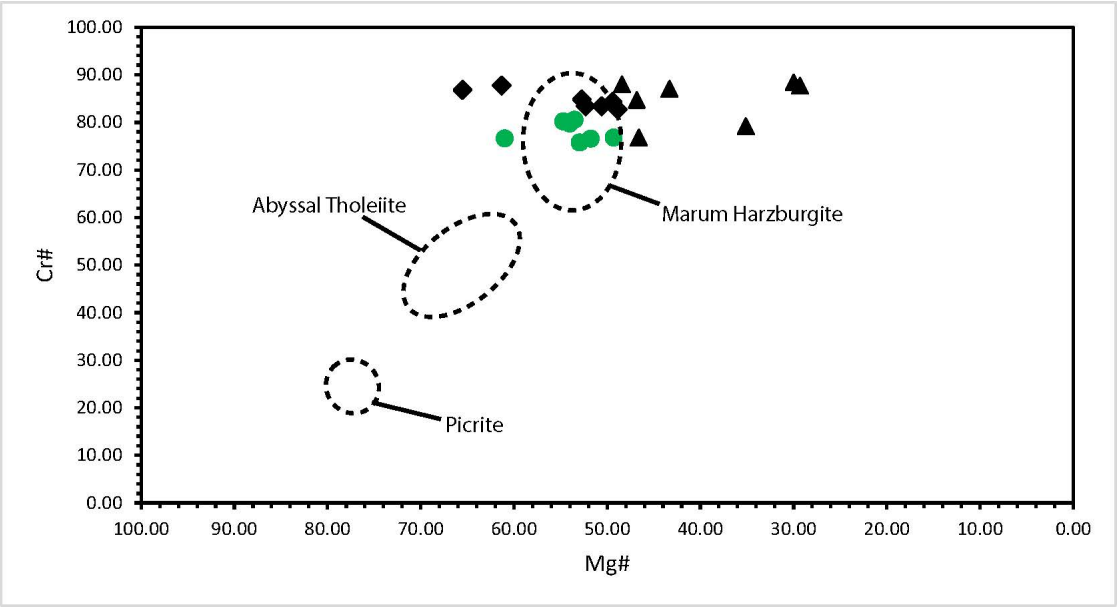

Figure 3.1
Compositional variation of Cr-spinel in boninites in terms of Cr/(Cr+Al) vs. Mg/(Mg+Fe2+) (i.e., Cr# vs. Mg#). Figure modified after Umino (1986). Green circles represent data from this study. Black triangles represent data from Umino (1986). Black triangles represent data from Dobson et al. (2006). Spinels from abyssal tholeiites and picrites (Dick et al. 1979) and Marum Harzburgite (Jacques 1981) are plotted for comparison.

Table 3.1. Olivine Compositions and Ol-liquid Temperatures

Sample	Mineral	SiO2 (wt%)	TiO2 (wt%)	Al2O3 (wt%)	Cr2O3 (wt%)	FeO (wt%)	MgO (wt%)	MnO (wt%)	NiO (wt%)	CaO (wt%)	Na2O (wt%)	K2O (wt%)	Total (wt%)	Fo	2% H_2O T(°C)	5% H_2O T(°C)
25R2	Ol	42.13	0.01	0.02	0.10	7.67	49.37	0.13	0.00	0.11	0.01	0.01	99.55	91.98	1250.47	1185.89
25R2	Ol	42.21	0.01	0.03	0.09	8.29	48.89	0.12	0.00	0.13	0.01	0.00	99.78	91.32	1228.47	1166.09
25R2	Ol	41.77	0.00	0.01	0.14	11.08	46.39	0.18	0.00	0.17	0.02	0.01	99.76	88.18	1132.77	1079.52
15R1	Ol	40.99	0.00	0.05	0.14	11.60	47.85	0.04	0.00	0.16	0.01	0.01	100.86	88.03	1125.77	1073.16
15R1	Ol	42.37	0.00	0.02	0.06	10.52	48.30	0.16	0.28	0.13	0.00	0.00	101.83	89.11	1156.62	1101.16
15R1	Ol	42.37	0.00	0.02	0.06	10.52	48.30	0.16	0.28	0.13	0.00	0.00	101.83	89.11	1158.18	1102.57
19R2	Ol	41.98	0.00	0.01	0.06	10.44	48.19	0.22	0.17	0.16	0.00	0.00	101.22	89.16	1172.09	1115.17
19R2	Ol	42.14	0.02	0.03	0.05	9.87	49.22	0.19	0.23	0.13	0.00	0.00	101.89	89.89	1190.86	1132.16
2R3	Ol	42.25	0.00	0.02	0.12	10.94	48.01	0.20	0.28	0.12	0.02	0.01	101.96	88.66	1162.23	1107.59
2R3	Ol	42.17	0.00	0.03	0.08	11.65	47.07	0.21	0.25	0.15	0.00	0.02	101.62	87.81	1118.97	1066.98
														Avg.	1169.64	1113.03
														Stdev.	40.81	36.89

[a] Minerals: Olivine (Ol).

[b] Mineral end-members: Forsterite (Fo).

[c] Samples: U1439C-25R-2-W 18-19 (25R2).

[d] The 2% H_2O T(°C) and 5% H_2O T(°C) columns show temperatures determined using calculations from Putirka et al. (2007).

Table 3.2. Pyroxene Compositions and P-T results

Sample	SiO2 (wt%)	TiO2 (wt%)	Al2O3 (wt%)	Cr2O3 (wt%)	FeO (wt%)	MgO (wt%)	MnO (wt%)	NiO (wt%)	CaO (wt%)	Na2O (wt%)	K2O (wt%)	Total (wt%)	Jd	CaTiTs	CaCrTs	CaTs	Wo	En	Fs	Mg#		B & K (1990) T(°C)	Putirka (2008) T(°C)	Putirka (2008) P(kb)
25R2	56.51	0.11	1.01	0.28	9.70	30.25	0.10	0.04	2.18	0.05	0.00	100.23	0.18	0.15	0.40	0.63	3.22	80.88	14.54	75.73				
25R2	52.21	0.53	4.11	0.17	7.95	17.69	0.10	0.01	16.19	0.21	0.03	99.19	0.79	0.79	0.26	3.48	29.29	52.22	13.17	68.98		1220.18	1171.17	5.15
25R2	56.57	0.00	1.27	0.51	9.60	29.99	0.12	0.04	2.88	0.04	0.00	101.02	0.14	0.00	0.71	0.91	4.44	79.53	14.27	75.76				
25R2	50.17	0.35	5.88	0.05	8.24	14.70	0.10	0.01	19.66	0.24	0.00	99.39	0.92	0.52	0.07	5.93	34.84	43.91	13.81	64.08		1110.98	1121.52	0.94
15R1	57.15	0.00	0.97	0.50	7.82	32.52	0.06	0.00	1.22	0.03	0.00	100.27	0.09	0.00	0.70	0.61	1.61	85.46	11.53	80.61				
15R1	49.94	0.53	6.11	0.00	10.36	14.64	0.08	0.00	19.09	0.17	0.00	100.93	0.66	0.78	0.00	5.96	32.74	42.85	17.00	58.57		1166.20	1115.81	3.28
15R1	56.51	0.00	1.08	0.56	8.29	32.09	0.07	0.00	1.47	0.00	0.02	100.08	0.00	0.00	0.78	0.73	2.04	84.24	12.21	79.47				
15R1	50.46	0.21	5.50	0.00	8.82	15.07	0.09	0.00	19.08	0.17	0.01	99.40	0.64	0.31	0.00	5.82	33.88	44.68	14.67	63.08		1150.02	1094.32	3.67
15R1	55.93	0.06	0.75	0.55	6.90	36.32	0.18	0.00	1.23	0.01	0.01	101.93	0.03	0.08	0.70	0.27	1.75	87.80	9.36	84.03				
15R1	48.06	0.44	6.06	0.00	10.16	15.42	0.27	0.00	20.30	0.17	0.00	100.88	0.63	0.63	0.00	5.77	33.83	43.19	15.96	60.28		1116.77	1120.41	5.15
15R1	56.80	0.06	1.07	0.56	7.05	31.16	0.09	0.09	1.73	0.09	0.01	98.69	0.30	0.09	0.81	0.51	2.50	85.01	10.78	81.56				
15R1	50.11	0.26	5.49	0.00	9.82	14.85	0.28	0.04	17.93	0.17	0.01	98.96	0.65	0.40	0.00	5.81	31.91	44.65	16.57	60.19		1212.18	1153.76	4.93
15R1	56.94	0.01	0.74	0.35	7.44	31.55	0.16	0.08	1.47	0.02	0.00	98.76	0.05	0.02	0.50	0.49	2.30	85.34	11.29	80.91				
15R1	49.57	0.17	6.32	0.02	8.92	13.94	0.18	0.01	19.71	0.17	0.00	99.00	0.67	0.25	0.03	6.94	34.92	42.09	15.11	60.98		1122.82	1067.35	3.20
15R1	56.72	0.05	1.11	0.57	7.87	31.03	0.10	0.08	1.65	0.04	0.01	99.23	0.15	0.07	0.81	0.64	2.36	84.02	11.95	79.77				
15R1	51.03	0.16	4.19	0.04	8.23	15.61	0.20	0.02	18.80	0.18	0.01	98.45	0.68	0.23	0.07	4.29	34.82	46.23	13.67	65.49		1159.46	1107.56	4.76
15R1	58.47	0.05	0.92	0.31	8.47	31.62	0.17	0.10	1.84	0.00	0.01	101.94	0.00	0.07	0.43	0.67	2.75	83.53	12.55	78.87				
15R1	47.81	0.56	9.01	0.06	12.81	11.39	0.26	0.00	19.97	0.01	0.01	101.89	0.06	0.86	0.10	9.86	32.75	34.56	21.80	47.07		1120.88	1054.60	0.20
2R3	57.9	0.1	1.8	0.6	8.5	30.1	0.2	0.1	2.5	0.0	0.0	101.8	0.0	0.1	0.9	1.4	3.4	81.3	12.9	78.0				
2R3	51.3	0.3	5.5	0.0	9.5	14.5	0.2	0.0	19.5	0.0	0.0	100.9	0.0	0.5	0.1	5.9	35.1	42.8	15.7	60.5		1150.22	1096.52	0.66
																				Avg.		1152.97	1110.30	3.19
																				Stdev.		36.43	33.54	1.84

[a] Samples: U1439C-25R-2-W 18-19 (25R2), U1439C-15R-1-W 8-10 (15R1), U1439C-2R-3-W 2-3 (2R3).

[b] Pyroxene Quadrilateral Components: Enstatite (En), Wollastonite (Wo), Ferrosilite (Fs).

[c] Pyroxene Non-Quadrilateral Components: Jadeite (Jd), Ti-Tschermak (CaTiTs), Cr-Tschermak (CaCrTs), Ca-Tschermak (CaTs).

[d] Mg#=100*(Mg/(Mg+Fe)).

[e] The B& K T(°C) column shows temperatures determined using calculations from Brey and Kohler (1990), the Putirka (2008) T(°C) and Putirka (2008) P(kb)columns show temperatures and pressures determined using calculations from Putirka (2008).

Table 3.3. Composition of Olivine-Spinel Pairs and P-T Results

Sample	Mineral	SiO2 (wt%)	TiO2 (wt%)	Al2O3 (wt%)	Cr2O3 (wt%)	FeO (wt%)	MgO (wt%)	MnO (wt%)	NiO (wt%)	CaO (wt%)	Na2O (wt%)	K2O (wt%)	Total (wt%)	Mg#	Cr#		Ballhaus T(°C)	Jianping T(°C)
15R1	Ol	40.99	0.00	0.05	0.14	11.60	47.85	0.04	0.00	0.16	0.01	0.01	100.86	88.02	66.81		1067.34	1168.52
15R1	Cr-Sp	1.88	0.08	8.20	59.29	19.49	11.76	0.24	0.00	0.11	0.16	0.08	101.29	51.81	82.91			
15R1	Ol	42.37	0.00	0.02	0.06	10.52	48.30	0.16	0.28	0.13	0.00	0.00	101.83	89.11	64.27		956.88	1072.19
15R1	Cr-Sp	0.05	0.16	10.34	58.42	20.16	10.97	0.35	0.14	0.01	0.00	0.00	100.61	49.22	79.12			
15R1	Ol	42.37	0.00	0.02	0.06	10.52	48.30	0.16	0.28	0.13	0.00	0.00	101.83	89.11	64.27		1028.15	1132.49
15R1	Cr-Sp	0.11	0.10	7.35	60.99	21.38	11.37	0.32	0.10	0.06	0.02	0.00	101.79	48.67	84.78			
19R2	Ol	41.98	0.00	0.01	0.06	10.44	48.19	0.22	0.17	0.16	0.00	0.00	101.22	89.16	77.32		908.40	1026.20
19R2	Cr-Sp	0.05	0.16	9.36	58.31	21.69	10.09	0.42	0.11	0.02	0.00	0.01	100.20	45.33	80.70			
19R2	Ol	42.14	0.02	0.03	0.05	9.87	49.22	0.19	0.23	0.13	0.00	0.00	101.89	89.89	52.95		1100.06	1198.04
19R2	Cr-Sp	0.05	0.19	9.24	59.60	18.76	13.08	0.30	0.09	0.03	0.00	0.00	101.32	55.41	81.22			
2R3	Ol	42.25	0.00	0.02	0.12	10.94	48.01	0.20	0.28	0.12	0.02	0.01	101.96	88.66	78.60		1013.15	1122.87
2R3	Cr-Sp	0.08	0.10	8.48	62.61	19.31	11.07	0.37	0.10	0.02	0.01	0.00	102.16	50.54	83.21			
2R3	Ol	42.17	0.00	0.03	0.08	11.65	47.07	0.21	0.25	0.15	0.00	0.02	101.62	87.81	61.44		999.66	1109.07
2R3	Cr-Sp	0.02	0.12	10.07	59.20	20.43	10.66	0.29	0.12	0.03	0.04	0.00	100.98	48.19	79.77			
																Avg.	1010.52	1118.48
																Stdev.	59.75	53.18

[a] Minerals: Ol= Olivine, Cr-Sp= Cr-Spinel.

[b] Samples: U1439C-15R-1-W 8-10 (15R1), U1439C-19R-2-W 46-48 (19R2), U1439C-2R-3-W 2-3 (2R3).

[c] The Ballhaus T(°C) column shows temperatures determined using calculations from Ballhaus et al. (1990), the Jianping T(°C) column shows temperatures determined using calculations from Jianpin et al. (1995).

[d] Mg#=100*(Mg/(Mg+Fe)), Cr#= 100* (Cr/(Cr+Al))

Chromium-rich spinel is a common minor mineral phase, as small isolated grains within the groundmass glass, and enclosed within larger olivine and (rarely) enstatite/clinoenstatite crystals (but never within pigeonite grains). Cr-spinel inclusions are typically in the cores of olivine, pointing to early crystallization (Table 3.3). Cr-spinel has concentrations of Al_2O_3 (≈7-10 wt%), MgO (≈9-14 wt%), FeO^{tot} (≈16-24 wt%), and TiO_2 (≈0.04-0.20 wt%) similar to the Cr-spinels reported in Umino (1986) and Dobson et al. (2006) from Chichijima with slight differences in Al_2O_3 and MgO concentrations (Figure 3.1).

3.3.2.Interstitial Glass and Melt Inclusion Compositions

Interstitial glass is commonly found in boninite pillow lavas from Expedition 352 (i.e., like the samples from this study). Andesite and dacite compositions were the most common compositions found in the samples from this study (Figure 3.2, Table 3.4). High-Mg andesite, LSB, and HSB glass compositions were also observed in some samples; however, these compositions are far less common. LSB and HSB compositions are most common in interstitial glass and melt inclusions, which are have undergone less crystallization (i.e., samples which are less crystal-rich or melt inclusions which lack evidence of crystallization after entrapment).

Table 3.4. Glass Analysis

SAMPLE	Glass Type	Analy. Ins.	SiO2 (wt%)	TiO2 (wt%)	Al2O3 (wt%)	Cr2O3 (wt%)	FeO (wt%)	MgO (wt%)	MnO (wt%)	CaO (wt%)	Na2O (wt%)	K2O (wt%)	P2O5 (wt%)	Total (wt%)	Si8	Ti8
2R3	FG	Cameca	61.45	0.18	19.86	0.02	2.93	0.33	0.05	5.62	2.87	0.93	0.00	94.24	59.44	0.15
2R3	FG	Cameca	62.74	0.11	19.18	0.01	3.14	0.43	0.05	5.66	2.86	0.93	0.00	95.11	60.75	0.10
2R3	FG	Cameca	62.25	0.18	18.83	0.01	4.56	0.82	0.05	5.64	2.62	0.83	0.00	95.79	60.37	0.15
2R3	FG	Cameca	61.25	0.19	18.48	0.00	4.65	0.87	0.06	5.70	2.39	0.85	0.00	94.44	59.38	0.17
2R3	FG	Cameca	62.15	0.12	18.54	0.00	4.15	0.71	0.06	6.49	2.64	0.86	0.00	95.74	60.24	0.10
2R3	FG	Cameca	58.69	0.28	18.74	0.01	5.10	1.45	0.07	8.25	2.45	0.77	0.00	95.80	56.98	0.24
2R3	FG	JEOL	60.59	0.18	19.15	0.00	4.13	0.63	0.04	5.67	3.04	0.73	0.03	94.18	58.66	0.15
2R3	FG	JEOL	61.22	0.21	18.69	0.00	4.46	0.58	0.07	5.92	3.36	0.83	0.01	95.33	59.28	0.18
2R3	FG	JEOL	61.39	0.18	19.19	0.00	2.51	0.59	0.07	5.71	2.44	0.65	0.03	92.76	59.45	0.15
2R3	FG	JEOL	61.92	0.19	18.24	0.00	2.01	0.42	0.08	5.71	3.04	0.84	0.02	92.47	59.94	0.16
2R3	FG	JEOL	60.66	0.21	19.04	0.00	2.87	0.83	0.08	5.64	3.08	0.81	0.02	93.23	58.79	0.18
2R3	FG	JEOL	60.85	0.14	18.85	0.00	2.31	0.56	0.07	5.85	3.28	0.81	0.03	92.74	58.90	0.11
2R3	FG	JEOL	61.37	0.18	19.25	0.00	2.75	0.64	0.06	5.11	3.05	0.78	0.01	93.20	59.44	0.15
2R3	MI	Cameca	63.49	0.16	19.21	0.01	2.81	0.19	0.05	5.93	2.57	0.83	0.00	95.25	61.44	0.13
2R3	MI	Cameca	64.15	0.20	20.08	0.00	2.54	0.15	0.04	6.37	2.99	0.87	0.00	97.39	62.09	0.16
5R1	FG	JEOL	63.50	0.22	16.42	0.00	3.44	1.48	0.08	5.75	2.81	0.84	0.02	94.57	61.80	0.19
5R1	FG	JEOL	63.49	0.33	16.61	0.00	3.32	1.34	0.07	5.79	2.87	0.83	0.04	94.68	61.74	0.28
5R1	FG	JEOL	63.38	0.21	16.34	0.00	3.14	1.19	0.09	5.41	2.91	0.88	0.03	93.58	61.60	0.18
5R1	FG	JEOL	62.54	0.21	16.72	0.00	2.84	1.25	0.06	5.26	2.84	0.83	0.02	92.56	60.77	0.18
5R1	FG	JEOL	63.36	0.24	16.13	0.00	3.08	1.26	0.09	5.37	2.89	0.89	0.02	93.32	61.59	0.21
8R1	FG	JEOL	58.62	0.25	13.11	0.00	4.18	5.85	0.14	8.09	2.07	0.59	0.00	92.91	58.06	0.24
8R1	FG	JEOL	58.88	0.16	12.73	0.00	3.81	5.98	0.14	7.88	2.14	0.59	0.00	92.32	58.35	0.15
8R1	FG	JEOL	57.57	0.23	12.92	0.00	3.92	5.76	0.11	7.98	2.01	0.60	0.04	91.15	56.98	0.22
8R1	FG	JEOL	60.37	0.23	12.98	0.00	4.21	6.16	0.14	7.84	2.14	0.57	0.01	94.65	59.88	0.22
8R1	FG	JEOL	58.86	0.21	12.90	0.00	4.24	5.75	0.13	8.20	2.05	0.62	0.02	92.98	58.27	0.20
15R1	FG	Cameca	62.72	0.17	18.97	0.00	3.44	0.46	0.07	5.46	2.71	0.90	0.00	94.90	60.74	0.15
15R1	FG	Cameca	60.08	0.22	18.36	0.00	4.30	0.94	0.07	4.96	2.95	1.11	0.00	92.99	58.23	0.19
15R1	FG	Cameca	62.78	0.16	18.72	0.00	3.86	0.61	0.08	5.56	2.69	0.88	0.00	95.33	60.84	0.14
15R1	FG	Cameca	63.32	0.10	18.89	0.00	3.25	0.46	0.05	5.54	2.73	0.89	0.00	95.24	61.35	0.08
15R1	FG	Cameca	61.10	0.15	18.57	0.01	3.96	0.67	0.06	5.74	2.55	0.85	0.00	93.65	59.18	0.13

SAMPLE	Glass Type	Analy. Ins.	SiO2 (wt%)	TiO2 (wt%)	Al2O3 (wt%)	Cr2O3 (wt%)	FeO (wt%)	MgO (wt%)	MnO (wt%)	CaO (wt%)	Na2O (wt%)	K2O (wt%)	P2O5 (wt%)	Total (wt%)	Si8	Ti8
15R1	FG	Cameca	59.51	0.19	18.10	0.00	3.44	0.45	0.07	5.47	2.29	1.14	0.00	90.66	57.54	0.16
15R1	FG	Cameca	62.86	0.15	19.07	0.00	3.31	0.33	0.06	5.69	2.68	0.89	0.00	95.03	60.85	0.13
15R1	FG	Cameca	60.92	0.22	18.85	0.00	3.30	0.29	0.06	6.01	2.16	0.77	0.00	92.59	58.90	0.18
15R1	FG	Cameca	62.01	0.15	19.67	0.00	3.03	0.27	0.06	5.67	3.03	1.00	0.00	94.86	59.99	0.12
15R1	FG	JEOL	61.22	0.16	19.27	0.00	4.21	0.67	0.10	6.01	3.24	0.79	0.02	95.69	59.30	0.13
15R1	FG	JEOL	60.59	0.21	18.94	0.00	4.93	0.81	0.05	5.97	3.13	0.78	0.02	95.42	58.70	0.18
15R1	FG	JEOL	60.07	0.21	19.11	0.00	5.88	1.22	0.09	6.61	2.73	0.68	0.02	96.62	58.29	0.18
15R1	FG	JEOL	61.21	0.13	19.49	0.00	3.34	0.29	0.06	5.74	3.58	0.79	0.01	94.64	59.19	0.11
15R1	FG	JEOL	60.38	0.19	19.04	0.00	5.59	1.12	0.07	6.05	2.80	0.63	0.03	95.89	58.58	0.16
15R1	FG	JEOL	60.55	0.20	19.06	0.00	4.17	0.57	0.07	5.98	3.04	0.67	0.01	94.31	58.60	0.17
15R1	FG	JEOL	60.22	0.22	18.99	0.00	5.47	0.93	0.09	5.63	2.94	0.67	0.02	95.16	58.37	0.19
15R1	MI	Cameca	61.66	0.23	18.70	0.00	4.33	0.60	0.09	5.99	2.31	0.79	0.00	94.70	59.72	0.20
15R1	MI	Cameca	56.80	0.11	11.97	0.15	5.97	9.88	0.12	7.91	1.42	0.62	0.00	94.96	57.29	0.12
15R1	MI	Cameca	62.79	0.22	19.15	0.00	3.39	0.31	0.06	5.98	2.38	0.75	0.00	95.04	60.77	0.19
15R1	MI	Cameca	62.88	0.13	18.90	0.00	3.22	0.36	0.06	5.42	2.78	0.95	0.00	94.70	60.88	0.11
25R2	FG	Cameca	62.06	0.33	17.20	0.02	5.26	1.28	0.12	5.65	2.05	0.38	0.00	94.35	60.31	0.29
25R2	FG	Cameca	62.76	0.37	17.13	0.01	5.01	1.36	0.07	5.35	1.96	0.40	0.00	94.41	61.02	0.32
25R2	FG	Cameca	61.99	0.32	17.67	0.00	5.33	1.49	0.10	5.76	1.22	0.35	0.00	94.25	60.29	0.28
25R2	FG	Cameca	64.83	0.22	18.19	0.00	2.73	0.32	0.05	4.90	1.56	0.37	0.00	93.15	62.82	0.19
25R2	FG	Cameca	64.29	0.29	18.28	0.01	3.51	0.65	0.06	5.00	1.55	0.32	0.00	93.97	62.37	0.24
25R2	FG	Cameca	62.67	0.34	17.87	0.00	4.64	1.32	0.09	5.65	1.75	0.30	0.00	94.64	60.92	0.30
25R2	FG	Cameca	63.18	0.29	18.74	0.01	4.55	1.41	0.08	4.60	2.29	0.40	0.00	95.55	61.46	0.25
25R2	FG	Cameca	63.67	0.39	17.70	0.00	3.78	0.76	0.08	5.77	1.58	0.35	0.00	94.06	61.77	0.33
25R2	FG	Cameca	60.75	0.31	16.80	0.01	5.05	1.45	0.09	5.87	1.29	0.29	0.00	91.92	59.04	0.27

Table 3.4. continues

SAMPLE	Glass Type	Analy. Ins.	SiO2 (wt%)	TiO2 (wt%)	Al2O3 (wt%)	Cr2O3 (wt%)	FeO (wt%)	MgO (wt%)	MnO (wt%)	CaO (wt%)	Na2O (wt%)	K2O (wt%)	P2O5 (wt%)	Total (wt%)	Si8	Ti8
25R2	MI	Cameca	63.16	0.31	17.89	0.00	4.67	1.11	0.10	5.51	1.48	0.28	0.00	94.52	61.36	0.27
25R2	MI	Cameca	64.53	0.19	17.97	0.01	2.63	0.43	0.05	5.41	1.43	0.32	0.00	92.95	62.54	0.16
25R2	MI	Cameca	63.81	0.29	17.37	0.00	3.61	0.89	0.06	5.02	1.29	0.35	0.00	92.70	61.94	0.25
25R2	MI	Cameca	59.69	0.21	18.12	0.00	4.31	1.39	0.08	6.87	1.52	0.38	0.00	92.57	57.96	0.18
25R2	MI	Cameca	64.21	0.38	17.96	0.01	3.80	0.94	0.09	5.11	1.64	0.34	0.00	94.50	62.37	0.33
25R2	MI	Cameca	62.67	0.40	17.18	0.01	4.53	1.18	0.09	6.02	1.46	0.37	0.00	93.91	60.88	0.34
25R2	MI	Cameca	64.63	0.37	17.24	0.01	4.20	0.90	0.05	4.83	1.40	0.31	0.00	93.94	62.77	0.31
25R2	MI	Cameca	64.73	0.34	17.55	0.00	3.64	0.58	0.08	4.83	1.59	0.33	0.00	93.67	62.78	0.29
25R2	MI	Cameca	60.45	0.27	16.43	0.00	6.05	2.30	0.15	7.46	1.43	0.28	0.00	94.81	58.96	0.24
25R2	MI	Cameca	61.81	0.40	17.13	0.03	3.98	1.02	0.09	6.14	1.64	0.37	0.00	92.59	59.98	0.34
25R2	MI	Cameca	63.28	0.35	17.85	0.01	4.73	1.12	0.10	5.58	1.56	0.36	0.00	94.93	61.48	0.31
25R2	MI	Cameca	62.35	0.32	17.00	0.01	4.63	1.39	0.09	5.55	1.56	0.38	0.00	93.28	60.62	0.27
25R2	MI	Cameca	62.66	0.21	17.48	0.00	3.36	0.69	0.05	5.03	1.45	0.36	0.00	91.29	60.75	0.18
25R2	MI	Cameca	64.10	0.29	17.96	0.00	3.59	0.59	0.07	4.88	1.46	0.32	0.00	93.25	62.16	0.24
29R1	FG	JEOL	53.03	0.19	11.91	0.00	9.71	14.76	0.16	3.89	1.00	0.56	0.01	95.22	54.80	0.23
29R1	FG	JEOL	54.45	0.18	12.64	0.00	6.92	12.12	0.06	2.58	0.70	0.89	0.00	90.54	55.53	0.20
29R1	FG	JEOL	54.02	0.26	11.29	0.00	8.15	13.49	0.08	3.26	1.20	1.50	0.00	93.26	55.46	0.30
31R2	FG	Cameca	61.30	0.20	19.28	0.01	3.80	0.83	0.07	6.15	2.80	0.51	0.00	94.95	59.42	0.17
31R2	MI	Cameca	57.30	0.19	15.22	0.00	4.55	8.47	0.10	4.13	1.84	0.67	0.00	92.46	57.42	0.19
31R2	MI	Cameca	64.32	0.32	17.43	0.02	3.16	0.45	0.06	5.91	2.33	0.47	0.00	94.47	62.34	0.27

[a] Glass type: Fresh Interstitial Glass (FG), Melt Inclusion (MI)

[b] Samples: U1439C-15R-1-W 8-10 (15R1), U1439C-25R-2-W 18-19 (19R2), U1439C-2R-3-W 2-3 (2R3), (29R1), (5R1), (8R1), (31R2).

[c] The Analy. Ins. column indicates the analytical instrument used

[d] Si8= SiO_2+(MgO-8)/3.32 , Ti8= 42*TiO_2/(50-MgO)

Table 3.4. continues

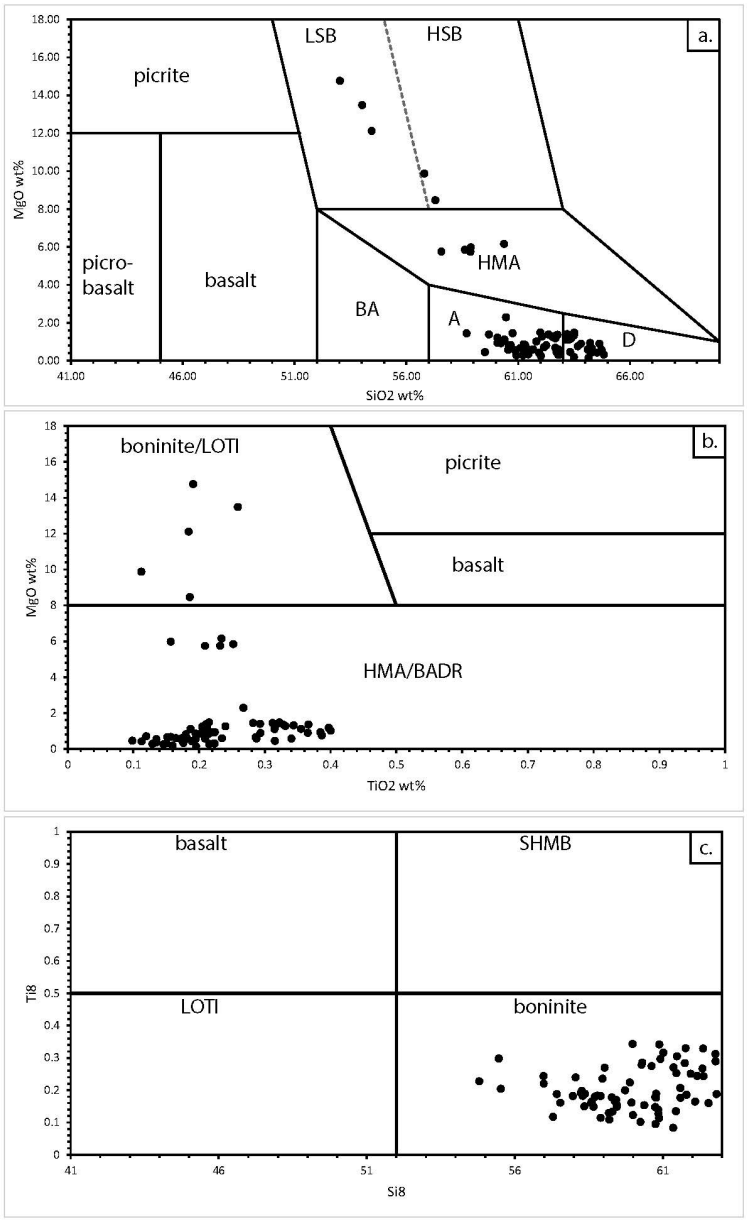

Figure 3.2
Glass analysis from this study plotted on the classification diagrams develop by Pearce and Reagan (2019) for boninites. (a.) modified version of the MgSi plot commonly used to define boninite melts, (b.) MgTi plot showing boninite classification zone, (c.) new classification diagram developed by Pearce and Reagan (2019) which plots Ti8 (i.e., Ti against Mg) and Si8 (i.e., Si against Mg). Low-Si Boninite (LSB), High-Si Boninite (HSB), High-Mg Andesite (HMA), Basaltic Andesite (BA), Andesite (A), Dacite (D), Low-Ti Basalts (LOTI), Basalt-Andesite-Dacite-Rhyolite (BADR), Siliceous High-Mg Basalts (SHMB).

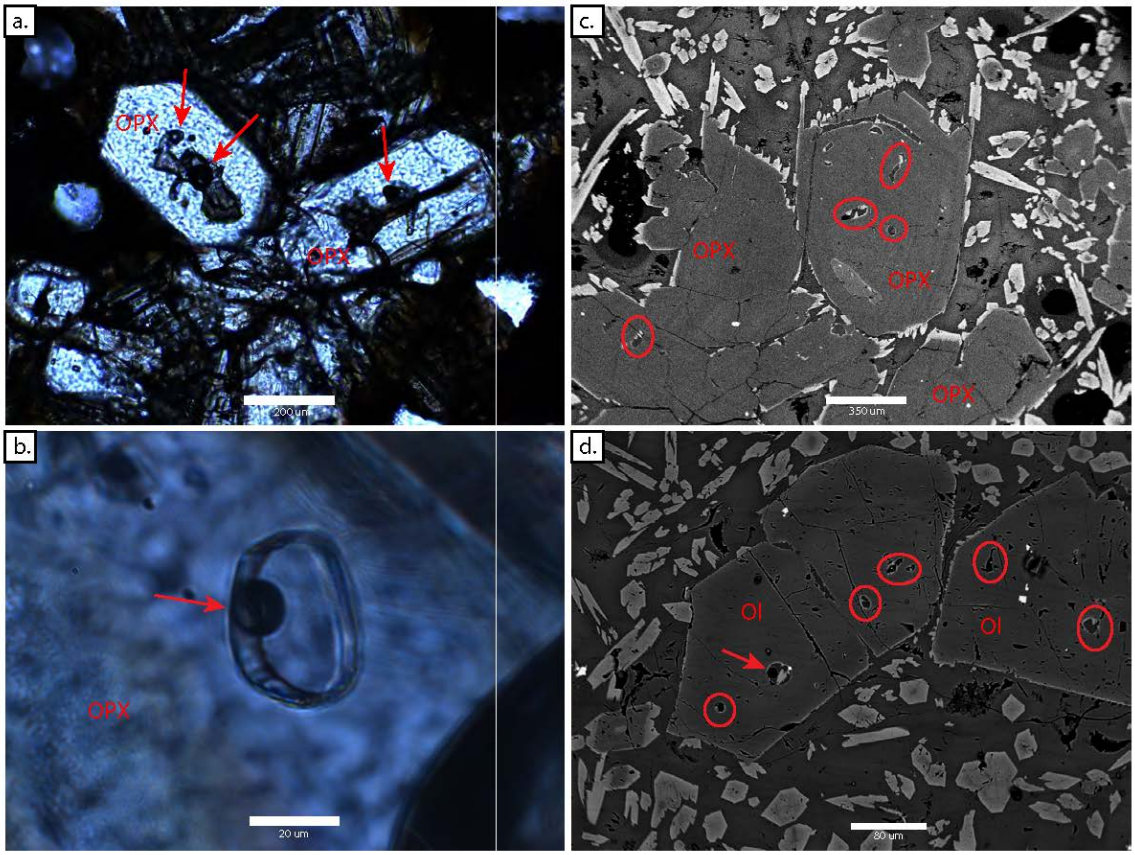

Figure 3.3
Photomicrographs (a., b.) and Backscatter Electron images (BSE) (c., d.) of melt inclusions with and without vapor bubbles. Red arrows point to vapor bubbles within melt inclusions. Red circles show melt inclusions without vapor bubbles. Orthopyroxene OPX), Olivine (Ol).

Table 3.5. FTIR Results

Sample	Number of Analysis	H_2O_T (wt%) Average	H_2O_M (wt%) Average
U1442A-48R-1W 140-142	4	1.39	0.79
U1442A-20R-1W 104-106	6	1.22	0.8
U1442A-12R-1W 35-38	3	1.36	1.36

[a] Total H_2O (H_2O_T), Molecular H_2O (H_2O_M)

Melt inclusions, some with vapor bubbles and crystals nucleating on the walls, are common in many of the samples (Figure 3.3). Melt inclusions within olivine and low-Ca pyroxenes show compositional trends similar to the interstitial glass, with andesite and dacite compositions being the most common. The andesite and dacite glass compositions have elevated Al concentrations (often >15 wt%) and depleted Mg concentrations (<2 wt%) compared to primitive boninite melts.

Measured H_2O contents of interstitial boninite glass from Hole U1442A range between 1.3-1.4 wt% (Table 3.5). Evidence for vesicularity in these and other expedition 352 boninites, especially among the uppermost HSB, indicates that our measured values are likely minima with regard to original magmatic volatile contents.

3.4. Discussion

3.4.1. Interstitial Glass and Melt Inclusions

The compositional trends in the interstitial glass and melt inclusions suggest that fractionation in Expedition 352 boninites progresses from LSB/HSB through the HMA

field and into andesite and dacite compositions (Figure 3.2.). This fractionation sequence produces end-member compositions similar to those observed in lavas recovered from the Bonin-Islands (Umino 1986; Dobson et al. 2006; Ishizuka et al. 2006; Ishizuka et al. 2011). Similar trends are also observed in "boninitic" xenolith glass and spinel inclusion studies from Kamchatka and West Bismarck (Benard et al. 2016, 2017; 2018). Benard et al. (2016, 2017, 2018) attributed these trends to orthopyroxene (Opx) and clinopyroxene (Cpx) crystallization as these are the only phases present in the xenolith glasses and spinel inclusions. Pearce and Reagan (2019) also observe similar trends in the whole-rock compositions of boninite lavas from the Bonin-Islands (specifically Chichjima). Pearce and Reagan (2019) attribute the trend in lava compositions to olivine and Opx crystallization with later Cpx crystallization. It should be noted that none of these studies observe Mg concentrations as low as some of the boninite glasses from this study, which have evolved to andesite and dacite composites.

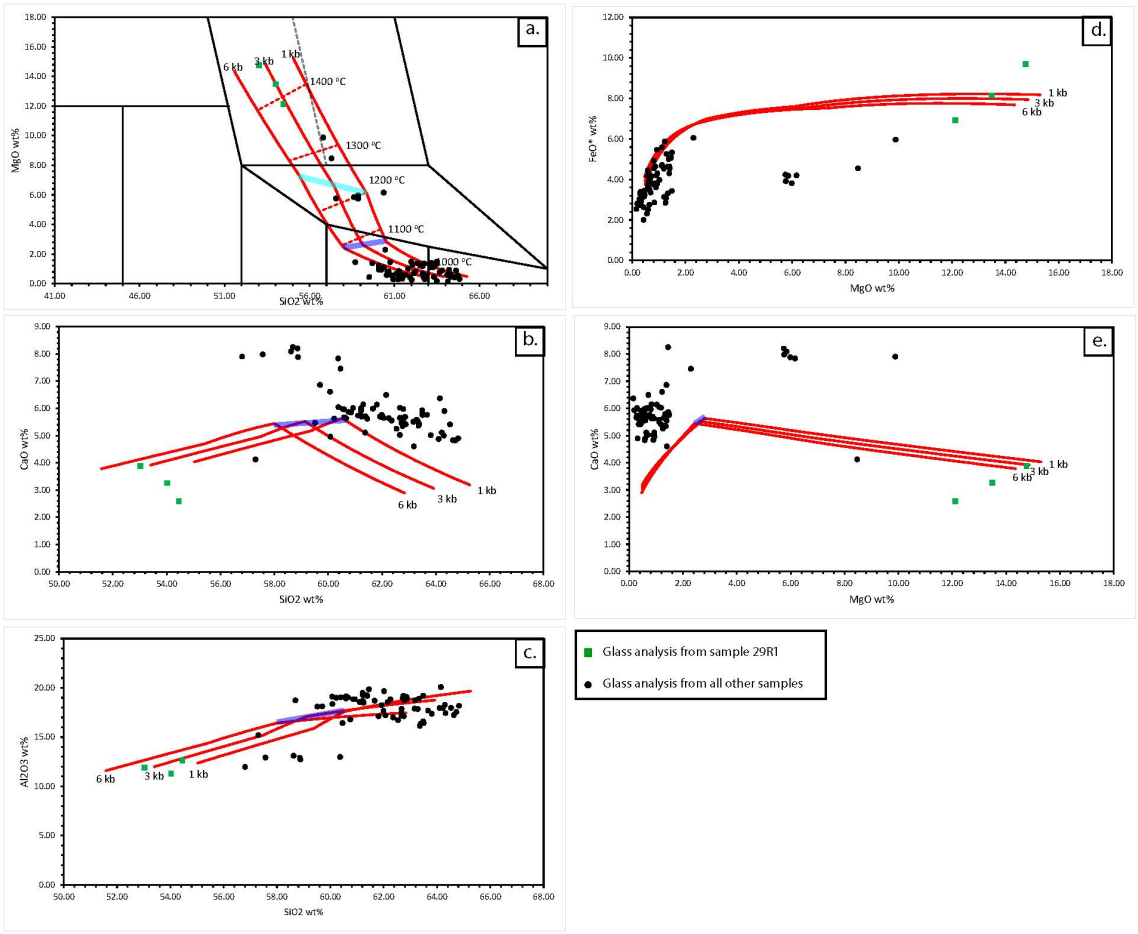

Figure 3.4
Forward model of matrix glass from sample 29R1. Red lines represent chemical evolution paths of the boninite melts during crystal fractionation. The pressure at which each model was run is indicated at the end of each line. Dashed red lines (a.) indicate the temperature the point at which the models achieve temperatures of 1400 ºC, 1300 ºC, 1200 ºC, 1100 ºC, and 1000 ºC. Purple lines (a., b., c., e.) represent the clinopyroxene (Cpx) inflection point. FeO* (Fe Total). The light blue line represents the olivine-Opx primary crystallizing phase transition (i.e., the point at which Opx becomes the primary crystallizing phase) (a.).

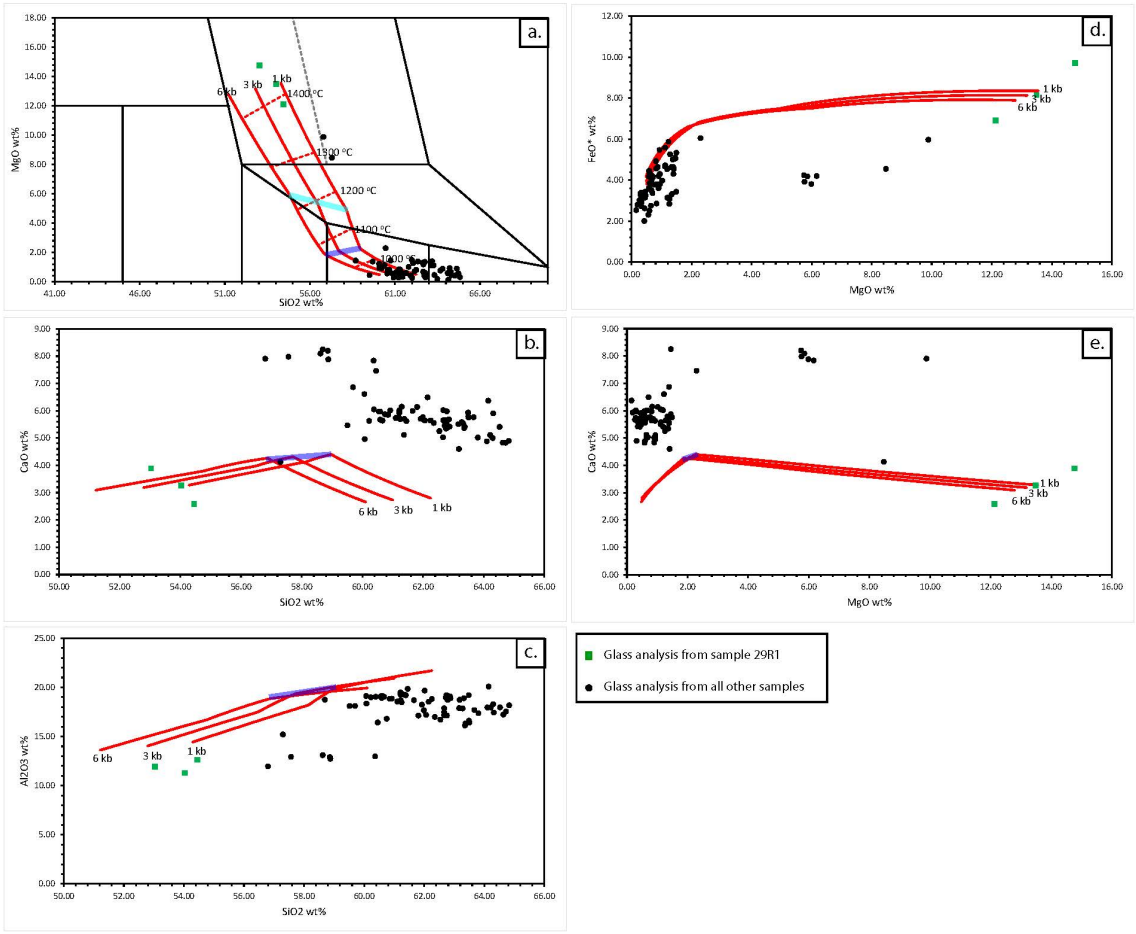

Figure 3.5
Forward model of matrix glass from sample 29R1. Red lines represent chemical evolution paths of the boninite melts during crystal fractionation. The pressure at which each model was run is indicated at the end of each line. Dashed red lines (a.) indicate the temperature the point at which the models achieve temperatures of 1400 °C, 1300 °C, 1200 °C, 1100 °C, and 1000 °C. Purple lines (a., b., c., e.) represent the clinopyroxene (Cpx) inflection point. FeO* (Fe Total). The light blue line represents the olivine-Opx primary crystallizing phase transition (i.e., the point at which Opx becomes the primary crystallizing phase) (a.).

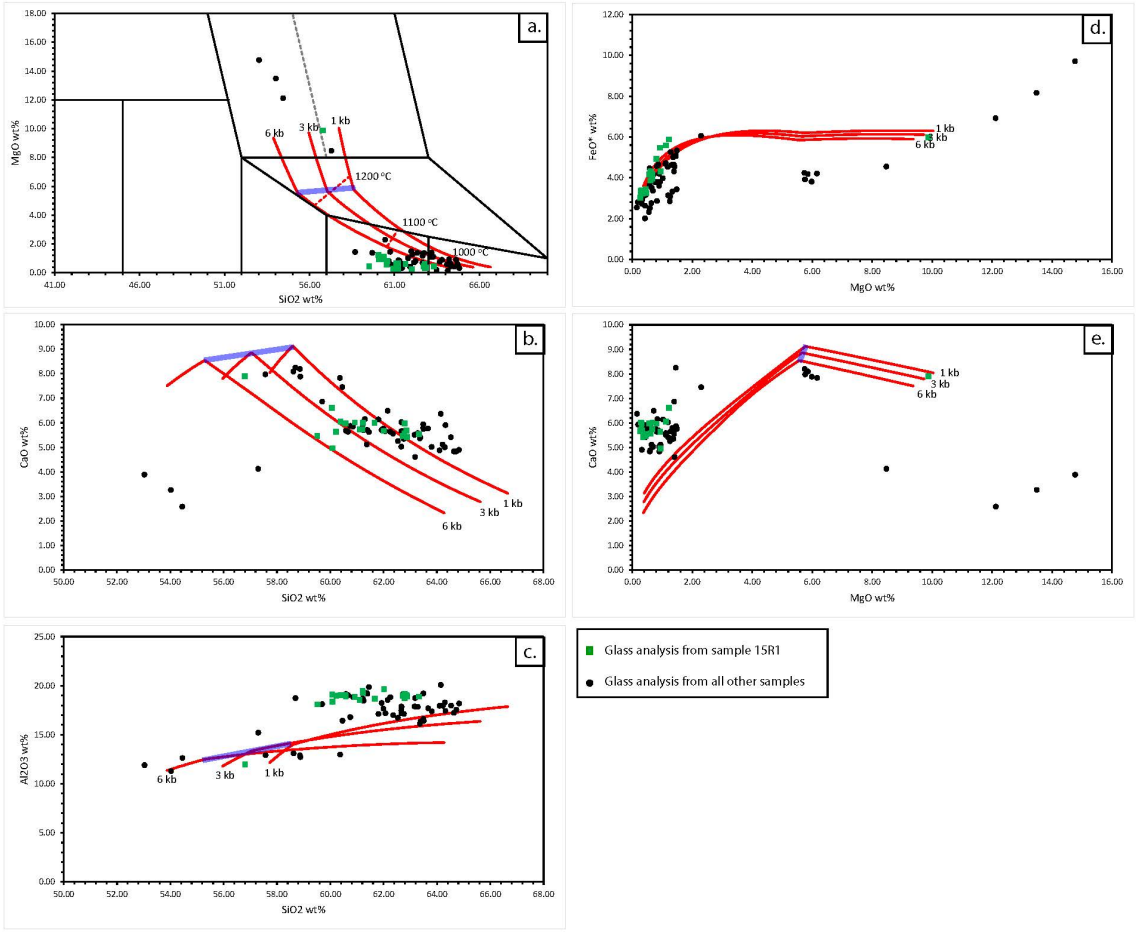

Figure 3.6
Forward model of and orthopyroxene (Opx) hosted melt inclusion from sample 15R1. Red lines represent chemical evolution paths of the boninite melts during crystal fractionation. The pressure at which each model was run is indicated at the end of each line. Dashed red lines (a.) indicate the temperature the point at which the models achieve temperatures of 1200 ºC, 1100 ºC, and 1000 ºC. Purple lines (a., b., c., e.) represent the clinopyroxene (Cpx) inflection point. FeO* (Fe Total). The light blue line represents the olivine-Opx primary crystallizing phase transition (i.e., the point at which Opx becomes the primary crystallizing phase) (a.).

3.4.2.Boninite Crystallization Models

All of the samples modeled in this study contain olivine, Opx (i.e., enstatite), and Cpx (i.e., augite), with the exception of sample 29R1, which plots in the LSB field and contains only olivine (Figure 3.4 & 3.5). Some samples also contain minor amounts of pigeonite. There is a consistent decrease in Mg# as the mineral phases become more calcic (i.e., (high Mg#) olivine>Opx>pigeonite>Cpx (low Mg#)).

All models in this study were run under water-saturated conditions since initial attempts to model the data in water undersaturated conditions required unrealistic starting H_2O contents (>10 wt% H_2O) to achieve chemical compositions similar to those observed in glasses. In water unsaturated models, chemical trends that match the data could be created with unrealistic water contents or chemical trends that would be significantly different from the data with water contents that match those observed; however, both factors would never match the data simultaneously. Most models were run at pressures between 1 and 6 kb; however, some models were also run at 0.1 kb in cases where the 1-6 kb trends appeared to be Si depleted.

Forward Models: Forward fractionation models were made for glass analysis with compositions in the boninite field of Pearce and Reagan (2019), i.e., MgO >8% at >52% SiO2. Forward fractionation models are generated by calculating the equilibrium mineral assemblage at specific pressures and water contents and subtracting that assemblage from the parent melt to determine the crystal fractionation path in composition space. The goal of forward modeling is to reproduce evolved melt compositions and determine the conditions (P, PH2O) under which fractionation occurred. These models were generated

for glass from sample 29R1 and an Mg-rich Opx-hosted melt inclusion from sample 15R1. Models were set to stop at Cpx Mg# 30 to match the low range for Cpx Mg# observed in this study. In forward models for sample 29R1, olivine, Opx, Cpx, and pigeonite were the crystallizing phases modeled (Figure 3.4 & 3.5). For the Opx-hosted inclusion from sample 15R1 (Figure 3.6), the crystallizing phases set in the model were Opx, Cpx, and pigeonite since no olivine was observed in the inclusion. There was some minor Cpx crystallization in the inclusion, these were acicular Cpx and likely formed during rapid cooling processes similar to that discussed in Scholpp et al. (in review).

Reverse Models: Reverse fractionation models were made for glass analysis with compositions in the andesite and dacite fields of Pearce and Reagan (2019). The goal of these models is to determine if the evolved glasses formed by fractionation of boninite composition melts and to assess the conditions under which this fractionation occurred. These models also allow us to estimate the parent melt composition in equilibrium with the upper mantle. In contrast to forward modeling, where equilibrium assemblages are subtracted from the melt composition, reverse fractionation involves the addition of these equilibrium phases back into the melt. Calculations are made in a stepwise fashion, such that new equilibrium phases compositions and proportions are calculated after each step, and then added back into their parent melt.

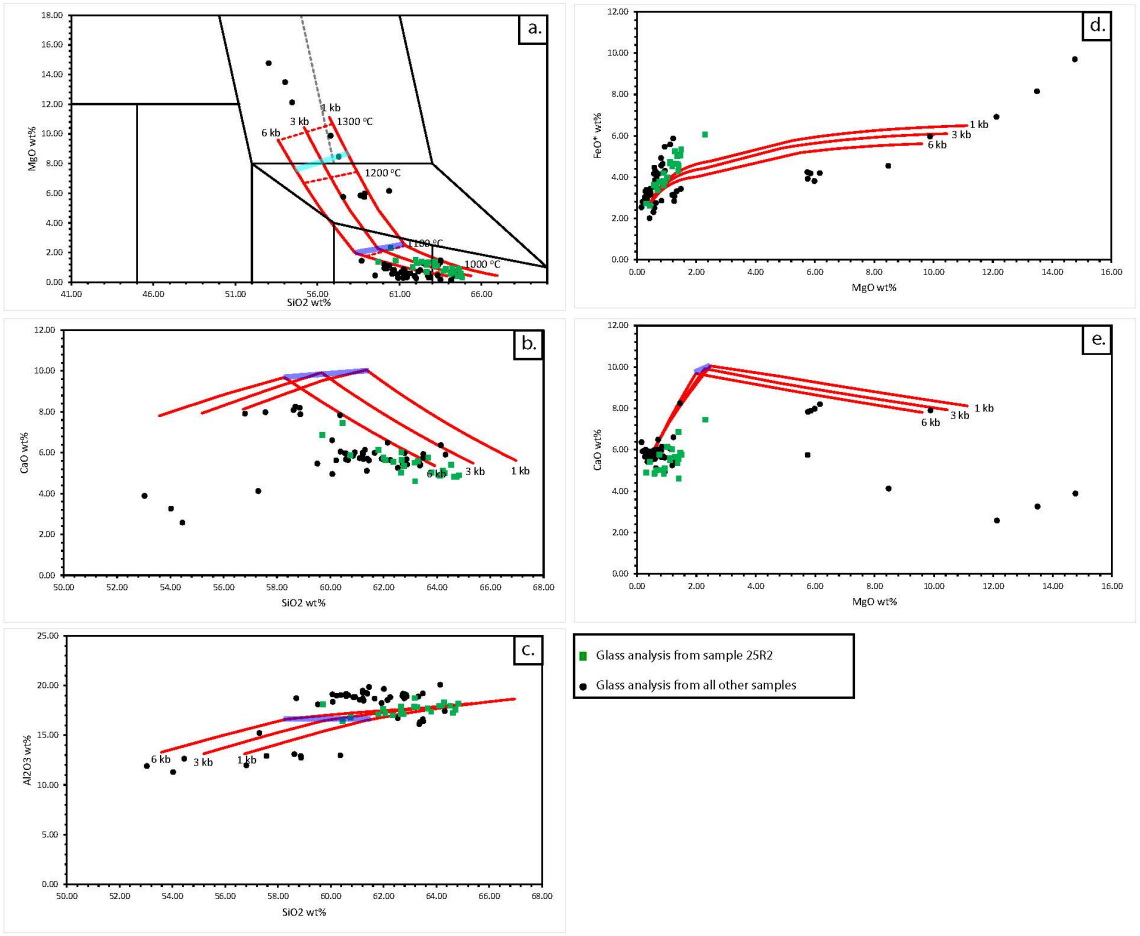

Figure 3.7
Reverse fractionation model of an olivine hosted melt inclusion from sample 25R2. Red lines represent chemical evolution paths of the boninite melts during crystal fractionation. The pressure at which each model was run is indicated at the end of each line. Dashed red lines (a.) indicate the temperature the point at which the models achieve temperatures of 1300 °C, 1200 °C, 1100 °C, and 1000 °C. Purple lines (a., b., c., e.) represent the clinopyroxene (Cpx) inflection point. FeO* (Fe Total). The light blue line represents the point at which the inclusion reaches equilibrium with the host olivine (a.).

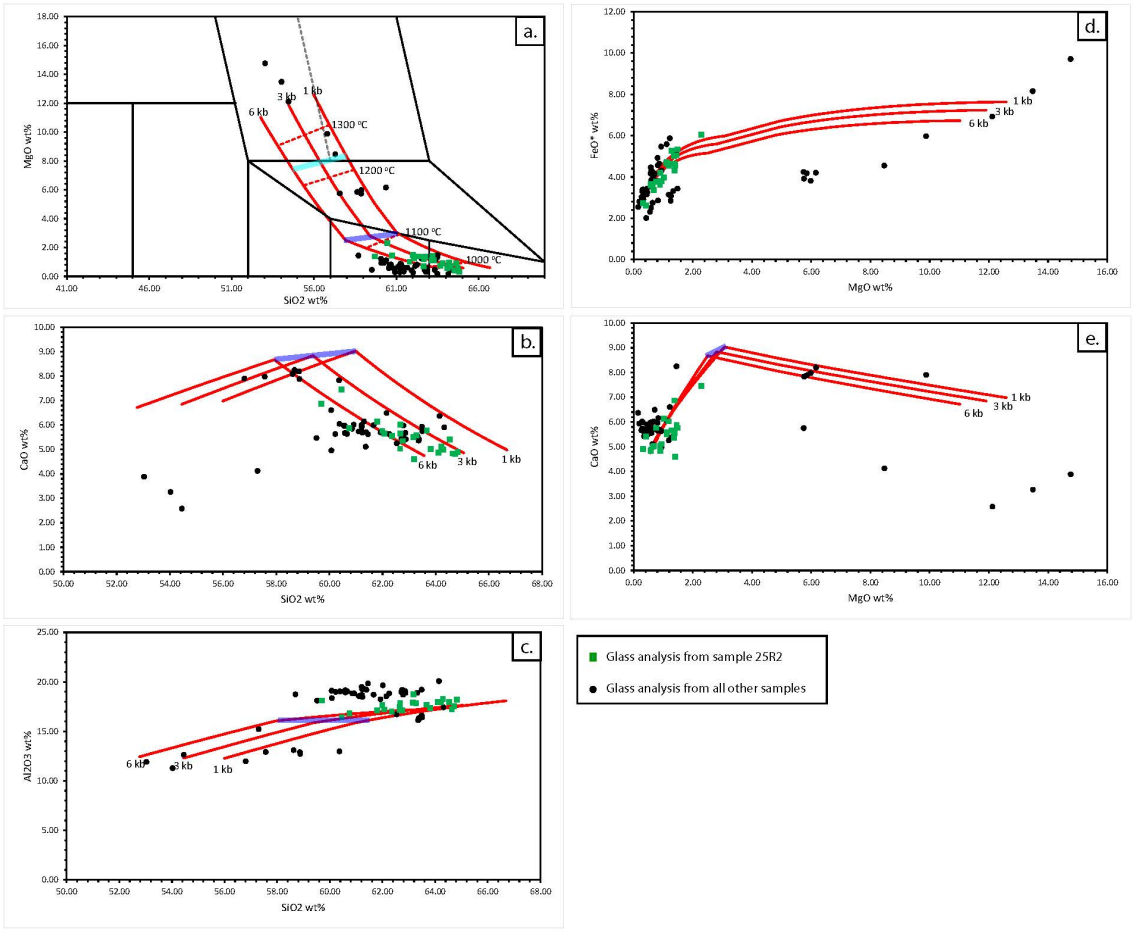

Figure 3.8
Reverse fractionation model of an olivine hosted melt inclusion from sample 25R2. Red lines represent chemical evolution paths of the boninite melts during crystal fractionation. The pressure at which each model was run is indicated at the end of each line. Dashed red lines (a.) indicate the temperature the point at which the models achieve temperatures of 1300 ºC, 1200 ºC, 1100 ºC, and 1000 ºC. Purple lines (a., b., c., e.) represent the clinopyroxene (Cpx) inflection point. FeO* (Fe Total). The light blue line represents the point at which the inclusion reaches equilibrium with the host olivine (a.).

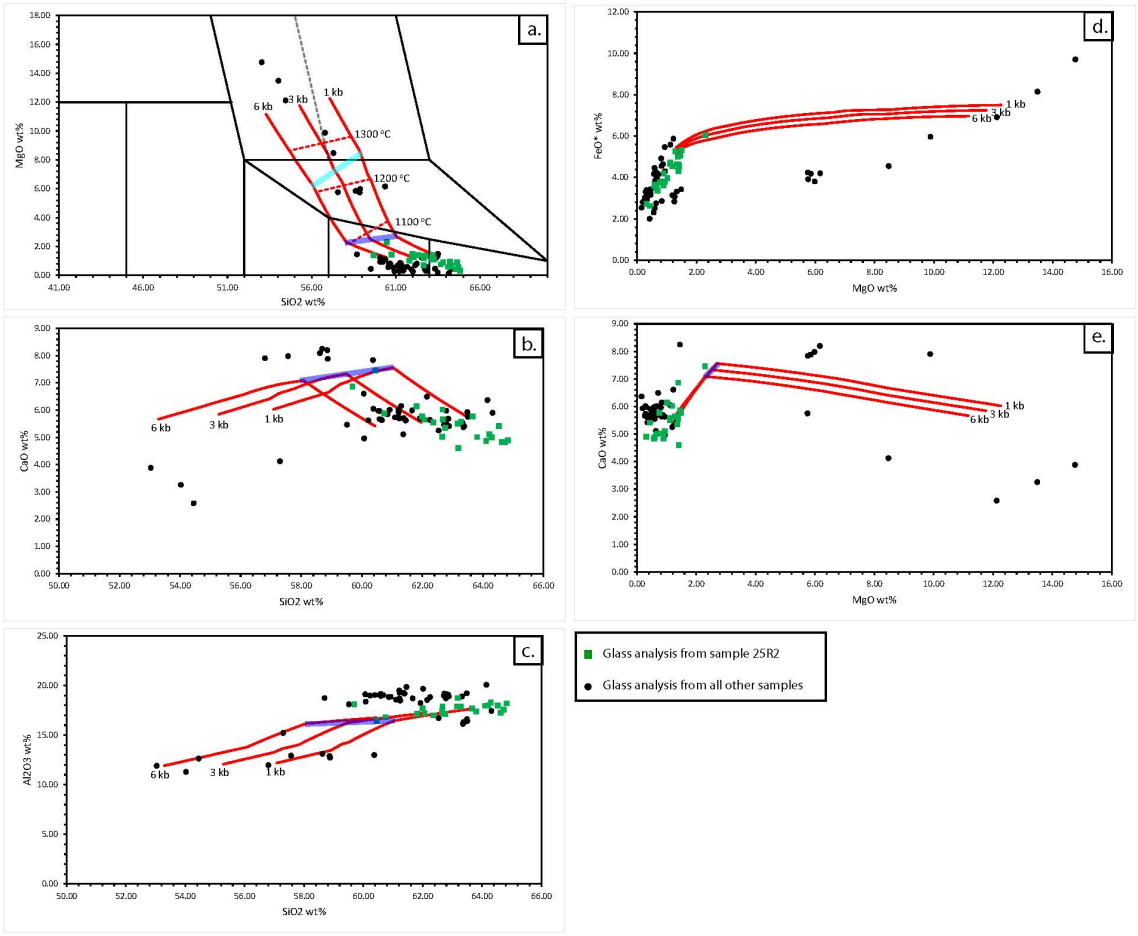

Figure 3.9

Reverse fractionation model of matrix glass from sample 25R2. Red lines represent chemical evolution paths of the boninite melts during crystal fractionation. The pressure at which each model was run is indicated at the end of each line. Dashed red lines (a.) indicate the temperature the point at which the models achieve temperatures of 1300 °C, 1200 °C, 1100 °C, and 1000 °C. Purple lines (a., b., c., e.) represent the clinopyroxene (Cpx) inflection point. FeO* (Fe Total). The light blue line represents the olivine-Opx primary crystallizing phase transition (i.e., the point at which Opx becomes the primary crystallizing phase) (a.).

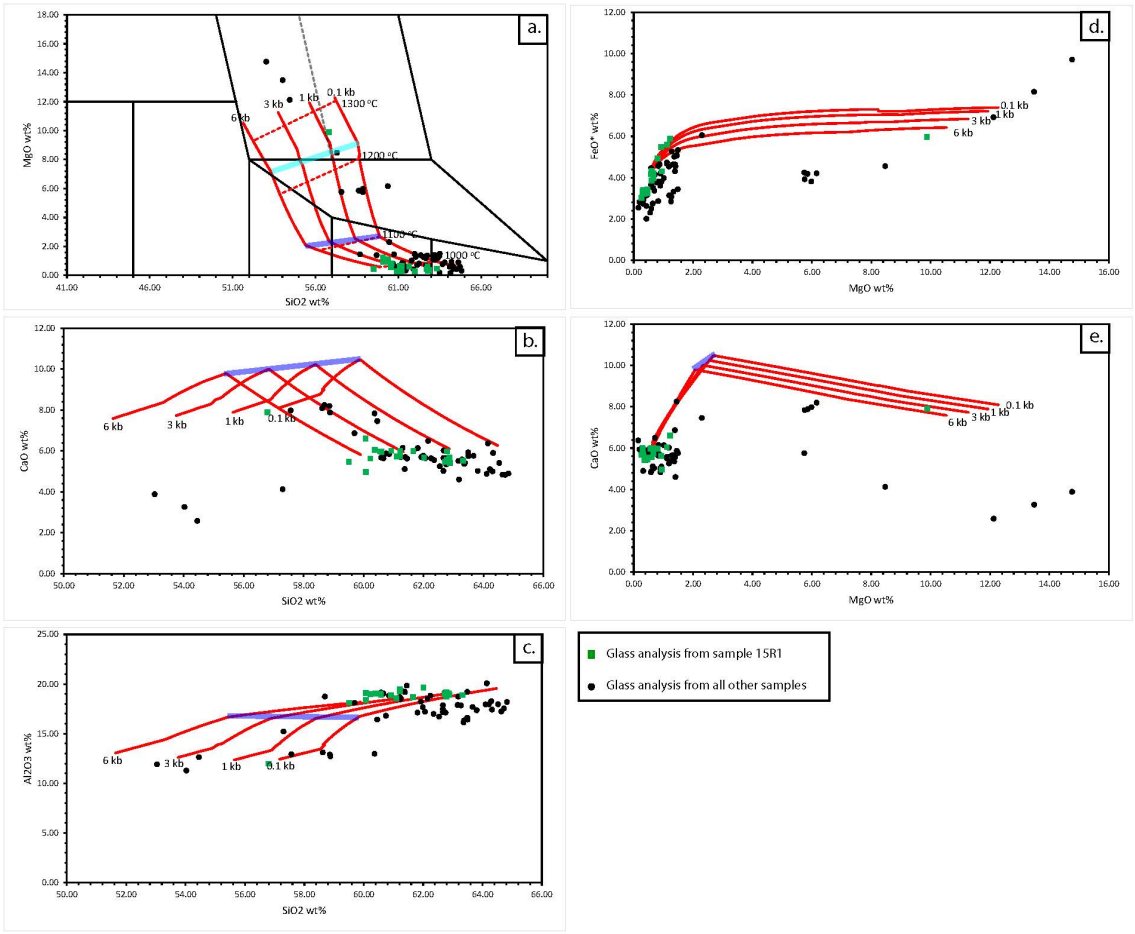

Figure 3.10
Reverse fractionation model of an orthopyroxene (Opx) hosted melt inclusion from sample 15R1. Red lines represent chemical evolution paths of the boninite melts during crystal fractionation. The pressure at which each model was run is indicated at the end of each line. Dashed red lines (a.) indicate the temperature the point at which the models achieve temperatures of 1300 °C, 1200 °C, 1100 °C, and 1000 °C. Purple lines (a., b., c., e.) represent the clinopyroxene (Cpx) inflection point. FeO* (Fe Total). The light blue line represents the olivine-Opx primary crystallizing phase transition (i.e., the point at which Opx becomes the primary crystallizing phase) (a.).

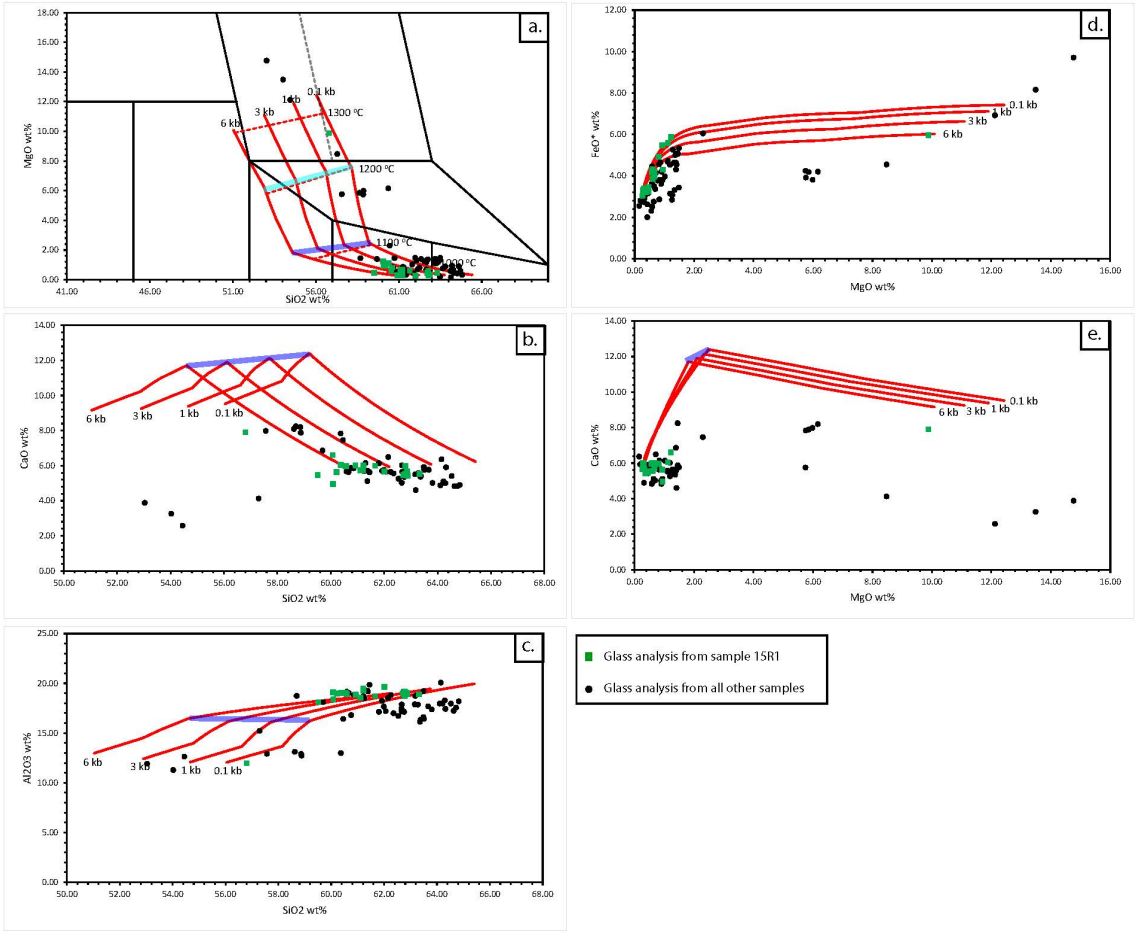

Figure 3.11
Reverse fractionation model of an orthopyroxene (Opx) hosted melt inclusion from sample 15R1. Red lines represent chemical evolution paths of the boninite melts during crystal fractionation. The pressure at which each model was run is indicated at the end of each line. Dashed red lines (a.) indicate the temperature the point at which the models achieve temperatures of 1300 °C, 1200 °C, 1100 °C, and 1000 °C. Purple lines (a., b., c., e.) represent the clinopyroxene (Cpx) inflection point. FeO* (Fe Total). The light blue line represents the olivine-Opx primary crystallizing phase transition (i.e., the point at which Opx becomes the primary crystallizing phase) (a.).

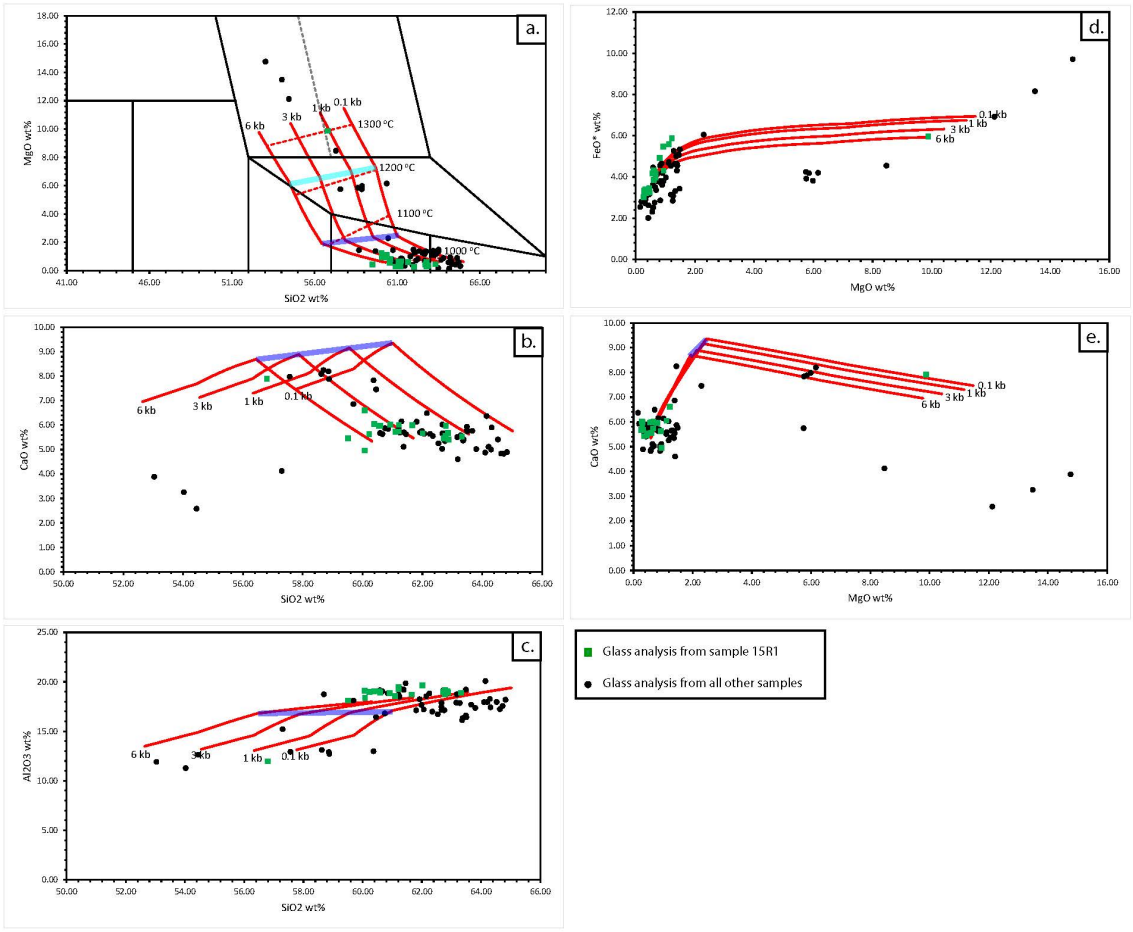

Figure 3.12
Reverse fractionation model of matrix glass from sample 15R1. Red lines represent chemical evolution paths of the boninite melts during crystal fractionation. The pressure at which each model was run is indicated at the end of each line. Dashed red lines (a.) indicate the temperature the point at which the models achieve temperatures of 1300 ºC, 1200 ºC, 1100 ºC, and 1000 ºC. Purple lines (a., b., c., e.) represent the clinopyroxene (Cpx) inflection point. FeO* (Fe Total). The light blue line represents the olivine-Opx primary crystallizing phase transition (i.e., the point at which Opx becomes the primary crystallizing phase) (a.).

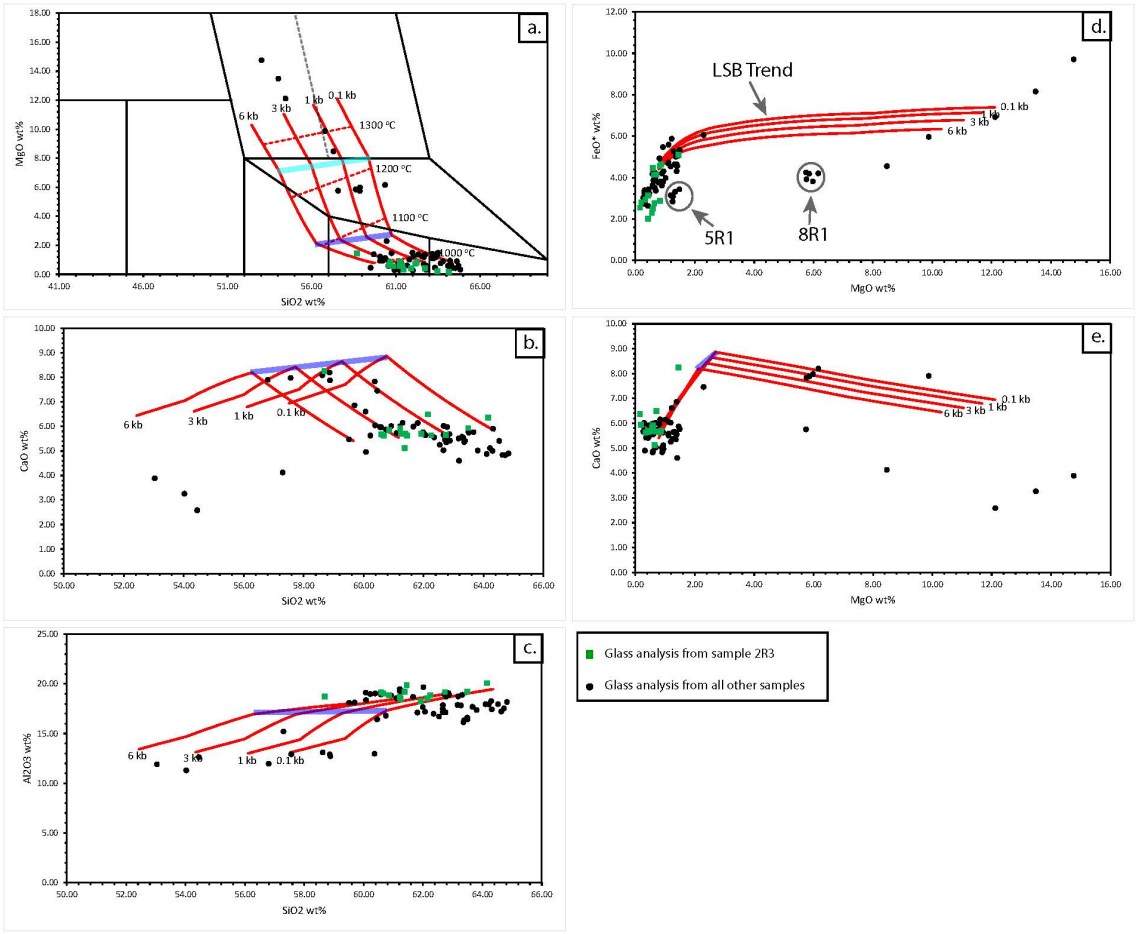

Figure 3.13
Reverse fractionation model of matrix glass from sample 2R3. Red lines represent chemical evolution paths of the boninite melts during crystal fractionation. The pressure at which each model was run is indicated at the end of each line. Dashed red lines (a.) indicate the temperature the point at which the models achieve temperatures of 1300 °C, 1200 °C, 1100 °C, and 1000 °C. Purple lines (a., b., c., e.) represent the clinopyroxene (Cpx) inflection point. FeO* (Fe Total). The light blue line represents the olivine-Opx primary crystallizing phase transition (i.e., the point at which Opx becomes the primary crystallizing phase) (a.). Glass analysis from HSB samples 8R1 and 5R1 are shown in the grey circles (d.) and be seen following a different trend from that of the LSB samples.

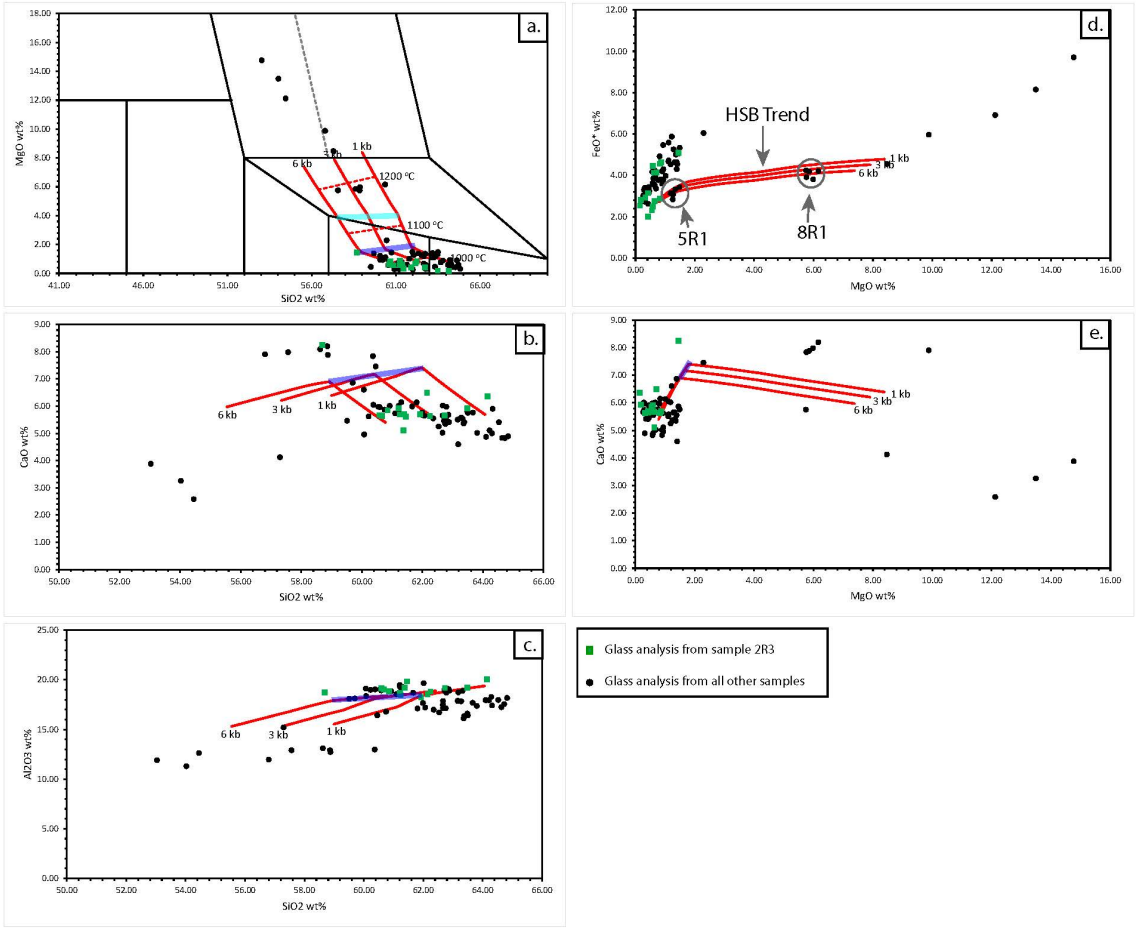

Figure 3.14
Reverse fractionation model of an orthopyroxene (Opx) hosted melt inclusion from sample 2R3. Red lines represent chemical evolution paths of the boninite melts during crystal fractionation. The pressure at which each model was run is indicated at the end of each line. Dashed red lines (a.) indicate the temperature the point at which the models achieve temperatures of 1300 ºC, 1200 ºC, 1100 ºC, and 1000 ºC. Purple lines (a., b., c., e.) represent the clinopyroxene (Cpx) inflection point. FeO* (Fe Total). The light blue line represents the olivine-Opx primary crystallizing phase transition (i.e., the point at which Opx becomes the primary crystallizing phase) (a.). Glass analysis from HSB samples 8R1 and 5R1 are shown in the grey circles (d.). Samples 8R1 and 5R1 appear to follow a similar trend to that observes in the subgroup from sample 2R3. This is labeled as the HSB trend on the graph (d.).

Reverse models were generated for interstitial glass and melt inclusions in samples 2R3, 15R1, and 25R2. These models were done in steps, depending on the phase hosting the melt inclusion or crystal assemblage of the glass. Models were broken into two to three individual steps at compositional inflection points thought to represent the onset of a new crystalline phase. This allows the software to track the observed phase assemblages more easily. Models that were broken into individual steps, controlled by observed compositions from the samples, produce mineral assemblages similar to those in the samples and follow chemical trends similar to the measure compositions in the boninites (as is discussed below).

Olivine-hosted inclusions are only found in sample 25R2. Since Cpx is the only mineral phase found within the melt inclusions, reverse fractionation was modeled in two steps: first with Cpx then with olivine. Cpx was added to the initial inclusion composition until it reached a melt composition in equilibrium with Cpx at Mg# 75, corresponding to the highest observed Cpx Mg#. Olivine was then progressively added to this melt until it was in equilibrium with Fo 92 olivine (highest observed olivine Mg#) (Figure 3.7 & 3.8) Host olivine compositions are Fo 87 and Fo 89, the point at which the inclusion reaches equilibrium with the host olivine composition is indicated in the models (Figure 3.7a. & 3.8a.).

Reverse fractionation models of interstitial glass and Opx-hosted melt inclusions were calculated in three steps, based on the presence of three mineral phases: olivine, Cpx, and Opx (Figure 3.9, 3.10, 3.11, 3.12, 3.13, & 3.14). Cpx was added to the initial composition until it reached a melt composition in equilibrium with Cpx at Mg# 70,

corresponding to the highest observed Cpx Mg# in the melt inclusions. Opx was then added progressively to that melt until it was in equilibrium with Mg# 88 Opx (highest observed Opx Mg#). Olivine was then added to that melt until it was in equilibrium with Fo 92 olivine.

3.4.3.Modeling Results

The forward models for sample 29R1 produced olivine, Opx, and Cpx with no pigeonite and bracket the measured glass compositions well (with respect to SiO_2 and MgO compositions), with most of the measured glass analysis falling between the 1 and 3 kb trends (Figure 3.4a. & 3.5a.). The model for 15R1 also crystallized Opx and Cpx with no pigeonite and has a similar pattern to the models from 29R1. The key difference between the models is the point at which Cpx enters the melt. The inflection point for 15R1 occurring before the high magnesium andesite (HMA) to andesite boundary while both models from 29R1 put the inflection point in the andesite field (Figure 3.6a.). While it is not clear why this occurred in the models, the crystallization of small amounts of Cpx (likely under disequilibrium conditions) in the inclusion from 15R1 may have altered the chemistry of the inclusion enough to change to the position of the Cpx inflection point in our modeled results.

Reverse fractionation models from samples 2R3, 15R1, and 25R2 produce similar results to the forward models (concerning SiO_2 and MgO compositions). The Cpx inflection point typically occurs when the melts reach andesitic compositions. Opx crystallization primarily occurs in HMA to LSB melt compositions. Olivine crystallization occurs in a similar melt composition range to Opx; however, olivine is the

more common phase in LSB melt compositions, while Opx is more common in HMA compositions. Reverse models also bracket most of the data between pressures of 1 to 3 kb with some variation between samples.

Both forward and reverse modeling produce similar fractionation trends with respect to SiO_2 and MgO. However, there are some noticeable differences in elements like CaO and Al_2O_3. Forward models from sample 29R1 do not reach CaO concentrations as high as those measured in the glass analysis from highly fractionated samples. The forward model of the melt inclusion from sample 15R1 does produce similar CaO concentrations to the highly fractionated samples; however, the model also produces anomalously low Al_2O_3 concentrations as well as a CaO vs. MgO trend which does not match any of the analyzed glass. All reverse models reach elevated CaO compositions similar to the forward model for sample 15R1 (Figure 3.6), while Al_2O_3 compositions are similar to those observed in forward models from sample 29R1 (Figure 3.4).

Reverse models from sample 2R3 reveal two groups of glass compositions, which vary slightly in MgO and FeO compositions (Figure 3.13 & 3.14). Melt inclusions and interstitial glass analysis plot in both groups and analyses from both microprobes used in this study plot in each group. The modeled results from this sample suggest that each group followed different fractionation paths during their chemical evolution. One group appears to follow a trend towards LSB and has a MgO vs. FeO evolution path similar to samples 15R1, 25R2, and 29R1 (Figure 3.13). The other group appears to follow a trend towards HSB and has a MgO vs. FeO evolution path, similar to samples 5R1 and 8R1 (Figure 3.14). While samples 5R1 and 8R1 were not modeled in this study, they form the

upper section of Hole U1439C in the HSB section of the core (Reagan et al. 2015, 2017). This indicates that sample 2R3 may be a mixture of LSB and HSB magmas, as hypothesized in Scholpp et al. (in review).

3.4.4.Insights from Thermometry and Barometry

Several approaches were taken to infer equilibration temperature and pressures for our samples: olivine-spinel geothermometry (Balhaus et al. 1990; Jiangping et al. 1995), two-pyroxene geothermometry (Brey and Kohler 1990), two-pyroxene thermobarometry (Putirka 2008), and olivine-liquid geothermometry (Putirka et al. 2007). The Ballhaus et al. (1990) olivine-spinel geothermometer produces temperatures 1011±60°C (Table 3.3), assuming a pressure of 0.3 GPa (3 kb), while the Jianping et al. (1995) olivine-spinel geothermometer produces temperatures of 1118±53°C at the same pressure. Two-pyroxene thermometer (i.e., Brey and Kohler 1990) and thermobarometer (i.e., Putirka 2008) produce temperatures between 1153±36 °C and 1110±34 °C for adjacent Cpx and Opx in zoned pyroxenes (Table 3.2). Barometric calculations Putirka (2008) indicate pyroxene crystallization occurred at pressures of 3±2 kb.

The Putirka et al. (2007) olivine-liquid geothermometer yields temperatures of around 1113±37°C assuming initial melt H_2O content of 5 wt.%, and 1170±41°C assuming initial melt H_2O of 2 wt.% (Table 3.1). The composition of the initial melt was calculated using the methods of Yamashita and Tatsumi (1994), assuming Fo 90-92 compositions for initial olivine, $K_d^{Fe\text{-}Mg}$ of 0.3, and a $Fe^{3+}/(Fe^{2+}+Fe^{3+})$ of 0.21 in the initial melt. While our measured H_2O contents for Expedition 352 boninites are lower, at 1.3 wt.% - 1.4 wt.% (Table 3.5), these glass measurements on what are uniformly highly vesicular rocks

probably reflect minimum values for their pre-eruptive water contents. These temperatures are in agreement with our two-pyroxene and olivine-spinel results, suggesting that this temperature range represents the magma chamber temperatures.

Although temperatures from the olivine-spinel thermometers vary, Lehmann (1983) and Ozawa (1983) have noted that olivine and Cr-spinel will re-equilibrate at lower temperatures than those at which they formed if the mineral pair remains in contact. Based on the observations of Scholpp et al. (in review), which suggest some olivine crystal may be residing magma chambers for an extended period before their eruption, it is likely that these olivine and spinel pairs have re-equilibrated at lower temperatures than those at which they formed. Jianping et al. (1995) attempted to account for the inconsistencies between the olivine-spinel thermometer of Fabries (1979) and the two pyroxene thermometers, which is likely why the calculated temperatures from this model are similar to those from the Putirka (2008) olivine-liquid geothermometer. Thus, the temperatures based on the calculations of Ballhaus et al. (1990) are essentially the minimum temperatures of the system, while the temperatures calculated from Jianping et al. (1995) and Putirka et al. (2007) are closer to the temperatures of the magma chamber.

The temperatures and pressures determined from the fractionation modeling and thermometers and barometers are similar enough to constrain the thermal evolution of these lavas prior to the eruption. However, the forward and reverse fractionation models reach higher temperatures than those determined using other thermometers and barometers. Our calculated and modeled temperatures for Expedition 352 boninites are also consistent with inferences from past studies on IBM boninites and those from

different settings (e.g., Umino 1986; Crawford et al. 1989; Dobson et al. 2006; Lee et al. 2009; Whattam et al. 2020). Although the calculated and modeled pressures are well correlated with each other and produce chemical trends consistent with the glass analysis, they are substantially higher than (1-4 kb higher) the pressures documented in Whattam et al. (2020) for IBM boninites. This is likely related to the use of different calculations in the studies, as Whattam et al. (2020) use an Opx-liquid thermobarometer (actually Opx whole-rock). However, our calculated pressures do fall between those calculated by Lee et al. (2009) for Fo92 olivine in equilibrium with a harzburgite mantle (≈8 kb, based on conditions assumed for melting beneath the IBM arc) and those of Whattam et al. (2020).

3.4.5.Comparing Models

Previous studies which attempt to model boninite fractionation have focused on melt inclusions and vein glass from mantle xenoliths which have “boninite-like” compositions (Benard et al. 2016, 2017, 2018), while other studies attempt to model boninite crystallization and its effects on melt chemistry on boninite lava (i.e., Pearce and Reagan 2019; Shervais et al. submitted). Samples from xenolith studies were recovered from western pacific arcs (i.e., Kamchatka and West Bismarck), while samples from studies on boninite lavas were recovered during IODP Expedition 352. Modeled compositions from Benard et al. (2016, 2017, 2018) are derived from a combination of heated and unheated melt inclusions, vein glass, and theoretical melts derived from lherzolite and harzburgite sources. Whole-rock compositions from primitive boninite lavas are used to model fractional crystallization in Pearce and Reagan (2019) and

Shervais et al. (submitted).

Xenolith studies do document similar HMA to dacite glass compositions. However, these studies also observe rhyolite glass and do not document any fresh boninite glass as this study does. Benard et al. (2016, 2017) also model chemical evolution paths that are noticeably different from those observed in our glass analysis and models. These chemical evolution paths cut across the LSB and HSB fields as they trend towards rhyolite or dacite (final composition is dependent on the model). This trend is similar to that of boninites from the Mariana inner trench wall (i.e., Bloomer and Hawkins 1987; Pearce and Reagan 2019), which are hypothesized to exhibit a mixing trend between LSB and siliceous magmas. Models from Benard et al. (2018) appear to follow chemical trends similar to models from this study; however, these models are made generated for pressures much higher than those in this study.

Models from this study are most similar to those of Pearce and Reagan (2019) and Shervais et al. (submitted), which are modeled from boninite parent melts at pressures between 1-3 kb. As Pearce and Reagan (2019) and Shervais et al. (submitted) model parent compositions derived from Expedition 352 boninite whole rock data, it is not surprising that our models are very similar. Thus, the primitive whole-rock compositions of Expedition 352 boninites may be acceptable for forward modeling. However, processes such as crystal accumulation (specifically olivine accumulation in most boninites) can affect the whole rock chemistry. This can be seen in the whole-rock data for boninites which have undergone extensive crystallization (Reagan et al. 2015, 2017; Pearce and Reagan 2019; Shervais et al. submitted), as many boninites never reach

andesite or dacite compositions, likely due to olivine accumulation in these magmas, which increases their whole-rock MgO concentrations (e.g., Reagan et al. 2017; Pearce and Reagan 2019; Shervais et al. submitted).

3.4.6. The Architecture of the Magmatic System

Modeled results from this study, as well as those of Pearce and Reagan (2019) and Shervais et al. (submitted), indicate that boninite lavas primarily crystallize at pressures between 1-3 kb. This is consistent with the calculated pressures of 3±2 kb. These pressures place the magmatic system in which these boninites evolve at depths of 3-10 km (assuming 1 kb≈3.3 km). Assuming that the crustal thickness during boninite volcanism is similar to that of oceanic crust (6-7 km thick: Perfit, 2001), these calculated and modeled pressures suggest that boninite crystallization primarily occurs from the base to middle of the crustal section.

Large olivine xenocrysts with homogenous chemical compositions and resorbed rims observed by Scholpp et al. (in review) indicate that boninite magmas likely enter a magma chamber through a crystal mush zone or cumulate pile at its base. Based on the hypothesis of Reagan et al. (2015, 2017, 2019) and Shervais et al. (submitted) that LSB volcanism is related to spreading, we suggest that the magmatic system in which LSB form is similar to that at mid-ocean ridges and during fore-arc basalt (FAB) volcanism. These are likely composite magma chambers with large crystal mush zones and small lenses of molten magma, as the petrologic variations and mixing evidence observed at mid-ocean ridges, are difficult to produce in large well-mixed chambers (Langmuir et al.

1986; Bloomer et al. 1989; Sinton et al. 1991; Sinton and Detrick 1992; Sours-Page et al. 2002; Rubin et al. 2009; Costa et al. 2010). Thus, we suggest that the magma chamber (the melt lens within the system) exists at depths between 3 and 6 km, and overlies a crystal mush zone through which the melt migrate.

The magmatic system for HSB is harder to constrain since observations from Reagan et al. (2017, 2019) and Shervais et al. (submitted) indicate that there is a change in the melt source, and hypothesize that HSB is transitional lavas generated as the system transitions from spreading to proto-arc magmatism. However, the chemical trends observed in sample 2R3 suggest that LSB was still produced during this transitional phase and likely mixing with HSB magmas before eruption (Figure 3.13 & 3.14). If the spreading rate was decreasing at that point, it is likely that the magmatic system at this point consisted of multiple less localized melt lenses throughout a crystal mush zone since there was likely less magma supplied to the system making large melt bodies unlikely (Casey and Karson 1981; Sinton and Dietrick 1992; Sours-Page et al. 2002; Carbotte et al. 2013). Although the data from this study and previous work suggest the HSB magmatic system is different, the pressure and temperature calculations and models from this study indicate that HSB magmas were evolving at similar pressures and temperatures to LSB magmas.

3.5. Future Work

In light of the results from this study, additional analysis on boninite lavas from IODP Expedition 352 must be done to better constrain the unique fractionation trend of HSB melts. First, more EPMA analysis with be done on HSB interstitial glass and melt

inclusions, in an attempt to create a more robust data set for the fraction trend of HSB melts. This will also be done for lavas from the basaltic boninite (BSB) section of Hole U1439C described in Reagan et al. (2015, 2017) to determine their relation to the other boninite subgroups from this study. We will complete this work at the electron microprobe laboratory at the University of Tennessee-Knoxville.

Second, we will conduct laser ablation inductively coupled plasma mass spectrometry (LA-ICP-MS) and secondary ion mass spectrometry (SIMS) analysis on interstitial glass and melt inclusions from LSB, HSB, and BSB lavas. This will provide trace element and isotopic data and allow us to determine whether the difference in LSB, HSB, and BSB lava compositions is related chemical to changes in the melt source or differences in P-T conditions and crystal fractionation during the melts ascent. We will analyze samples at the University of South Florida (for LA-ICP-MS) and the University of Wisconsin-Madison (for SIMS).

Third, we will conduct high pressure and temperature reheating experiments on samples which contain melt inclusions with vapor bubbles. Laser Raman spectroscopic (LRS) analysis will also be conducted to determine the chemical composition of the vapor bubbles. From these analyses, we can evaluate the P-T conditions at which the dissolved gasses would have been in equilibrium with the boninite melts. In addition, we will be able at changes in boninite gas compositions as the magmatic systems and melt sources changed and evolve. We will complete this work at the fluid and melt inclusions lab at the University of Wisconsin-Madison.

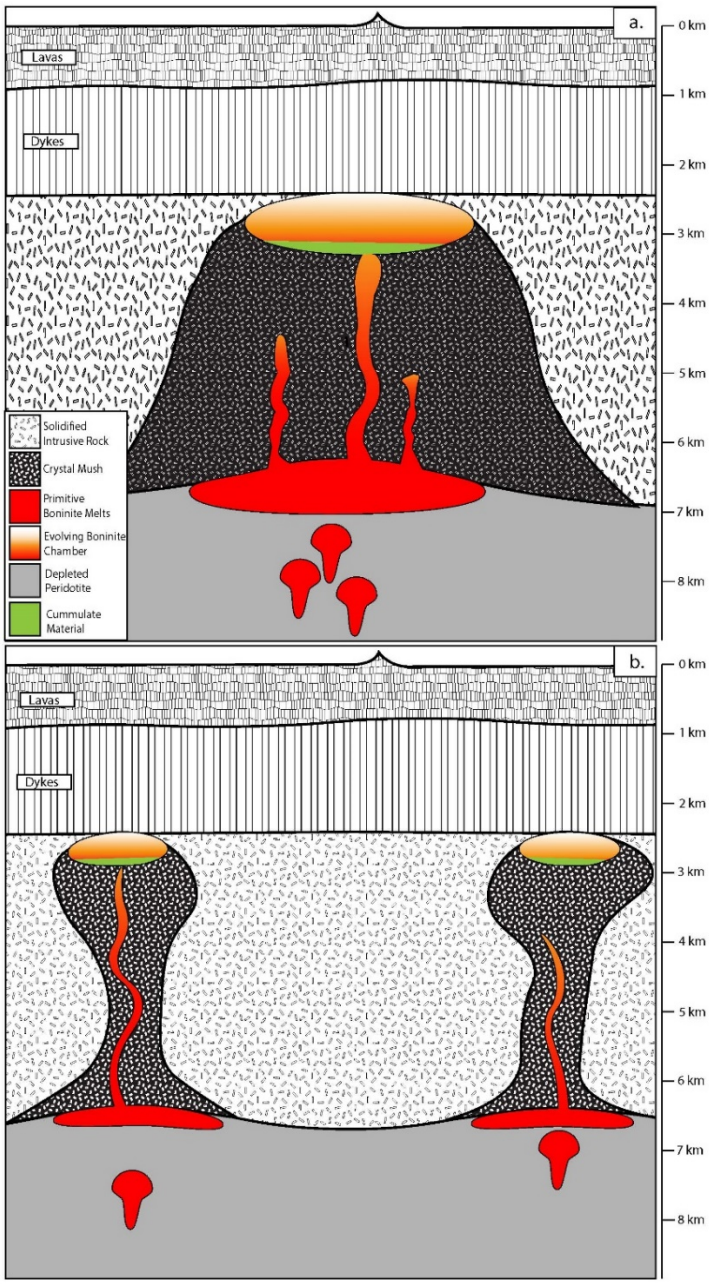

Figure 3.15
Boninite magma chamber models for LSB (a.) and HSB (b.) volcanism. During LSB volcanism, melts are generated and erupt from an axial volcanic system (a.). During HSB volcanism, melts are generated in multiple mantle sources and emplaced within the crust at numerous locations (b.). In both volcanic systems, primitive boninite melts pond beneath the fore-arc crust before ascending through a crystal mush zone. Primitive melts begin to crystallize as they migrate through the crystal mush, ascending towards a fractionating magma chamber with a cumulate pile.

3.6. Conclusions

The models from this study are a powerful tool for understanding the chemical evolution of boninite magmas during crystallization and the architecture of the magmatic system present during early subduction volcanism. Boninite melts primarily crystallize olivine and Opx as they evolve from LSB/HSB through HMA compositions with late crystallizing Cpx driving melts from andesite to dacite compositions. Pigeonite can form in melts that experience significant undercooling events; however, pigeonite crystallization has little effect on the overall melt compositions.

Thermometry and barometry calculations indicate that crystallization occurred between 1200°C and 1000°C, at pressures around 3 kb. While this is in agreement with the pressures modeled in this study and Pearce and Reagan (2019), the temperatures in our model reverse and forward models indicate that olivine and higher Mg# Opx grains likely crystallized at higher temperatures. We conclude that the calculated pressures and temperatures from this study represent the conditions within the magma chamber and the higher modeled temperatures represent the conditions experienced during ascent, before being injected into the magma chamber. This means that some crystallization did occur at higher pressures and temperatures; however, the majority of crystallization occurred within a magma chamber at pressures and temperatures calculated in this study.

The magmatic system present during LSB volcanism likely resembled that of mid-ocean ridge magmatic systems based on the results of this study and the conclusions of Reagan et al. (2015, 2017, 2019) and Shervais et al. (submitted), which indicate that LSB lavas likely erupted from and axial spreading center. This was probably a composite axial

magma chamber with small pockets of eruptible melt underlain by a crystal mush zone (Casey and Karson 1981; Sinton and Detrick 1992; Sours-Page et al. 2002; Rubin et al. 2009; Carbotte et al. 2013). As melts were generated and entered the chamber, they would migrate through and interact with the crystal mush, possibly resulting in the mixing textures and chemistry observed in Scholpp et al. (in review).

It is less clear what the magmatic system during HSB volcanism would have looked like based on the data acquired in this study. However, calculated pressures and temperatures for sample 2R3 from the HSB section indicate that crystallization likely occurred at similar P-T conditions in both magmatic systems. Modeled results from sample 2R3 indicate that LSB melts were still being produced during the period of off-axis HSB volcanism. It is not clear whether HSB and LSB melts mingled often; however, the magma mixing textures (i.e., Scholpp et al. in review) and dual chemical evolution paths representing HSB fractionation and LSB fractionation observed in sample 2R3 show the mixing occurred during the pre-eruptive history of this sample. We suggest that the HSB volcanic system consisted of multiple small melt lenses that were not localized beneath a spreading center (Figure 3.15). These melt lenses would have primarily included HSB melts with occasional LSB melt lenses, as small amounts of LSB melts were still being produced.

3.7. References

Arculus, R.J., Pearce, J.A., Murton, B.J., and Van der Laan, S.R. (1992) Igneous stratigraphy and major element geochemistry of Holes 786A and 786B. In Proceedings of the Ocean Drilling Program, Scientific Results Vol. 125, pp. 143–169. Ocean Drilling Program, College Station, TX.

Ariskin, A.A., Frenkel, M.Ya., Barmina, G.S., and Nielsen, R.L. (1993) Comagmat: a Fortran program to model magma differentiation processes. Computers & Geosciences, 19, 1155–1170.

Ballhaus, C., Berry, R.F., and Green, D.H. (1990) Oxygen fugacity controls in the Earth's upper mantle. Nature, 348, 437.

Bédard, J.H., Lauzière, K., Tremblay, A., and Sangster, A. (1998) Evidence for forearc seafloor-spreading from the Betts Cove ophiolite, Newfoundland: oceanic crust of boninitic affinity. Tectonophysics, 284, 233–245.

Bénard, A., Nebel, O., Ionov, D.A., Arculus, R.J., Shimizu, N., and Métrich, N. (2016) Primary silica-rich picrite and high-Ca boninite melt inclusions in pyroxenite veins from the Kamchatka sub-arc mantle. Journal of Petrology, 57, 1955–1982.

Bénard, A., Arculus, R.J., Nebel, O., Ionov, D.A., and McAlpine, S.R.B. (2017) Silica-enriched mantle sources of subalkaline picrite-boninite-andesite island arc magmas. Geochimica et Cosmochimica Acta, 199, 287–303.

Bénard, A., Le Losq, C., Nebel, O., and Arculus, R.J. (2018) Low-Ca boninite formation by second-stage melting of spinel harzburgite residues at mature subduction zones: new evidence from veined mantle xenoliths from the West Bismarck Arc. Contributions to Mineralogy and Petrology, 173, 105.

Bloomer, S.H. (1979) Mariana arc-trench studies: Petrology of boninites and evidence for a" boninite series". EOS (Amer. Geophys. Union Trans.), 60, 968.

Bloomer, S.H., and Hawkins, J.W. (1987) Petrology and geochemistry of boninite series volcanic rocks from the Mariana trench. Contributions to Mineralogy and Petrology, 97, 361–377.

Brey, G.P., and Köhler, T. (1990) Geothermobarometry in four-phase lherzolites II. New thermobarometers, and practical assessment of existing thermobarometers. Journal of Petrology, 31, 1353–1378.

Cameron, W.E. (1985) Petrology and origin of primitive lavas from the Troodos ophiolite, Cyprus. Contributions to Mineralogy and Petrology, 89, 239–255.

Cameron, W.E., Nisbet, E.G., and Dietrich, V.J. (1979) Boninites, komatiites and ophiolitic basalts. Nature, 280, 550–553.

Cameron, W.E., McCulloch, M.T., and Walker, D.A. (1983) Boninite petrogenesis: Chemical and Nd-Sr isotopic constraints. Earth and Planetary Science Letters, 65, 75–89.

Carbotte, S.M., Marjanović, M., Carton, H., Mutter, J.C., Canales, J.P., Nedimović, M.R., Han, S., and Perfit, M.R. (2013) Fine-scale segmentation of the crustal magma reservoir beneath the East Pacific Rise. Nature Geoscience, 6, 866.

Casey, J.F., and Karson, J.A. (1981) Magma chamber profiles from the Bay of Islands ophiolite complex. Nature, 292, 295–301.

Costa, F., Coogan, L.A., and Chakraborty, S. (2010) The time scales of magma mixing and mingling involving primitive melts and melt–mush interaction at mid-ocean ridges. Contributions to Mineralogy and Petrology, 159, 371–387.

Crawford, A.J., Falloon, T.J., and Green, D.H. (1989) Classification, petrogenesis and tectonic setting of boninites.

Danyushevsky, L.V., and Plechov, P. (2011) Petrolog3: Integrated software for modeling crystallization processes. Geochemistry, Geophysics, Geosystems, 12.

Dick, H.J.B., Bryan, W.B., Dmitriev, L., Heirtzler, J., Aguilar, R., Cambon, P., Dungan, M., Erickson, A., Hodges, F.N., Honnorez, J., and others (1979) Variation of basalt phenocryst mineralogy and rock compositions in DSDP Hole 396B. Initial Reports of the Deep Sea Drilling Project, 46, 215–225.

Dietrich, V., Emmermann, R., Oberhänsli, R., and Puchelt, H. (1978) Geochemistry of basaltic and gabbroic rocks from the West Mariana basin and the Mariana trench. Earth and Planetary Science Letters, 39, 127–144.

Dixon, J.E., and Clague, D.A. (2001) Volatiles in basaltic glasses from Loihi Seamount, Hawaii: Evidence for a relatively dry plume component. Journal of Petrology, 42, 627–654.

Dixon, J.E., Stolper, E.M., and Holloway, J.R. (1995) An experimental study of water and carbon dioxide solubilities in mid-ocean ridge basaltic liquids. Part I: calibration and solubility models. Journal of Petrology, 36, 1607–1631.

Dobson, P.F., Blank, J.G., Maruyama, S., and Liou, J.G. (2006) Petrology and geochemistry of boninite-series volcanic rocks, Chichi-Jima, Bonin Islands, Japan. International Geology Review, 48, 669–701.

Fabriès, J. (1979) Spinel-olivine geothermometry in peridotites from ultramafic complexes. Contributions to Mineralogy and Petrology, 69, 329–336.

Falloon, T.J., and Crawford, A.J. (1991) The petrogenesis of high-calcium boninite lavas dredged from the northern Tonga ridge. Earth and Planetary Science Letters, 102, 375–394.

Hickey, R.L., and Frey, F.A. (1982) Geochemical characteristics of boninite series volcanics: implications for their source. Geochimica et Cosmochimica Acta, 46, 2099–2115.

Ihinger, P.D., Hervig, R.L., and McMillan, P.F. (1994) Analytical methods for volatiles in glasses. Reviews in Mineralogy and Geochemistry, 30, 67–121.

Ishikawa, T., Umino, S., and Kazuya, N. (2002) Boninitic volcanism in the Oman ophiolite: Implications for thermal condition during transition from spreading ridge to arc. Geology, 30, 899–902.

Ishikawa, T., Fujisawa, S., Nagaishi, K., and Masuda, T. (2005) Trace element characteristics of the fluid liberated from amphibolite-facies slab: Inference from the metamorphic sole beneath the Oman ophiolite and implication for boninite genesis. Earth and Planetary Science Letters, 240, 355–377.

Ishizuka, O., Kimura, J.-I., Li, Y.B., Stern, R.J., Reagan, M.K., Taylor, R.N., Ohara, Y., Bloomer, S.H., Ishii, T., Hargrove, U.S., and others (2006) Early stages in the evolution of Izu–Bonin arc volcanism: New age, chemical, and isotopic constraints. Earth and Planetary Science Letters, 250, 385–401.

Ishizuka, O., Taylor, R.N., Yuasa, M., and Ohara, Y. (2011) Making and breaking an island arc: A new perspective from the Oligocene Kyushu-Palau arc, Philippine Sea. Geochemistry, Geophysics, Geosystems, 12.

Jaques, A.L. (1981) Petrology and petrogenesis of cumulate peridotites and gabbros from the Marum ophiolite complex, northern Papua New Guinea. Journal of Petrology, 22, 1–40.

Jianping, L., Kornprobst, J., Vielzeuf, D., and Fabriès, J. (1995) An improved experimental calibration of the olivine-spinel geothermometer. Chinese Journal of Geochemistry, 14, 68–77.

Kyser, T.K., Cameron, W.E., and Nisbet, E.G. (1986) Boninite petrogenesis and alteration history: constraints from stable isotope compositions of boninites from Cape Vogel, New Caledonia and Cyprus. Contributions to Mineralogy and Petrology, 93, 222–226.

Langmuir, C.H., Bender, J.F., and Batiza, R. (1986) Petrological and tectonic segmentation of the East Pacific Rise, 5°30′–14°30′ N. Nature, 322, 422–429.

Lee, C.-T.A., Luffi, P., Plank, T., Dalton, H., and Leeman, W.P. (2009) Constraints on the depths and temperatures of basaltic magma generation on Earth and other terrestrial planets using new thermobarometers for mafic magmas. Earth and Planetary Science Letters, 279, 20–33.

Lehmann, J. (1983) Diffusion between olivine and spinel: application to geothermometry. Earth and Planetary Science Letters, 64, 123–138.

Meffre, S., Falloon, T.J., Crawford, T.J., Hoernle, K., Hauff, F., Duncan, R.A., Bloomer, S.H., and Wright, D.J. (2012) Basalts erupted along the Tongan fore arc during subduction initiation: Evidence from geochronology of dredged rocks from the Tonga fore arc and trench. Geochemistry, Geophysics, Geosystems, 13.

Meijer, A. (1980) Primitive Arc Volcanism and a Boninite Series: Examples from Western Pacific Island Arcs. In The Tectonic and Geologic Evolution of Southeast Asian Seas and Islands pp. 269–282. American Geophysical Union (AGU).

Meijer, A., Anthony, E., and Reagan, M. (1982) Petrology of volcanic-rocks from the fore-arc sites. Initial Reports of the Deep Sea Drilling Project, 60, 709–729.

Ozawa, K. (1983) Evaluation of olivine-spinel geothermometry as an indicator of thermal history for peridotites. Contributions to Mineralogy and Petrology, 82, 52–65.

Pagé, P., Bédard, J.H., Schroetter, J.-M., and Tremblay, A. (2008) Mantle petrology and mineralogy of the Thetford Mines Ophiolite Complex. Links Between Ophiolites and LIPs in Earth History, 100, 255–292.

Pagé, P., Bédard, J.H., and Tremblay, A. (2009) Geochemical variations in a depleted fore-arc mantle: The Ordovician Thetford Mines Ophiolite. Mantle Dynamics and Crust-Mantle Interactions in Collisional Orogens, 113, 21–47.

Pearce, J.A., and Reagan, M.K. (2019) Identification, classification, and interpretation of boninites from Anthropocene to Eoarchean using Si-Mg-Ti systematics. Geosphere, 15, 1008–1037.

Pearce, J.A., van der Laan, S.R., Arculus, R.J., Murton, B.J., Ishii, T., Peate, D.W., and Parkinson, I.J. (1992) Boninite and harzburgite from Leg 125 (Bonin-Mariana forearc): A case study of magma genesis during the initial stages of subduction. In Proceedings of the ocean drilling program, scientific results Vol. 125, pp. 623–659. Citeseer.

Perfit, M.R. (2001) Mid-ocean ridge geochemistry and petrology. Encyclopedia of Ocean Sciences, 3, 1778–1788.

Putirka, K.D. (2008) Thermometers and Barometers for Volcanic Systems. Reviews in Mineralogy and Geochemistry, 69, 61–120.

Putirka, K.D., Perfit, M., Ryerson, F.J., and Jackson, M.G. (2007) Ambient and excess mantle temperatures, olivine thermometry, and active vs. passive upwelling. Chemical Geology, 241, 177–206.

Reagan, M.K., Pearce, J.A., Petronotis, K., and Expedition 352 Scientists (2015) Expedition 352 summary. Proceedings of the International Ocean Discovery Program, 352, 1–32.

Reagan, M.K., Pearce, J.A., Petronotis, K., Almeev, R.R., Avery, A.J., Carvallo, C., Chapman, T., Christeson, G.L., Ferré, E.C., Godard, M., and others (2017) Subduction initiation and ophiolite crust: new insights from IODP drilling. International Geology Review, 59, 1439–1450.

Reagan, M.K., Heaton, D.E., Schmitz, M.D., Pearce, J.A., Shervais, J.W., and Koppers, A.A.P. (2019) Forearc ages reveal extensive short-lived and rapid seafloor spreading following subduction initiation. Earth and Planetary Science Letters, 506, 520–529.

Rubin, K.H., Sinton, J.M., Maclennan, J., and Hellebrand, E. (2009) Magmatic filtering of mantle compositions at mid-ocean-ridge volcanoes. Nature Geoscience, 2, 321.

Scholpp, J.L., Ryan, J.G., Shervais, J.W., Stremtan, C., Rittner, M., Luna, A., Hill, S.A., and Mack, B.C. (in review.) Petrologic Evolution Of Boninite Lavas From The IBM Fore-Arc, IODP Expedition 352: Evidence For Open-System Processes During Early Subdcution Zone Magmatism. American Mineralogist.

Shervais, J.W., Reagan, M., Godard, M., Prytulak, J., Ryan, J.G., Pearce, J.A., Almeev, R.R., Li, H., Haugen, E., Chapman, T., and others (Submitted) Magmatic Response to Subduction Initiation, Part II: Boninites and related rocks of the Izu-Bonin Arc from IODP Expedition 352. Geochemistry, Geophysics, Geosystems.

Sinton, J.M., and Detrick, R.S. (1992) Mid-ocean ridge magma chambers. Journal of Geophysical Research: Solid Earth, 97, 197–216.

Sinton, J.M., Smaglik, S.M., Mahoney, J.J., and Macdonald, K.C. (1991) Magmatic processes at superfast spreading mid-ocean ridges: Glass compositional variations along the East Pacific Rise 13°–23°S. Journal of Geophysical Research: Solid Earth, 96, 6133–6155.

Sours-Page, R., Nielsen, R.L., and Batiza, R. (2002) Melt inclusions as indicators of parental magma diversity on the northern East Pacific Rise. Melt Inclusions at the Millennium: Toward a Deeper Understanding of Magmatic Processes, 183, 237–261.

Taylor, R.N., Nesbitt, R.W., Vidal, P., Harmon, R.S., Auvray, B., and Croudace, I.W. (1994) Mineralogy, Chemistry, and Genesis of the Boninite Series Volcanics, Chichijima, Bonin Islands, Japan. Journal of Petrology, 35, 577–617.

Umino, S. (1986) Magma mixing in boninite sequence of Chichijima, Bonin Islands. Journal of Volcanology and Geothermal Research, 29, 125–157.

Whattam, S.A., Shervais, J.W., Reagan, M.K., Coulthard JR, D.A., Pearce, J.A., Jones, P., Seo, J., Putirka, K., Chapman, T., Heaton, D., and others (2020) Mineral compositions and thermobarometry of basalts and boninites recovered during IODP Expedition 352 to the Bonin forearc. American Mineralogist.

Wyman, D.A. (1999) Paleoproterozoic boninites in an ophiolite-like setting, Trans-Hudson orogen, Canada. Geology, 27, 455–458.

CHAPTER IV:

4. SUMMARY AND CONCLUSIONS

Boninite lavas from the IBM arc system were part of the magmatic response to subduction initiation between the Pacific and Philippine tectonic plates (~52 Ma) (Reagan et al. 2019; Shervais et al. submitted). IBM boninite primary melts are sourced from a depleted harzburgite mantle source, which formed during the voluminous FAB volcanism, which preceded boninite volcanism (Reagan et al. 2015, 2017, 2019; Li et al. 2019; Pearce and Reagan 2019; Shervais et al. 2019, submitted). Shipboard and post-cruise observations from IODP Expedition 352 indicate that magma mixing may have occurred in boninite lavas (e.g., Reagan et al. 2015, 2017). LSB and HSB subgroups were distinguished by differences in their major and trace element chemistries, which previous studies have attributed to the changes in the amount of source depletion and added subduction component (Reagan et al. 2015, 2017; Pearce and Reagan 2019; Shervais et al. submitted). We hypothesize that boninite lavas recovered during IODP Expedition 352 (1) experienced multiple episodes of magma mixing prior to an eruption, and (2) these magma mixing events occurred within a composite magma chamber within the fore-arc crust. The goal of this work is to develop a model for the chemical evolution of boninite melts (from melt source to eruption) and to develop the first model of the magmatic architecture present during boninite volcanism in the IBM arc system.

Chapter II of this study presents photomicrographs of crystal textures in boninite lavas, major element chemistry of crystals, chemical transects of zoned crystals, and

single element maps of crystals. These data are combined with shipboard observations from Expedition 352 to reveal that magma mixing events effect boninite lavas at multiple points during their chemical evolution. These results are consistent with the hypothesis that magma mixing is a significant factor controlling the chemistry of boninite magmas (e.g., Umino 1986; Dobson et al. 2006; Pearce and Reagan 2019), occurring multiple times prior to eruption. The presence of olivine xenocrysts with zoned phenocrysts and lack of amphibole crystals indicate that the magma mixing events likely occur within a shallow magma chamber similar to that hypothesized by Umino (1986) and Dobson et al. (2006). Magmatic ascent and eruption cause the undercooling related zoning profiles, acicular pyroxene groundmass, and high-Ca pyroxene overgrowths (e.g., Lofgren et al. 1975; Grove and Bence 1977; Ohnenstetter and Brown 1991; Dobson et al. 2006; Crabtree and Lange 2010; Shea and Hamer 2013; Waters and Lange 2017). The data and interpretations presented in chapter II provide evidence for the presents of a magma chamber in which boninite melts crystallize and mixing prior to eruption. Further, the results of chapter II illustrate how integrating elemental maps and chemical transects of magmatic phenocrysts can be used to differentiate between undercooling and mixing related zoning patterns in cases where phenocrysts are effected by both processes.

Chapter III of this study presents major element chemistry of fresh glass, major element chemistry of melt inclusions within olivine and orthopyroxene phenocrysts, thermometry and barometry calculations on mineral and glass chemistries, and forward and reverse crystal fractionation models. Previous studies which attempt to model boninite crystal fractionation suggest that boninite and “boninite-like” melts can be

sourced from depleted lherzolite or harzburgite and crystallize Opx and Cpx (±olivne, source dependent) (i.e., Benard et al. 2016, 2017, 2018; Pearce and Reagan 2019; Shervais et al. submitted). Modeled crystallization paths from chapter III show that IBM boninites crystallize olivine and Opx with late forming Cpx, while melt composition evolves from boninite to HMA followed by andesite and dacite. Thermometry and barometry calculations produce temperatures of 1000-1200 ºC and pressures of ~3 kb. These results are consistent with those of Pearce and Reagan (2019) and Shervais et al. (submitted) and indicate that crystallization occurs at depths between 3 and 10 km at temperatures consistent with previous studies (e.g., Umino 1986; Crawford et al. 1989; Dobson et al. 2006; Lee et al. 2009, Whattam et al. 2020). Crystallization models from chapter III also indicate that boninite subgroups (i.e., LSB & HSB) have unique chemical evolution paths, which may be related to shut down in spreading and shift in the locus of volcanism as suggested by previous studies (e.g., Reagan et al. 2015, 2017, 2019; Shervais et al. submitted). Future major and trace elements (i.e., EPMA & LA-ICP-MS), isotopic (i.e., SIMS), and Laser Raman analysis on interstitial glass and melt inclusions will inform whether source migration or source evolution (i.e., chemical evolution) control the transition from LSB to HSB volcanism. The data and interpretations presented in chapter III provide evidence for a magmatic system in which crystallization begins at the base of the crust and continues until eruption. Further, the data and interpretations of chapter III indicate the magmatic system present during LSB volcanism is similar to those observed at mid-ocean ridge systems (e.g., Casey and Karson 1981; Sinton and Detrick 1992; Sours-Page et al. 2002; Rubin et al. 2009; Carbotte et al. 2013),

while HSB volcanism is likely more diffuse with less localized eruptions and fewer mixing events.

These integrated studies on crystal chemistry and the chemical evolution of boninite melts provide insight into the magmatic architecture and how it evolves with boninite volcanism. Together, these data document complex melt and crystal evolution histories, in a magmatic system similar to those observed at mid-ocean ridges. Melts containing zoned phenocrysts experience multiple magma mixing events with intermittent periods of undercooling, which results in rapid crystallization. Pyroxene overgrowths and groundmass primarily form during an eruption as devolatilization, ascending melts, and decreasing temperatures result in elevated pyroxene nucleation and crystal growth. Normal and reverse zoned olivine grains indicate that mixing events occur shortly before eruptions, possibly causing the eruption due to the destabilization of the magma chamber. Cumulate olivine grains (i.e., olivine xenocrysts) in the lavas reveal that magmas are interacting in a magma chamber, which contains a cumulate pile at its base. Cumulate olivine compositions and crystallization models indicate that the composition of the magma chamber is low-Mg boninite to HMA. Fractional crystallization models and the lack of amphibole crystallization show that the magma chamber exists at shallow depths (e.g., 3-6 km). Crystallization of the boninite melts begins at the base of the crust (i.e., 7-10 km) at temperatures of 1200-1300 ^{o}C. Crystallization continues as melts migrate through a crystal mush zone and into a magma chamber. The composite magma chamber (i.e., melt lens and crystal mush zone) exist at depths of 3-6 km at temperatures of 1000-1200 ^{o}C. The magmatic system during HSB

volcanism is likely similar in overall structure; however, lower melt production and a decrease in spreading rate result in less localized melt lens, which erupts off of the spreading axis.

Several outstanding questions remain regarding the melt source evolution as the magmatic system evolves from axial volcanism of LSB to the off-axis volcanism of HSB. Crystallization models indicate that these boninite subgroups follow slightly different major element evolution paths. Whole-rock chemistry (e.g., Reagan et al. 2015, 2017; Shervais et al. submitted) from recent studies indicate that the HSB melt likely contains more of a subduction component than LSB. While this does suggest that the input from the subducting slab does increase during the transition to HSB, it does not indicate whether the melt source (i.e., the peridotite from which melts are generated) remains the same and continues to deplete or migrates and beings to melt a new region of the mantle. Answering this question requires detailed trace element and isotopic analysis of the interstitial glass and crystal hosted melt inclusions in boninite lavas. Determining if the melt source migrated or continued to melt the same mantle peridotite will improve our understanding of mantle evolution as arc volcanism evolves from spreading centers to proto-arc volcanic systems where calc-alkaline volcanism begins (e.g., the Bonin Islands, Ishizuka et al. 2006; Reagan et al. 2019).

Crystal hosted melt inclusions observed in this work provide a unique window into the fluid chemistry of slab derived fluids during boninite volcanism, as many inclusions contain vapor bubbles. These vapor bubbles are currently the only known gas samples directly related to the IBM boninite lavas and will allow us to conduct the first direct

analysis based study of boninite gas and fluid chemistry. Determining the composition (major element and isotopic) of these vapor bubbles will allow us to improve our overall understanding of slab dehydration and its impact on early subduction volcanism. This will allow us to determine the source of fluids (i.e., what mineral source is breaking down and releasing the fluids), depth of the slab (i.e., depth at which the source mineral breaks down), and how this varies throughout the evolution of boninite volcanism. Further, this work will improve our overall understanding of melt production in the mantle and the change in slab input as the subduction system transitions to a proto-arc.

4.1. References

Bénard, A., Nebel, O., Ionov, D.A., Arculus, R.J., Shimizu, N., and Métrich, N. (2016) Primary silica-rich picrite and high-Ca boninite melt inclusions in pyroxenite veins from the Kamchatka sub-arc mantle. Journal of Petrology, 57, 1955–1982.

Bénard, A., Arculus, R.J., Nebel, O., Ionov, D.A., and McAlpine, S.R.B. (2017) Silica-enriched mantle sources of subalkaline picrite-boninite-andesite island arc magmas. Geochimica et Cosmochimica Acta, 199, 287–303.

Bénard, A., Le Losq, C., Nebel, O., and Arculus, R.J. (2018) Low-Ca boninite formation by second-stage melting of spinel harzburgite residues at mature subduction zones: new evidence from veined mantle xenoliths from the West Bismarck Arc. Contributions to Mineralogy and Petrology, 173, 105.

Carbotte, S.M., Marjanović, M., Carton, H., Mutter, J.C., Canales, J.P., Nedimović, M.R., Han, S., and Perfit, M.R. (2013) Fine-scale segmentation of the crustal magma reservoir beneath the East Pacific Rise. Nature Geoscience, 6, 866.

Casey, J.F., and Karson, J.A. (1981) Magma chamber profiles from the Bay of Islands ophiolite complex. Nature, 292, 295–301.

Crabtree, S.M., and Lange, R.A. (2010) Complex Phenocryst Textures and Zoning Patterns in Andesites and Dacites: Evidence of Degassing-Induced Rapid Crystallization? Journal of Petrology, 52, 3–38.

Crawford, A.J., Falloon, T.J., and Green, D.H. (1989) Classification, petrogenesis and tectonic setting of boninites.

Dobson, P.F., Blank, J.G., Maruyama, S., and Liou, J.G. (2006) Petrology and geochemistry of boninite-series volcanic rocks, Chichi-Jima, Bonin Islands, Japan. International Geology Review, 48, 669–701.

Grove, T.L., and Bence, A.E. (1977) Experimental study of pyroxene-liquid interaction in quartz-normative basalt 15597. In Lunar and Planetary Science Conference Proceedings Vol. 8, pp. 1549–1579.

Ishizuka, O., Kimura, J.-I., Li, Y.B., Stern, R.J., Reagan, M.K., Taylor, R.N., Ohara, Y., Bloomer, S.H., Ishii, T., Hargrove, U.S., and others (2006) Early stages in the evolution of Izu–Bonin arc volcanism: New age, chemical, and isotopic constraints. Earth and Planetary Science Letters, 250, 385–401.

Lee, C.-T.A., Luffi, P., Plank, T., Dalton, H., and Leeman, W.P. (2009) Constraints on the depths and temperatures of basaltic magma generation on Earth and other terrestrial

planets using new thermobarometers for mafic magmas. Earth and Planetary Science Letters, 279, 20–33.

Lofgren, G.E., Donaldson, C.H., and Usselman, T.M. (1975) Geology, petrology, and crystallization of Apollo 15 quartz-normative basalts. In Lunar and Planetary Science Conference Proceedings Vol. 6, pp. 79–99.

Ohnenstetter, D., and Brown, W.L. (1992) Overgrowth Textures, Disequilibrium Zoning, and Cooling History of a Glassy Four-Pyroxene Boninite Dyke from New Caledonia. Journal of Petrology, 33, 231–271.

Reagan, M.K., Pearce, J.A., Petronotis, K., and Expedition 352 Scientists (2015) Expedition 352 summary. Proceedings of the International Ocean Discovery Program, 352, 1–32.

Reagan, M.K., Pearce, J.A., Petronotis, K., Almeev, R.R., Avery, A.J., Carvallo, C., Chapman, T., Christeson, G.L., Ferré, E.C., Godard, M., and others (2017) Subduction initiation and ophiolite crust: new insights from IODP drilling. International Geology Review, 59, 1439–1450.

Reagan, M.K., Heaton, D.E., Schmitz, M.D., Pearce, J.A., Shervais, J.W., and Koppers, A.A.P. (2019) Forearc ages reveal extensive short-lived and rapid seafloor spreading following subduction initiation. Earth and Planetary Science Letters, 506, 520–529.

Rubin, K.H., Sinton, J.M., Maclennan, J., and Hellebrand, E. (2009) Magmatic filtering of mantle compositions at mid-ocean-ridge volcanoes. Nature Geoscience, 2, 321.

Shea, T., and Hammer, J.E. (2013) Kinetics of cooling- and decompression-induced crystallization in hydrous mafic-intermediate magmas. Journal of Volcanology and Geothermal Research, 260, 127–145.

Shervais, J.W., Reagan, M., Godard, M., Prytulak, J., Ryan, J.G., Pearce, J.A., Almeev, R.R., Li, H., Haugen, E., Chapman, T., and others (Submitted) Magmatic Response to Subduction Initiation, Part II: Boninites and related rocks of the Izu-Bonin Arc from IODP Expedition 352. Geochemistry, Geophysics, Geosystems.

Sours-Page, R., Nielsen, R.L., and Batiza, R. (2002) Melt inclusions as indicators of parental magma diversity on the northern East Pacific Rise. Melt Inclusions at the Millennium: Toward a Deeper Understanding of Magmatic Processes, 183, 237–261.

Umino, S. (1986) Magma mixing in boninite sequence of Chichijima, Bonin Islands. Journal of Volcanology and Geothermal Research, 29, 125–157.

Waters, L.E., and Lange, R.A. (2017) An experimental study of (Fe-Mg) KD between orthopyroxene and rhyolite: a strong dependence on H2O in the melt. Contributions to Mineralogy and Petrology, 172, 42.

Whattam, S.A., Shervais, J.W., Reagan, M.K., Coulthard JR, D.A., Pearce, J.A., Jones, P., Seo, J., Putirka, K., Chapman, T., Heaton, D., and others (2020) Mineral compositions and thermobarometry of basalts and boninites recovered during IODP Expedition 352 to the Bonin forearc. American Mineralogist.

APPENDICES

APPENDIX A: SUPPLEMENTAL MATERIAL TO CHAPTER II

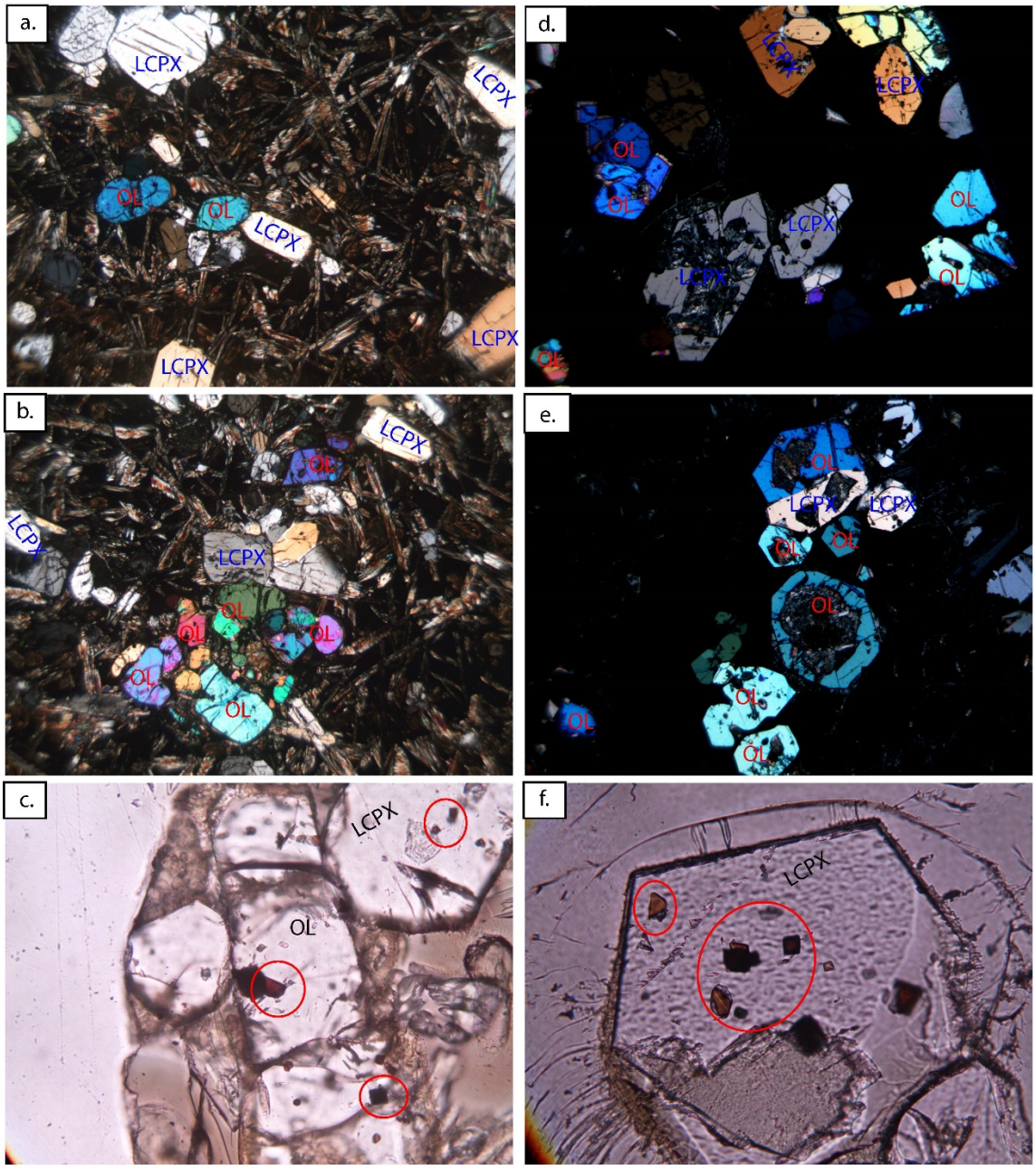

Figure A.1
Photomicrographs of typical boninite crystal assemblages. Photomicrographs (a.), (b.), and (f.) are from sample U1439A-21X1 2-3, (c.), (d.), and (f.) are from sample U1439C-28R2W 71-73. Sample U1439A-21X1 2-3 is an example of a highly crystalline boninite lava, while sample U1439C-28R2W 71-73 is an example of a glass rich boninite lava. OL= Olivine, LCPX= Low Ca Pyroxene. Red circles in (c.) and (f.) highlight Cr spinel grains in crystals from both samples.

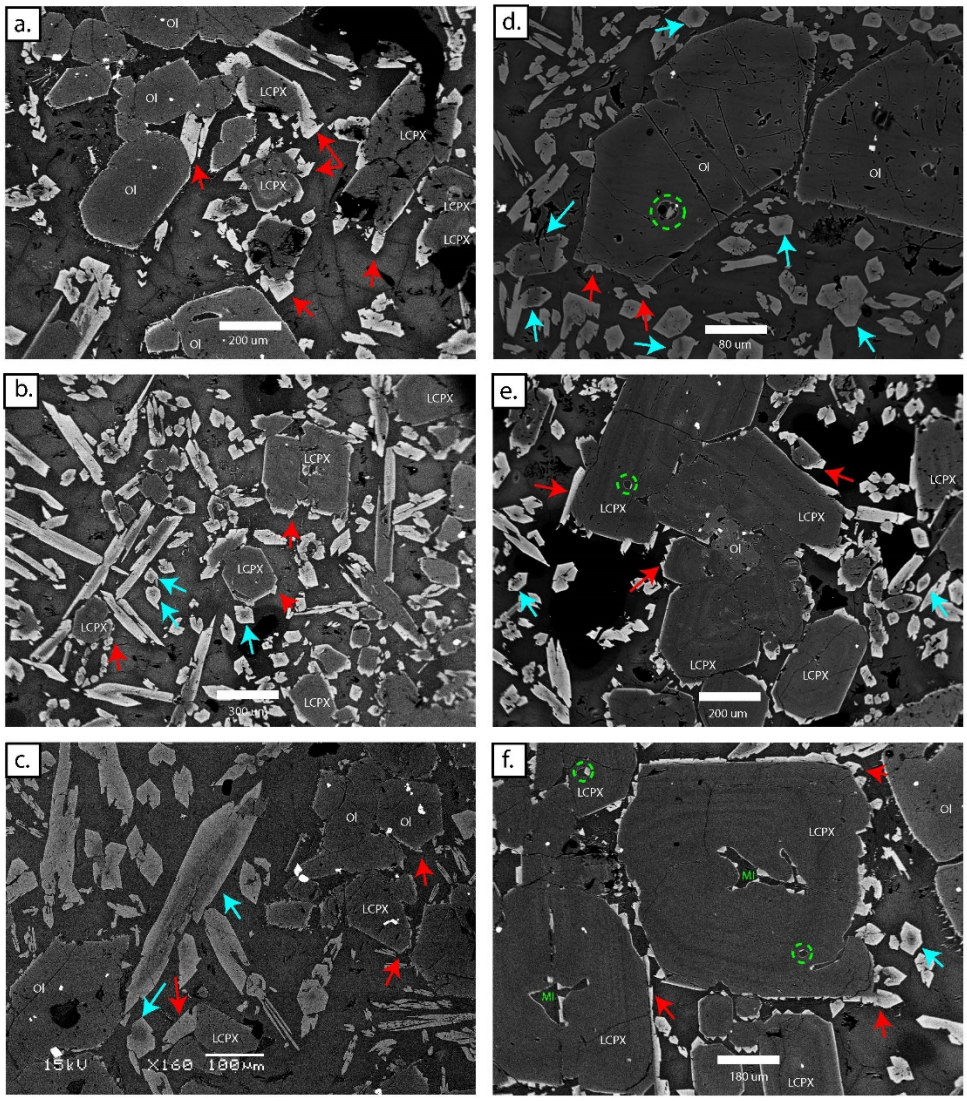

Figure A.2
BSE images of anomalous textures from the four samples, which are the focus of this study (samples U1439C-2R3W 2-3, U1439C-15R1W 8-10, U1439C-19R2W 46-48, and U1439C-25R2W 18-19). Images (b.) and (f.) from sample (2R3), (a.) and (e.) from sample (15R1), (c.) from sample (19R2), and (d.) from sample (25R2). White scale bar can be seen in the bottom center of each image. LCPX= Low Ca Pyroxene, Ol= Olivine. Red arrows in the images point to clinopyroxene overgrowths (in most cases, augite and anomalous Al-rich end-members), which nucleate off of olivine and low-Ca pyroxenes. Blue arrows point to groundmass pyroxenes that exhibit anomalous overgrowth and zoning textures (some exhibit oscillatory, normal, or reverse zoning). Green dashed circles in images (d.), (e.), and (f.) highlight melt inclusion in the phenocrysts. The green MI label in image (f.) is also meant to highlight larger melt inclusions, which are in zoned crystals.

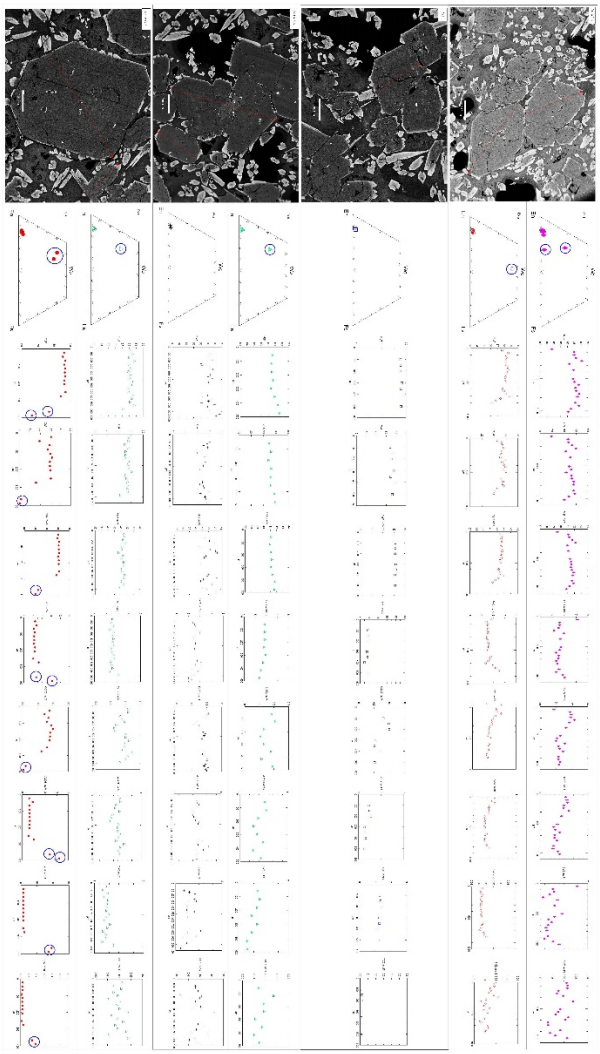

Figure A.3
Pyroxene chemical traverses from samples 2R3, 15R1, and 25R2. Labels (Px #) in the top left corner of each BSE image refers to the label used in (Supplemental Table 3.) to identify the individual pyroxene grains. A white scale bar can be found in the bottom center of each BSE. The red arrows in each BSE indicate the direction and length of the given chemical traverse (0 µm at the blunt end of the arrow and increasing in value towards the arrow). For BSE images with more than one chemical traverse, the labels (Px #) are also placed directly on the individual crystals analyzed in white. For these BSE images, the labels are also found to the top left of the pyroxene quadrilateral associated with each grain. Pyroxenes overgrowths and pyroxenes within melt inclusions are circled in blue on the pyroxene quadrilateral and on some elemental traverses (they were removed in some elemental traverses because they made it difficult to see chemical variation within low-Ca pyroxene cores). (Px 1) and (Px 2) are also referred to in (Figures. 4 and 6) within the paper. (Px 14) is referred to in (Figure 2.8) within the paper.

Figure A.3. continues

Figure A.3. continues

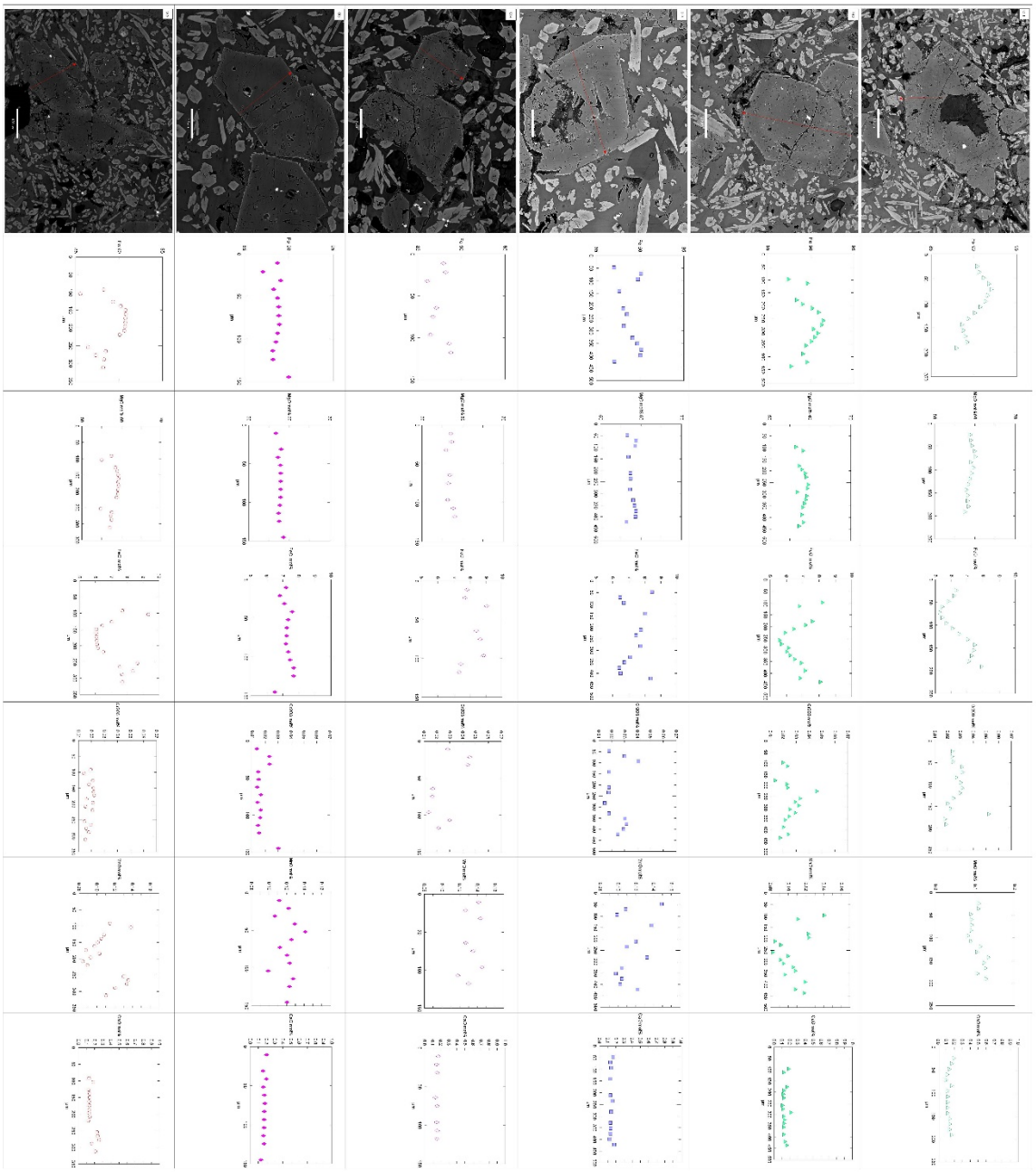

Figure A.4
Olivine chemical traverses from sample 25R2. Labels (Ol #) in the top left corner of each BSE image refers to the label used in (Table A.5.) to identify the individual olivine grains. A white scale bar can be found in the bottom center of each BSE. The red arrows in each BSE indicate the direction and length of the given chemical traverse (0 µm at the blunt end of the arrow and increasing in value towards the arrow). (Ol 1) is also referred to in (Figure 2.5) within the paper. (Ol 4) is referred to in (Figure A.5).

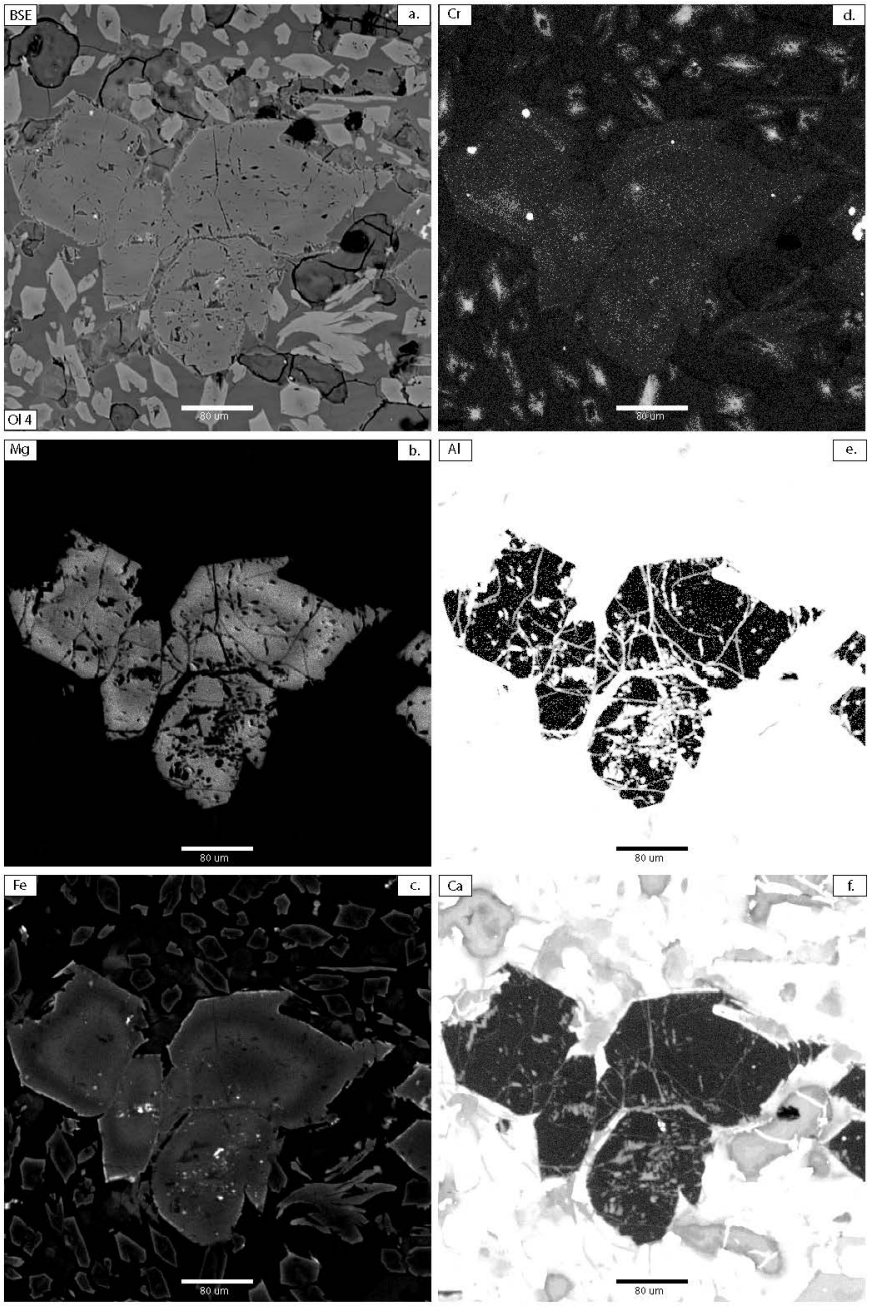

Figure A.5
Elemental maps of zoned olivine phenocrysts from sample 25R2. Label (Ol 4) in the bottom left-hand corner of BSE image (a.) refers to the label used in (Table A.5) and (Figure A.4) to identify the individual olivine grains. BSE image (a.) and elemental maps (b.), (c.), (d.), (e.), and (f.) were produced using EPMA. Bright coloration in the elemental maps indicates enrichment in a given element, while darker coloration indicates depletion.

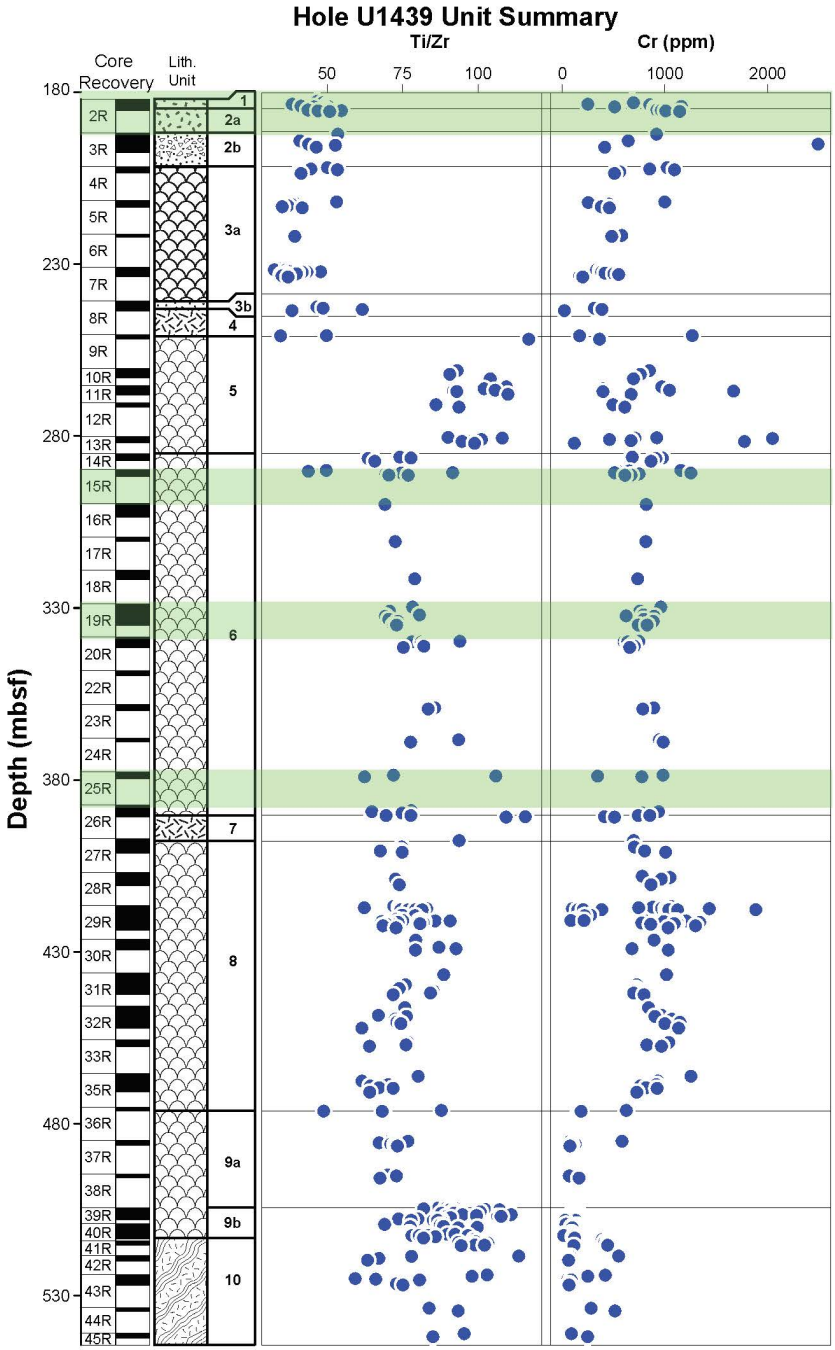

Figure A.6
Correlating samples with zones of high chemical variability within the core. The green lines cutting across the graphs indicate the location of the samples from this study within the core. Ti/Zr and Cr parts per million (ppm) are plotted in correlation to the given samples stratigraphic position. The correlation between samples from this study and zones of high chemical variability in the core is likely due to the open system magmatic processes that effected the lavas upon ascent. Modified after Ryan et al. (2017).

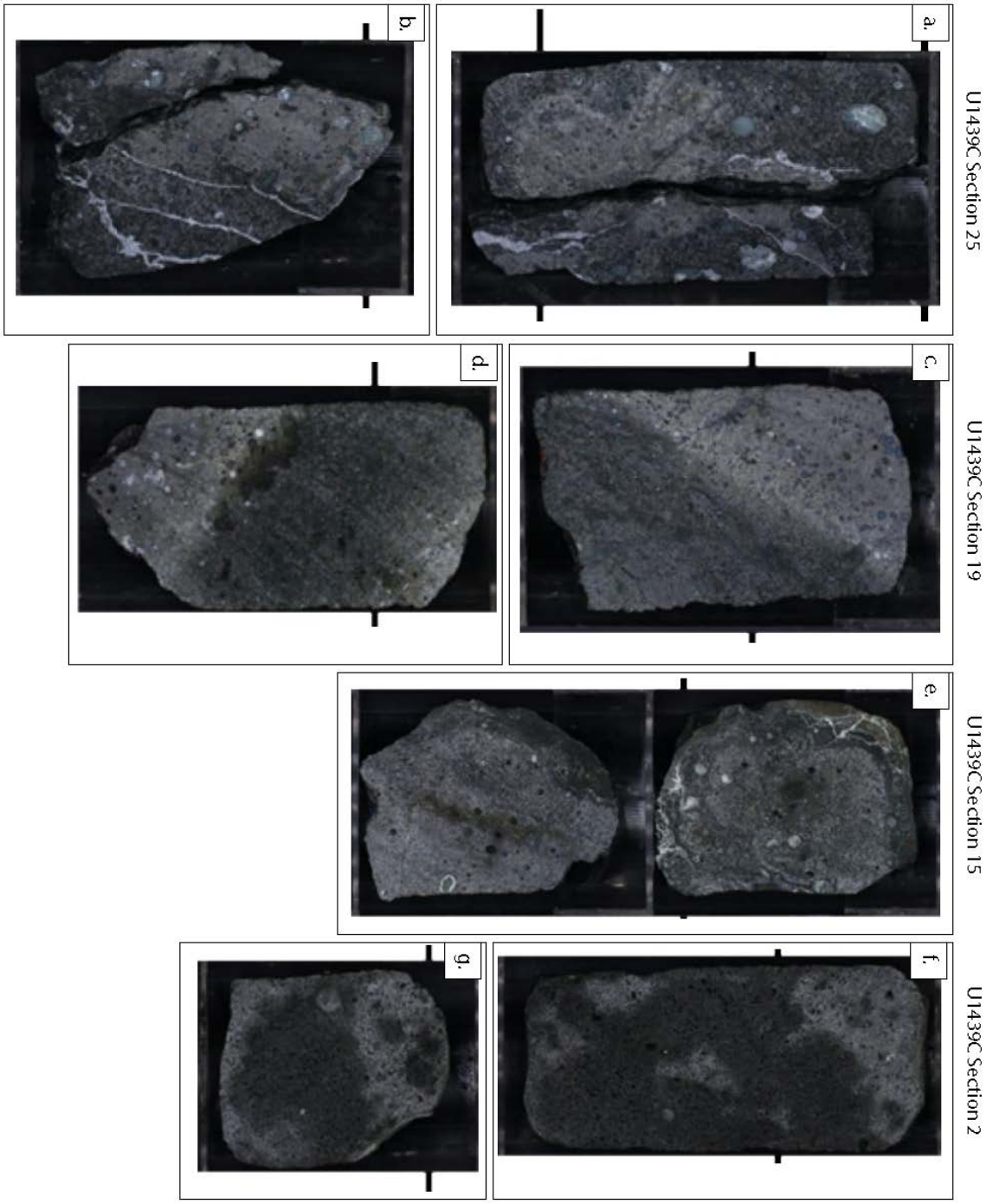

Figure A.7
Magma mingling textures observed in core U1439C from IODP expedition 352. Textures in this figure were all observed in sections of the core, which also correlate to the samples which exhibit anomalous zoning in this study (as indicated by the labels above each set of image).

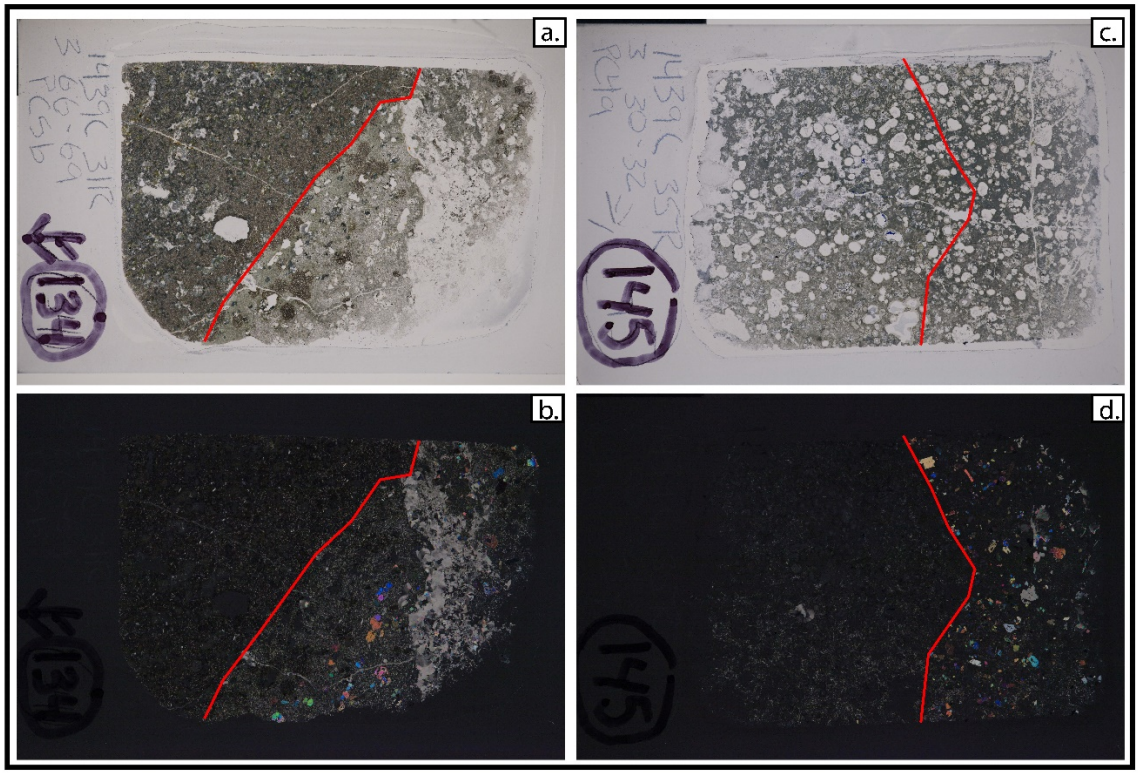

Figure A.8
Mixing textures in boninite lavas at thin-section scale. Full thin section photomicrographs of samples U1439C-31R-3 66-69 (a. & b.) and U1439C-35R-3 (c. & d.). Photomicrographs (a.) and (c.) were captured using plane-polarized light (PPL), while (b.) and (d.) were capture with cross-polarized light (XPL). Red lines across the samples represent the interface between the interacting lavas. On the left side of both samples, aphyric lavas which contain groundmass Cpx can be seen while the right side of the samples contain lavas with olivine and Opx phenocryst and Cpx rich groundmass. Images can be found in the IODP Expedition 352 proceedings with the preliminary expedition report (i.e., Expedition 352 scientist 2014 and Reagan et al. (2015).

Table A.1. Microprobe Standards

Mineral Standards																		
Standards	Intrusment	SiO2 (wt%)	TiO2 (wt%)	Al2O3 (wt%)	Cr2O3 (wt%)	FeO (wt%)	MgO (wt%)	MnO (wt%)	NiO (wt%)	CaO (wt%)	SrO (wt%)	BaO (wt%)	Na2O (wt%)	K2O (wt%)	P2O5 (wt%)	H2O (wt%)
Olivine #AS200-AB	JEOL	41.16	-	-	-	7.62	50.78	0.10	0.29	-	-	-	-	-	-	-
Plag An 65 #AS1280-AB	JEOL	52.41	0.07	25.83	-	0.37	0.13	-	-	11.80	0.08	0.01	4.35	0.41	-	-
Cr-Diopside #AS1120-AB	JEOL	54.60	0.10	-	0.50	1.39	17.15	-	-	25.51	-	-	0.44	-	-	-
Diopside #AS5130-AB	JEOL	54.98	-	-	-	1.88	17.10	0.22	-	25.66	-	-	0.40	-	-	-
Sanidine	JEOL	64.67	-	18.76	-	0.18	-	-	-	-	-	1.09	3.01	12.11	-	-
Kaersutite #AS1200-AB	JEOL	40.09	5.04	12.36	-	12.24	12.55	0.18	-	11.56	-	-	2.44	1.17	-	1.97
Chromite, Tobacco Root Mtn. USA	JEOL	-	0.99	20.52	40.81	29.40	8.29	-	-	-	-	-	-	-	-	-
Augite, Dumfries-shire, UK	JEOL	45.95	1.45	7.44	-	7.68	14.27	-	-	23.21	-	-	-	-	-	-
Ilmenite, Lac St Jean, Quebec	JEOL	-	46.70	-	-	49.77	3.53	-	-	-	-	-	-	-	-	-
Fayalite, Loch Fyne Argyll & Bute, Scotland	JEOL	30.12	-	-	-	66.48	3.40	-	-	-	-	-	-	-	-	-
San Carlos Olivine	Cameca	40.81	-	-	-	9.55	49.42	0.14	0.37	0.05	-	-	-	-	-	-
Chromite	Cameca	-	-	9.92	60.50	13.04	15.20	0.11	-	-	-	-	-	-	-	-
Anorthite	Cameca	44.00	0.03	36.03	-	0.62	0.02	-	-	19.09	-	-	0.53	0.03	-	-
Diopside	Cameca	55.81	-	0.11	-	0.25	17.79	0.04	-	25.28	-	-	0.25	-	-	-
Synthetic Tephroite	Cameca	29.75	-	-	-	-	-	70.25	-	-	-	-	-	-	-	-
Synthetic Fayalite	Cameca	29.49	-	-	-	70.51	-	-	-	-	-	-	-	-	-	-
Synthetic Rutile	Cameca	-	100.00	-	-	-	-	-	-	-	-	-	-	-	-	-
Amelia Albite	Cameca	68.14	-	19.76	-	-	-	-	-	0.40	-	-	11.46	0.20	-	-
Glass Standards																
USGS BHVO1	JEOL	49.90	2.73	13.50	-	11.07	7.23	-	-	11.40	-	-	2.22	0.52	0.27	-
Rhyolitic glass USNM 72854 VG-568	JEOL	76.71	0.12	12.06	-	1.23	-	0.03	-	0.50	-	-	3.75	4.89	-	0.12
Obsidian #AS1250-AB	JEOL	73.94	0.10	13.11	-	1.72	0.07	0.06	-	0.76	-	-	4.06	5.04	-	0.80
Basaltic Glass NMNH 111240-52 VG-2	Cameca	50.81	1.85	14.06	-	12.06	6.95	0.22	-	11.12	-	-	2.62	0.19	0.20	0.02

Table A.2. LA-ICP-TOF-MS Operating Conditions

Laser Ablation Operating Conditions	
Laser Type	Analyte G2
Spot Size	5µm
Repetition Rate	100 Hz
Sample Gas (He)	0.34 LPM
Ablation Mode	Raster
Fluence	3 Jcm^{-2}
Dosage	1 (edge-to-edge ablation)
ICP-TOF Operating Conditions	
Plasma Power	1380W
Sampling Depth	4.6 mm
Nebulizer Gas Flow (Ar)	0.85 LPM
m/Q attenuated	28, 30, 40, 80
TOF extraction time	46 µs
Number of integrated TOF extractions	726
Datapoint per laser pulse	1 mass spectrum
Aerosol wash-in delay	100 ms

Table A.3. Zoned Pyroxene Transects

Sample	Grain Label	SiO2 (wt%)	TiO2 (wt%)	Al2O3 (wt%)	Cr2O3 (wt%)	FeO (wt%)	MgO (wt%)	MnO (wt%)	CaO (wt%)	Na2O (wt%)	K2O (wt%)	Total (wt%)	Jade	CaTiTs	CaCrTs	CaTs	Wo	En	Fs	Mg#	Cr#	µm
15R1	Px 1	57.07	0.03	1.01	0.24	9.56	29.80	0.22	1.87	0.04	0.02	99.86	0.15	0.04	0.34	0.76	3.55	78.49	14.13	84.75	19.41	46.24
15R1	Px 1	58.76	0.04	1.09	0.54	7.73	31.75	0.18	1.37	0.06	0.01	101.54	0.22	0.05	0.74	0.59	2.53	81.56	11.15	87.98	33.19	92.49
15R1	Px 1	57.87	0.03	1.11	0.56	7.66	31.47	0.17	1.38	0.05	0.00	100.29	0.15	0.05	0.77	0.63	2.57	81.82	11.17	87.98	33.65	138.73
15R1	Px 1	58.06	0.02	0.95	0.55	7.58	31.98	0.17	1.29	0.02	0.00	100.63	0.07	0.03	0.76	0.53	2.39	82.76	11.00	88.27	36.67	184.98
15R1	Px 1	58.43	0.02	0.95	0.63	7.09	32.56	0.17	1.15	0.02	0.01	101.01	0.05	0.03	0.85	0.48	2.12	83.73	10.23	89.11	39.77	231.22
15R1	Px 1	57.78	0.03	1.15	0.53	8.13	31.29	0.16	1.45	0.03	0.00	100.55	0.11	0.04	0.73	0.72	2.71	81.28	11.84	87.28	31.47	277.47
15R1	Px 1	58.32	0.04	0.86	0.47	7.73	31.50	0.19	1.39	0.03	0.01	100.54	0.10	0.05	0.64	0.46	2.60	81.75	11.26	87.90	35.16	369.95
15R1	Px 1	53.11	0.18	3.31	0.21	9.40	20.47	0.23	12.60	0.11	0.02	99.64	0.38	0.25	0.31	2.97	24.64	55.68	14.34	79.52	6.04	416.20
15R1	Px 1	57.72	0.03	0.69	0.36	7.80	31.52	0.18	1.55	0.03	0.01	99.88	0.09	0.03	0.50	0.38	2.91	82.28	11.42	87.81	34.37	508.69
15R1	Px 1	58.66	0.02	0.55	0.31	7.76	32.03	0.18	1.41	0.03	0.00	100.95	0.11	0.03	0.42	0.27	2.61	82.65	11.23	88.04	35.80	554.93
15R1	Px 1	58.08	0.02	0.61	0.28	7.19	31.53	0.17	1.25	0.06	0.06	99.25	0.22	0.03	0.39	0.30	2.35	82.67	10.57	88.66	31.70	601.17
15R1	Px 1	58.64	0.04	0.79	0.45	7.64	32.02	0.17	1.34	0.01	0.00	101.08	0.02	0.05	0.61	0.44	2.48	82.53	11.04	88.20	36.15	647.42
15R1	Px 1	58.78	0.03	0.59	0.33	7.58	32.12	0.18	1.26	0.00	0.00	100.87	0.01	0.04	0.45	0.32	2.34	82.92	10.98	88.31	36.18	693.66
15R1	Px 1	58.55	0.01	0.58	0.35	7.31	32.25	0.17	1.21	0.02	0.00	100.47	0.08	0.01	0.49	0.30	2.25	83.46	10.61	88.72	37.88	739.91
15R1	Px 1	58.56	0.01	0.68	0.42	7.47	32.18	0.16	1.23	0.02	0.00	100.73	0.07	0.01	0.57	0.36	2.28	83.12	10.82	88.48	37.81	786.15
15R1	Px 1	58.72	0.03	0.55	0.33	7.67	32.13	0.17	1.25	0.02	0.01	100.87	0.07	0.03	0.46	0.26	2.32	82.94	11.10	88.20	37.83	878.64
15R1	Px 1	58.89	0.01	0.52	0.33	7.35	32.35	0.17	1.18	0.04	0.01	100.86	0.14	0.02	0.46	0.22	2.18	83.39	10.64	88.69	38.85	924.88
15R1	Px 1	58.52	0.02	0.71	0.37	8.08	31.83	0.21	1.37	0.03	0.00	101.14	0.09	0.03	0.50	0.41	2.54	82.11	11.70	87.53	33.85	971.13
15R1	Px 1	58.28	0.03	0.78	0.34	8.26	31.29	0.18	1.50	0.02	0.01	100.68	0.05	0.05	0.47	0.50	2.79	81.24	12.04	87.10	30.15	1017.37
15R1	Px 1	53.28	0.08	4.15	0.03	17.01	23.39	0.30	2.08	0.18	0.03	100.51	0.63	0.11	0.04	4.00	4.04	63.28	25.82	71.02	0.66	1063.62
15R1	Px 2	58.13	0.03	0.96	0.47	8.02	31.86	0.18	1.37	0.03	0.01	101.05	0.09	0.04	0.64	0.57	2.55	82.21	11.61	87.63	33.00	35.21
15R1	Px 2	58.26	0.03	0.86	0.49	7.38	31.93	0.17	1.24	0.02	0.02	100.39	0.08	0.04	0.67	0.47	2.32	82.80	10.73	88.53	36.36	70.42
15R1	Px 2	58.30	0.02	0.97	0.57	7.60	32.00	0.16	1.29	0.02	0.00	100.93	0.08	0.03	0.78	0.52	2.39	82.59	11.00	88.25	37.10	105.64
15R1	Px 2	58.54	0.02	0.74	0.45	7.60	32.14	0.18	1.37	0.01	0.00	101.05	0.04	0.03	0.62	0.39	2.53	82.83	10.99	88.29	38.09	140.85
15R1	Px 2	58.48	0.02	0.71	0.41	7.61	32.05	0.18	1.32	0.03	0.01	100.82	0.10	0.03	0.56	0.37	2.44	82.78	11.02	88.25	36.59	176.06
15R1	Px 2	58.67	0.03	0.69	0.39	7.60	31.96	0.17	1.28	0.02	0.01	100.81	0.06	0.04	0.54	0.36	2.37	82.60	11.02	88.23	36.48	211.27
15R1	Px 2	58.74	0.03	0.71	0.40	7.64	32.18	0.17	1.31	0.00	0.00	101.18	0.01	0.04	0.54	0.40	2.41	82.84	11.04	88.24	35.83	246.49
15R1	Px 2	58.57	0.02	0.70	0.38	7.49	32.24	0.17	1.29	0.02	0.01	100.89	0.07	0.02	0.52	0.40	2.40	83.13	10.83	88.47	35.25	281.70
15R1	Px 2	58.67	0.01	0.53	0.34	7.43	32.08	0.19	1.25	0.01	0.01	100.51	0.03	0.01	0.47	0.28	2.32	83.08	10.79	88.50	39.29	316.91
15R1	Px 2	58.77	0.02	0.55	0.32	7.59	32.14	0.18	1.26	0.02	0.00	100.85	0.07	0.02	0.44	0.29	2.35	82.98	10.99	88.30	36.71	352.12
15R1	Px 2	58.68	0.01	0.52	0.32	7.62	31.98	0.22	1.26	0.02	0.01	100.64	0.06	0.02	0.44	0.26	2.35	82.77	11.07	88.21	38.27	387.34
15R1	Px 2	58.58	0.02	0.52	0.34	7.69	32.04	0.19	1.32	0.01	0.01	100.71	0.03	0.03	0.47	0.26	2.46	82.87	11.15	88.14	39.52	422.55
15R1	Px 2	58.24	0.01	0.50	0.30	7.64	31.58	0.17	1.29	0.06	0.02	99.81	0.19	0.02	0.42	0.19	2.43	82.46	11.18	88.06	37.88	457.76
15R1	Px 2	58.65	0.02	0.52	0.35	7.58	31.91	0.19	1.32	0.00	0.00	100.54	0.01	0.02	0.48	0.27	2.45	82.69	11.02	88.24	39.98	492.97
15R1	Px 2	48.30	0.50	12.27	0.06	12.03	8.22	0.21	16.26	0.71	0.16	98.72	2.62	0.71	0.10	11.74	33.30	23.41	19.23	54.90	0.51	528.19
15R1	Px 2	58.34	0.01	0.60	0.33	7.89	31.53	0.18	1.38	0.01	0.00	100.28	0.04	0.02	0.45	0.35	2.59	82.05	11.51	87.69	35.53	598.61
15R1	Px 2	58.61	0.01	0.53	0.32	7.75	31.59	0.18	1.32	0.02	0.01	100.35	0.08	0.01	0.44	0.27	2.47	82.12	11.30	87.90	37.56	633.82
15R1	Px 2	58.54	0.01	0.54	0.32	7.57	31.69	0.19	1.29	0.01	0.00	100.16	0.03	0.01	0.44	0.31	2.41	82.48	11.05	88.18	37.09	669.03
15R1	Px 2	58.71	0.02	0.51	0.32	7.31	32.20	0.15	1.16	0.02	0.00	100.40	0.06	0.03	0.44	0.25	2.17	83.41	10.62	88.70	38.40	704.25
15R1	Px 2	58.62	0.02	0.58	0.29	8.19	31.78	0.19	1.43	0.02	0.00	101.12	0.08	0.03	0.39	0.33	2.66	82.03	11.85	87.38	32.98	739.46
15R1	Px 2	58.31	0.02	0.59	0.26	8.50	31.18	0.18	1.52	0.06	0.01	100.64	0.20	0.02	0.36	0.31	2.85	81.02	12.40	86.73	30.43	774.67
15R1	Px 2	58.17	0.01	0.69	0.29	8.85	30.87	0.21	1.69	0.03	0.01	100.83	0.09	0.02	0.41	0.44	3.16	80.25	12.90	86.15	29.92	809.88

Table A.3. continues

Sample	Grain Label	SiO2 (wt%)	TiO2 (wt%)	Al2O3 (wt%)	Cr2O3 (wt%)	FeO (wt%)	MgO (wt%)	MnO (wt%)	CaO (wt%)	Na2O (wt%)	K2O (wt%)	Total (wt%)	Jade	CaTiTs	CaCrTs	CaTs	Wo	En	Fs	Mg#	Cr#	µm
15R1	Px 3	58.19	0.01	0.90	0.47	7.89	31.63	0.17	1.36	0.02	0.01	100.65	0.06	0.02	0.64	0.56	2.54	81.98	11.48	87.72	34.11	100.70
15R1	Px 3	57.86	0.04	0.97	0.56	7.73	31.26	0.18	1.41	0.03	0.00	100.05	0.10	0.05	0.78	0.51	2.64	81.55	11.32	87.81	36.80	151.05
15R1	Px 3	58.04	0.03	1.06	0.58	7.94	31.31	0.20	1.49	0.03	0.01	100.69	0.11	0.04	0.79	0.59	2.79	81.23	11.56	87.55	35.33	201.40
15R1	Px 3	59.05	0.02	0.54	0.33	7.69	32.35	0.18	1.37	0.03	0.01	101.56	0.09	0.03	0.45	0.25	2.53	82.93	11.06	88.24	38.04	302.09
15R1	Px 3	58.84	0.02	0.56	0.30	7.85	32.13	0.16	1.36	0.01	0.00	101.23	0.03	0.02	0.40	0.33	2.52	82.71	11.34	87.95	34.62	352.44
15R1	Px 3	55.76	0.03	0.60	0.39	6.64	30.59	0.17	1.11	1.48	1.69	98.44	5.02	0.03	0.54	-2.20	2.08	79.79	9.71	89.15	39.41	402.79
15R1	Px 3	57.66	0.02	0.53	0.30	7.67	31.12	0.19	1.40	0.41	0.56	99.87	1.39	0.02	0.41	-0.38	2.63	81.02	11.20	87.86	36.17	503.49
15R1	Px 4	57.98	0.02	1.00	0.53	7.95	31.43	0.19	1.46	0.02	0.01	100.59	0.07	0.03	0.72	0.60	2.73	81.58	11.58	87.57	34.46	59.46
15R1	Px 4	57.75	0.04	1.06	0.60	7.96	31.13	0.18	1.50	0.03	0.03	100.29	0.10	0.05	0.83	0.57	2.81	81.11	11.64	87.45	36.03	118.92
15R1	Px 4	58.18	0.03	0.73	0.38	7.98	31.42	0.19	1.45	0.03	0.00	100.38	0.09	0.04	0.52	0.41	2.71	81.72	11.64	87.53	33.95	178.38
15R1	Px 4	58.64	0.03	0.55	0.31	7.93	31.73	0.22	1.34	0.02	0.01	100.78	0.06	0.04	0.43	0.28	2.50	82.15	11.52	87.70	36.16	237.83
15R1	Px 4	58.41	0.02	0.68	0.38	8.15	31.60	0.19	1.46	0.02	0.01	100.92	0.06	0.02	0.52	0.39	2.72	81.77	11.83	87.36	35.54	297.29
15R1	Px 4	58.22	0.03	0.94	0.52	7.79	31.66	0.18	1.34	0.01	0.00	100.68	0.02	0.03	0.71	0.56	2.50	82.03	11.33	87.87	35.50	356.75
15R1	Px 4	58.30	0.01	0.53	0.33	7.50	31.92	0.20	1.24	0.01	0.00	100.04	0.04	0.02	0.45	0.28	2.32	83.07	10.95	88.35	38.44	416.21
15R1	Px 4	58.28	0.02	0.85	0.55	7.34	31.95	0.18	1.24	0.00	0.01	100.44	0.01	0.03	0.76	0.46	2.31	82.82	10.68	88.58	39.16	475.67
15R1	Px 4	52.62	0.17	4.12	0.08	9.07	17.88	0.20	14.96	0.11	0.01	99.21	0.39	0.23	0.12	4.00	29.60	49.20	14.00	77.85	2.02	535.13
15R1	Px 5	58.35	0.02	0.93	0.62	7.36	31.78	0.20	1.26	0.03	0.00	100.55	0.09	0.03	0.85	0.45	2.35	82.35	10.71	88.50	39.88	115.09
15R1	Px 5	56.85	0.02	0.93	0.57	7.39	30.86	0.15	1.35	0.05	0.05	98.22	0.17	0.03	0.80	0.46	2.57	81.90	11.01	88.15	37.85	143.86
15R1	Px 5	57.43	0.03	1.04	0.56	7.73	32.50	0.15	1.52	0.03	0.02	101.00	0.12	0.04	0.76	0.58	2.81	83.63	11.16	88.23	35.01	172.64
15R1	Px 5	56.37	0.03	0.97	0.60	7.48	32.78	0.18	1.39	0.04	0.02	99.85	0.12	0.04	0.82	0.48	2.60	85.09	10.89	88.65	38.26	201.41
15R1	Px 5	58.25	0.00	0.76	0.38	8.18	30.88	0.18	1.49	0.01	0.01	100.16	0.04	0.01	0.53	0.49	2.80	80.69	11.99	87.06	33.54	258.96
15R1	Px 5	58.20	0.03	0.79	0.34	8.21	31.36	0.19	1.55	0.16	0.13	100.96	0.55	0.04	0.46	0.26	2.87	81.07	11.90	87.20	29.88	287.73
15R1	Px 5	57.96	0.03	0.72	0.43	7.69	32.73	0.20	1.39	0.02	0.00	101.19	0.08	0.04	0.59	0.36	2.57	84.05	11.08	88.35	37.44	316.50
15R1	Px 5	56.79	0.03	0.78	0.44	7.54	33.17	0.17	1.30	0.02	0.01	100.24	0.07	0.04	0.60	0.43	2.41	85.69	10.93	88.69	35.95	345.28
15R1	Px 5	55.42	0.02	0.80	0.46	7.38	32.76	0.17	1.31	0.02	0.01	98.34	0.06	0.03	0.64	0.45	2.48	86.18	10.89	88.79	36.60	374.05
15R1	Px 5	58.51	0.03	0.89	0.51	7.56	32.05	0.17	1.33	0.02	0.01	101.07	0.05	0.03	0.70	0.49	2.46	82.60	10.93	88.31	36.63	431.59
15R1	Px 5	56.23	0.03	1.01	0.54	7.58	31.30	0.17	1.48	0.66	0.77	99.78	2.22	0.04	0.75	-0.49	2.77	81.24	11.03	88.04	34.98	460.37
15R1	Px 5	56.79	0.02	0.99	0.53	7.50	32.80	0.19	1.32	0.03	0.01	100.18	0.11	0.03	0.72	0.57	2.45	84.88	10.90	88.62	34.73	489.14
15R1	Px 5	57.21	0.05	1.01	0.48	7.37	30.50	0.16	1.31	0.13	0.12	98.35	0.45	0.06	0.67	0.44	2.49	80.91	10.97	88.06	32.09	546.69
15R1	Px 5	57.53	0.03	1.01	0.52	7.92	32.43	0.17	1.40	0.07	0.05	101.13	0.24	0.04	0.71	0.51	2.59	83.37	11.42	87.95	34.08	748.10
15R1	Px 5	56.27	0.04	1.18	0.55	8.29	31.82	0.19	1.63	0.03	0.01	100.01	0.10	0.05	0.76	0.74	3.05	82.89	12.12	87.24	31.82	776.87
15R1	Px 5	55.06	0.03	0.91	0.49	7.55	32.60	0.17	1.32	0.03	0.00	98.16	0.09	0.04	0.68	0.52	2.49	85.97	11.17	88.50	34.81	805.64
15R1	Px 5	58.20	0.03	0.99	0.54	7.60	31.48	0.19	1.31	0.03	0.00	100.37	0.10	0.03	0.75	0.56	2.45	81.80	11.08	88.07	35.42	834.42
15R1	Px 5	57.86	0.04	1.43	0.62	8.23	31.27	0.20	1.54	0.02	0.01	101.21	0.08	0.06	0.85	0.94	2.85	80.76	11.93	87.13	30.21	863.19
15R1	Px 5	57.68	0.02	0.91	0.59	7.33	32.95	0.17	1.23	0.01	0.00	100.90	0.04	0.03	0.81	0.48	2.27	84.70	10.58	88.90	39.34	891.96
15R1	Px 5	56.13	0.04	1.21	0.58	7.93	32.48	0.18	1.43	0.01	0.01	99.99	0.05	0.05	0.80	0.76	2.66	84.35	11.55	87.96	32.49	920.73
15R1	Px 5	58.28	0.02	0.98	0.55	7.49	31.34	0.20	1.31	0.04	0.01	100.21	0.12	0.03	0.76	0.53	2.46	81.59	10.93	88.18	36.14	978.28
15R1	Px 5	58.34	0.02	0.91	0.53	7.31	32.10	0.17	1.28	0.04	0.03	100.73	0.13	0.02	0.73	0.47	2.38	82.90	10.60	88.66	36.93	1007.05
15R1	Px 5	57.44	0.03	0.94	0.61	6.89	33.34	0.17	1.13	0.06	0.04	100.65	0.19	0.03	0.83	0.41	2.08	85.68	9.93	89.62	39.22	1035.83
15R1	Px 5	56.64	0.03	0.92	0.56	7.20	33.17	0.14	1.18	0.00	0.01	99.85	-0.01	0.04	0.77	0.53	2.20	85.95	10.46	89.15	37.69	1064.60

Table A.3. continues

Sample	Grain Label	SiO2 (wt%)	TiO2 (wt%)	Al2O3 (wt%)	Cr2O3 (wt%)	FeO (wt%)	MgO (wt%)	MnO (wt%)	CaO (wt%)	Na2O (wt%)	K2O (wt%)	Total (wt%)	Jade	CaTiTs	CaCrTs	CaTs	Wo	En	Fs	Mg#	Cr#	µm
15R1	Px 6	57.96	0.04	1.01	0.58	7.65	31.62	0.15	1.33	0.03	0.00	100.36	0.09	0.05	0.80	0.54	2.47	82.15	11.14	88.06	36.54	0.00
15R1	Px 6	58.03	0.03	1.03	0.62	7.57	31.61	0.18	1.32	0.03	0.01	100.43	0.10	0.04	0.86	0.54	2.45	82.06	11.02	88.16	37.67	54.36
15R1	Px 6	58.05	0.02	1.05	0.63	7.38	31.68	0.20	1.24	0.02	0.00	100.26	0.06	0.03	0.86	0.59	2.32	82.33	10.75	88.45	37.29	108.73
15R1	Px 6	58.04	0.03	0.87	0.46	7.70	31.57	0.18	1.35	0.04	0.01	100.24	0.12	0.04	0.64	0.47	2.52	82.10	11.23	87.97	34.66	163.09
15R1	Px 6	58.47	0.02	0.85	0.50	7.27	31.99	0.17	1.26	0.02	0.00	100.56	0.08	0.03	0.69	0.45	2.35	82.81	10.56	88.69	37.28	217.45
15R1	Px 6	58.01	0.03	1.02	0.56	7.68	31.36	0.16	1.36	0.01	0.01	100.19	0.05	0.04	0.77	0.60	2.54	81.68	11.22	87.92	35.37	271.82
15R1	Px 6	57.48	0.02	0.71	0.39	7.42	31.02	0.19	1.32	0.22	0.19	98.96	0.76	0.02	0.54	0.07	2.49	81.61	10.95	88.16	35.32	326.18
15R1	Px 6	56.75	0.03	0.65	0.35	7.48	30.28	0.16	1.30	0.57	0.52	98.11	1.97	0.04	0.49	-0.59	2.47	80.24	11.12	87.83	34.79	380.54
15R1	Px 6	58.40	0.03	0.61	0.37	7.59	31.59	0.18	1.32	0.03	0.00	100.11	0.10	0.04	0.51	0.29	2.48	82.26	11.08	88.13	37.78	434.91
15R1	Px 6	57.89	0.03	0.97	0.58	7.57	31.18	0.17	1.37	0.02	0.01	99.79	0.08	0.04	0.80	0.52	2.57	81.57	11.11	88.02	37.31	489.27
15R1	Px 6	57.88	0.04	0.95	0.58	7.38	31.56	0.16	1.31	0.04	0.03	99.93	0.14	0.05	0.80	0.46	2.45	82.28	10.79	88.41	37.78	543.63
15R1	Px 6	58.20	0.02	0.95	0.65	7.50	31.70	0.18	1.28	0.02	0.01	100.50	0.07	0.03	0.89	0.46	2.39	82.22	10.92	88.27	40.56	598.00
15R1	Px 6	58.14	0.03	1.04	0.55	7.70	31.28	0.17	1.40	0.04	0.02	100.37	0.14	0.04	0.76	0.58	2.61	81.36	11.24	87.86	34.81	652.36
15R1	Px 6	57.48	0.03	0.96	0.54	7.63	31.12	0.17	1.33	0.09	0.09	99.44	0.31	0.05	0.75	0.41	2.50	81.62	11.23	87.90	36.11	706.73
15R1	Px 6	58.20	0.02	0.87	0.50	7.36	31.83	0.16	1.25	0.05	0.03	100.28	0.16	0.03	0.70	0.44	2.33	82.63	10.72	88.52	36.63	761.09
15R1	Px 6	57.93	0.03	1.20	0.71	7.43	31.66	0.17	1.30	0.02	0.00	100.45	0.07	0.04	0.98	0.67	2.42	82.13	10.82	88.36	37.13	815.45
15R1	Px 6	57.81	0.04	1.05	0.61	7.54	31.26	0.17	1.31	0.13	0.11	100.02	0.43	0.05	0.85	0.39	2.45	81.48	11.02	88.09	36.87	869.82
15R1	Px 6	57.88	0.02	0.96	0.57	7.18	31.55	0.21	1.22	0.21	0.17	99.97	0.72	0.02	0.78	0.22	2.29	82.06	10.48	88.67	37.11	924.18
15R1	Px 6	57.93	0.04	1.03	0.46	8.24	31.06	0.17	1.48	0.03	0.00	100.44	0.10	0.05	0.64	0.64	2.77	80.86	12.03	87.05	30.97	978.54
15R1	Px 6	51.42	0.22	4.53	0.07	9.51	17.98	0.16	14.62	0.32	0.16	99.00	1.13	0.30	0.11	4.01	28.91	49.48	14.69	77.11	1.59	1032.91
15R1	Px 7	57.18	0.04	1.14	0.50	8.62	29.95	0.21	1.85	0.13	0.07	99.69	0.45	0.05	0.69	0.56	3.49	78.81	12.72	86.10	30.39	22.86
15R1	Px 7	56.84	0.03	1.71	0.40	9.00	29.43	0.20	1.62	0.23	0.13	99.59	0.78	0.05	0.56	1.06	3.06	77.58	13.30	85.36	19.10	45.73
15R1	Px 7	57.68	0.03	1.18	0.48	8.31	30.93	0.19	1.53	0.11	0.08	100.51	0.37	0.05	0.66	0.65	2.85	80.45	12.12	86.90	29.02	68.59
15R1	Px 7	57.80	0.03	1.23	0.45	8.64	30.71	0.21	1.60	0.09	0.03	100.79	0.31	0.03	0.63	0.76	2.99	79.79	12.60	86.36	27.04	91.45
15R1	Px 7	57.17	0.03	1.24	0.53	8.35	30.50	0.18	1.53	0.13	0.09	99.75	0.45	0.05	0.74	0.65	2.88	79.99	12.29	86.68	29.96	114.31
15R1	Px 7	57.53	0.03	1.24	0.56	8.45	30.75	0.18	1.54	0.12	0.09	100.51	0.39	0.04	0.78	0.65	2.89	80.06	12.34	86.65	31.30	137.18
15R1	Px 7	55.54	0.03	1.22	0.50	8.06	29.49	0.18	1.53	0.82	1.23	98.61	2.80	0.04	0.70	-0.53	2.90	77.78	11.93	86.71	29.26	160.04
15R1	Px 7	57.60	0.03	1.24	0.51	8.64	30.68	0.20	1.57	0.03	0.02	100.52	0.11	0.04	0.71	0.82	2.94	79.96	12.63	86.36	29.33	182.90
15R1	Px 7	56.99	0.03	1.18	0.50	8.49	30.38	0.23	1.63	0.10	0.07	99.60	0.35	0.04	0.69	0.66	3.08	79.86	12.52	86.44	29.74	205.76
15R1	Px 7	58.00	0.02	1.06	0.46	8.18	30.95	0.17	1.49	0.06	0.04	100.43	0.21	0.03	0.63	0.64	2.79	80.57	11.95	87.09	30.25	251.49
15R1	Px 7	56.20	0.05	1.85	0.34	9.57	28.59	0.20	2.23	0.29	0.13	99.47	1.01	0.07	0.48	1.13	4.25	75.69	14.21	84.19	15.59	274.35
15R1	Px 7	51.76	0.20	4.24	0.05	8.38	15.61	0.19	18.72	0.17	0.02	99.34	0.61	0.28	0.07	4.01	37.22	43.18	13.00	76.85	1.14	365.80
15R1	Px 7	49.94	0.25	5.51	0.01	12.30	13.50	0.26	16.26	0.16	0.05	98.24	0.57	0.36	0.01	5.53	33.16	38.32	19.59	66.18	0.10	388.66

Table A.3. continues

Sample	Grain Label	SiO2 (wt%)	TiO2 (wt%)	Al2O3 (wt%)	Cr2O3 (wt%)	FeO (wt%)	MgO (wt%)	MnO (wt%)	CaO (wt%)	Na2O (wt%)	K2O (wt%)	Total (wt%)	Jade	CaTiTs	CaCrTs	CaTs	Wo	En	Fs	Mg#	Cr#	µm
15R1	Px 8	46.51	0.48	12.05	0.01	14.59	7.41	0.24	16.02	0.73	0.22	98.24	2.75	0.69	0.01	11.66	33.20	21.37	23.60	47.52	0.05	12.69
15R1	Px 8	51.02	0.26	4.90	0.09	8.65	15.23	0.20	18.53	0.15	0.01	99.05	0.55	0.36	0.14	4.68	37.00	42.31	13.48	75.84	1.88	25.39
15R1	Px 8	52.93	0.15	3.34	0.15	7.66	17.52	0.20	16.95	0.18	0.06	99.14	0.63	0.21	0.22	3.01	33.52	48.20	11.82	80.30	4.30	38.08
15R1	Px 8	56.46	0.05	1.51	0.35	9.71	27.86	0.24	3.64	0.05	0.03	99.90	0.17	0.07	0.49	1.19	6.94	73.86	14.45	83.64	18.59	50.78
15R1	Px 8	55.84	0.10	5.10	0.37	8.78	22.55	0.19	5.09	0.50	0.21	98.74	1.77	0.14	0.54	4.16	9.91	61.09	13.34	82.08	6.85	63.47
15R1	Px 8	56.27	0.05	1.74	0.28	10.01	26.57	0.25	4.78	0.05	0.02	100.03	0.18	0.07	0.39	1.47	9.14	70.71	14.95	82.55	13.73	88.86
15R1	Px 8	52.45	0.17	3.60	0.12	7.35	16.81	0.18	18.50	0.15	0.03	99.35	0.53	0.24	0.18	3.32	36.57	46.23	11.34	80.30	3.27	101.56
15R1	Px 9	57.85	0.05	1.06	0.52	8.15	30.78	0.22	1.53	0.03	0.01	100.19	0.11	0.06	0.72	0.62	2.88	80.41	11.94	87.07	32.74	26.82
15R1	Px 9	58.51	0.02	1.06	0.36	8.44	30.53	0.18	1.58	0.04	0.03	100.75	0.12	0.03	0.50	0.76	2.96	79.44	12.32	86.57	25.23	80.46
15R1	Px 9	57.94	0.03	2.83	0.32	8.71	27.62	0.22	2.22	0.27	0.07	100.23	0.92	0.04	0.44	2.23	4.21	72.75	12.88	84.96	10.06	107.28
15R1	Px 9	57.49	0.03	1.00	0.47	8.15	31.51	0.20	1.54	0.04	0.02	100.45	0.15	0.04	0.65	0.58	2.87	81.85	11.87	87.33	32.21	214.56
15R1	Px 9	52.98	0.14	2.93	0.05	7.63	16.71	0.20	18.36	0.10	0.01	99.12	0.37	0.20	0.08	2.77	36.46	46.17	11.83	79.61	1.75	241.37
15R1	Px 9	47.81	0.45	8.17	0.01	11.15	11.90	0.21	18.95	0.19	0.02	98.86	0.71	0.65	0.01	8.10	38.40	33.57	17.63	65.56	0.08	268.19
2R3	Px 10	57.93	0.04	1.12	0.50	8.26	30.44	0.18	1.63	0.02	0.01	100.13	0.08	0.05	0.70	0.72	3.06	79.68	12.13	86.78	30.99	56.28
2R3	Px 10	57.95	0.02	0.96	0.50	7.79	31.20	0.17	1.44	0.02	0.01	100.05	0.08	0.03	0.69	0.58	2.70	81.42	11.40	87.72	34.18	84.43
2R3	Px 10	58.23	0.02	0.94	0.51	7.74	31.61	0.19	1.38	0.02	0.01	100.66	0.07	0.03	0.70	0.55	2.57	81.90	11.25	87.93	34.90	140.71
2R3	Px 10	58.17	0.03	0.99	0.56	7.83	31.38	0.21	1.46	0.02	0.01	100.65	0.07	0.04	0.77	0.56	2.72	81.42	11.39	87.73	35.96	168.85
2R3	Px 10	58.09	0.02	0.89	0.52	7.40	31.70	0.17	1.27	0.03	0.00	100.09	0.10	0.03	0.72	0.47	2.37	82.48	10.80	88.42	37.10	196.99
2R3	Px 10	57.93	0.04	1.10	0.58	7.87	31.11	0.20	1.58	0.02	0.01	100.44	0.07	0.06	0.81	0.63	2.95	80.95	11.49	87.57	34.78	225.13
2R3	Px 10	58.37	0.03	0.79	0.50	7.64	31.73	0.18	1.36	0.02	0.00	100.60	0.08	0.03	0.69	0.39	2.53	82.22	11.10	88.10	38.74	253.28
2R3	Px 10	58.56	0.02	0.54	0.35	7.58	31.96	0.20	1.34	0.01	0.01	100.58	0.03	0.03	0.48	0.27	2.50	82.78	11.02	88.25	39.04	281.42
2R3	Px 10	49.94	0.27	6.82	0.03	11.99	12.31	0.23	17.24	0.30	0.06	99.20	1.10	0.39	0.05	6.63	34.88	34.66	18.94	64.67	0.44	309.56
2R3	Px 10	58.02	0.02	0.86	0.40	7.94	31.36	0.20	1.50	0.03	0.01	100.33	0.10	0.03	0.55	0.53	2.80	81.59	11.58	87.57	31.67	337.70
2R3	Px 10	58.37	0.03	0.89	0.47	7.53	31.67	0.18	1.34	0.03	0.03	100.53	0.11	0.03	0.65	0.50	2.49	82.11	10.96	88.22	34.69	365.84
2R3	Px 10	58.39	0.03	0.78	0.44	7.38	31.94	0.14	1.23	0.01	0.01	100.36	0.05	0.04	0.61	0.44	2.30	82.84	10.74	88.53	36.20	393.99
2R3	Px 10	58.42	0.02	0.79	0.42	7.58	31.84	0.19	1.17	0.04	0.01	100.49	0.15	0.03	0.58	0.41	2.19	82.53	11.02	88.22	34.96	422.13
2R3	Px 10	58.53	0.02	0.58	0.34	7.60	31.72	0.17	1.39	0.04	0.01	100.41	0.12	0.03	0.47	0.27	2.60	82.33	11.07	88.15	36.79	450.27
2R3	Px 10	58.31	0.02	0.73	0.40	7.64	31.47	0.18	1.35	0.03	0.00	100.13	0.11	0.02	0.55	0.39	2.52	81.97	11.16	88.01	35.58	478.41
2R3	Px 10	58.37	0.02	0.67	0.39	7.74	31.74	0.16	1.30	0.01	0.01	100.42	0.04	0.02	0.54	0.38	2.43	82.41	11.27	87.97	36.71	506.55
2R3	Px 10	57.93	0.03	1.04	0.55	7.86	31.14	0.17	1.46	0.02	0.01	100.21	0.07	0.04	0.76	0.61	2.74	81.18	11.49	87.60	34.58	534.70
2R3	Px 10	57.80	0.03	1.09	0.54	7.98	30.91	0.19	1.50	0.01	0.00	100.06	0.04	0.04	0.74	0.70	2.82	80.77	11.70	87.35	32.86	562.84
2R3	Px 10	58.19	0.02	0.91	0.51	7.53	31.52	0.19	1.33	0.02	0.01	100.22	0.06	0.02	0.70	0.53	2.49	82.01	11.00	88.18	35.87	590.98
2R3	Px 10	57.89	0.03	1.06	0.58	7.75	31.52	0.17	1.37	0.02	0.00	100.39	0.08	0.04	0.80	0.60	2.56	81.90	11.30	87.87	35.44	619.12
2R3	Px 10	57.95	0.03	1.08	0.62	7.54	31.38	0.18	1.33	0.01	0.00	100.12	0.04	0.03	0.85	0.63	2.49	81.76	11.03	88.11	36.34	647.26
2R3	Px 10	58.20	0.02	0.87	0.51	7.40	31.84	0.16	1.22	0.01	0.01	100.24	0.02	0.02	0.70	0.51	2.28	82.71	10.79	88.46	36.63	675.40
2R3	Px 10	57.80	0.03	1.32	0.48	8.27	30.53	0.15	1.48	0.06	0.02	100.15	0.20	0.04	0.67	0.89	2.79	79.81	12.13	86.81	26.72	703.55

Table A.3. continues

Sample	Grain Label	SiO2 (wt%)	TiO2 (wt%)	Al2O3 (wt%)	Cr2O3 (wt%)	FeO (wt%)	MgO (wt%)	MnO (wt%)	CaO (wt%)	Na2O (wt%)	K2O (wt%)	Total (wt%)	Jade	CaTiTs	CaCrTs	CaTs	Wo	En	Fs	Mg#	Cr#	µm
25R2	Px 11	55.71	0.10	1.62	0.41	8.02	24.80	0.25	8.21	0.11	0.01	99.25	0.39	0.14	0.59	1.09	15.86	66.64	12.10	84.64	20.28	9.62
25R2	Px 11	52.82	0.34	3.38	0.27	7.96	17.97	0.22	15.96	0.18	0.01	99.12	0.64	0.47	0.39	2.69	31.55	49.44	12.29	80.09	7.38	19.24
25R2	Px 11	56.92	0.07	0.94	0.57	8.53	28.67	0.21	3.89	0.04	0.00	99.87	0.14	0.09	0.80	0.42	7.39	75.75	12.65	85.69	37.80	28.86
25R2	Px 11	54.35	0.17	2.14	0.51	7.39	21.70	0.23	12.39	0.13	0.00	99.01	0.46	0.23	0.74	1.47	24.21	59.01	11.27	83.96	19.35	38.49
25R2	Px 11	56.32	0.09	1.28	0.53	8.45	26.41	0.21	5.89	0.08	0.01	99.27	0.29	0.12	0.76	0.71	11.32	70.66	12.68	84.79	29.39	48.11
25R2	Px 11	49.75	0.61	6.71	0.08	8.96	13.92	0.20	18.66	0.20	0.01	99.08	0.71	0.85	0.11	6.13	37.38	38.79	14.02	73.46	1.12	57.73
25R2	Px 12	50.83	0.44	6.41	0.05	8.16	14.05	0.20	19.04	0.30	0.03	99.51	1.09	0.62	0.07	5.82	37.87	38.88	12.67	75.43	0.74	1.00
25R2	Px 12	57.36	0.06	1.24	0.78	8.04	29.79	0.21	2.63	0.04	0.01	100.16	0.13	0.08	1.08	0.60	4.96	78.11	11.82	86.86	38.48	15.71
25R2	Px 12	57.19	0.07	1.11	0.25	9.83	29.03	0.25	2.31	0.04	0.01	100.10	0.15	0.10	0.35	0.81	4.38	76.56	14.55	84.03	18.47	23.56
25R2	Px 12	56.84	0.07	1.19	0.33	9.90	28.88	0.23	2.57	0.03	0.02	100.06	0.12	0.10	0.46	0.85	4.87	76.25	14.66	83.88	21.83	31.41
25R2	Px 12	56.86	0.07	1.31	0.85	8.08	29.54	0.20	2.78	0.05	0.02	99.75	0.17	0.09	1.18	0.60	5.27	77.81	11.93	86.70	39.22	39.26
25R2	Px 12	50.13	0.52	6.74	0.07	8.63	13.68	0.18	18.66	0.22	0.02	98.85	0.79	0.73	0.11	6.26	37.47	38.22	13.52	73.87	1.06	47.12
25R2	Px 13	54.41	0.19	3.35	0.30	8.24	20.41	0.19	11.75	0.15	0.13	99.12	0.52	0.27	0.44	2.87	23.04	55.69	12.62	81.52	8.34	1.00
25R2	Px 13	57.36	0.05	1.25	0.55	8.45	27.92	0.23	3.91	0.07	0.02	99.80	0.25	0.07	0.77	0.73	7.44	73.97	12.56	85.49	30.39	9.71
25R2	Px 13	55.78	0.10	1.55	0.54	7.80	24.11	0.25	9.19	0.11	0.03	99.46	0.40	0.14	0.76	0.93	17.75	64.82	11.77	84.63	25.64	19.43
25R2	Px 13	49.98	0.46	9.24	0.04	10.47	12.21	0.20	15.91	0.29	0.33	99.12	1.04	0.65	0.06	9.03	32.05	34.21	16.46	67.52	0.45	29.14
25R2	Px 14	47.71	0.68	9.29	0.04	13.98	11.74	0.28	14.17	0.29	0.12	98.29	1.06	0.97	0.06	8.95	29.05	33.50	22.37	59.96	0.40	1.00
25R2	Px 14	53.49	0.21	2.86	0.11	7.48	19.35	0.24	14.95	0.14	0.02	98.86	0.49	0.29	0.16	2.48	29.47	53.07	11.51	82.18	3.79	10.00
25R2	Px 14	52.82	0.31	3.16	0.22	6.91	16.98	0.17	18.16	0.16	0.02	98.91	0.58	0.43	0.32	2.57	36.03	46.88	10.71	81.40	6.56	19.99
25R2	Px 14	54.53	0.14	2.14	0.75	7.05	21.17	0.22	13.55	0.15	0.01	99.70	0.53	0.20	1.08	1.28	26.34	57.27	10.70	84.26	26.05	29.99
25R2	Px 14	54.10	0.18	2.08	0.73	6.87	20.51	0.20	14.18	0.14	0.01	99.01	0.51	0.24	1.06	1.22	27.82	55.98	10.52	84.18	26.07	39.98
25R2	Px 14	53.36	0.22	2.94	0.29	7.24	18.06	0.18	15.83	0.15	0.03	98.29	0.53	0.31	0.42	2.43	31.52	50.02	11.25	81.64	8.92	49.98
25R2	Px 14	53.92	0.17	2.16	0.45	6.67	18.64	0.20	17.06	0.16	0.01	99.43	0.56	0.23	0.65	1.49	33.51	50.95	10.23	83.28	17.28	59.97
25R2	Px 14	56.26	0.09	1.32	0.49	7.96	25.65	0.23	7.61	0.09	0.01	99.71	0.30	0.12	0.70	0.77	14.60	68.47	11.92	85.18	27.11	69.97
25R2	Px 14	52.87	0.31	3.98	0.10	8.07	17.88	0.23	15.62	0.16	0.02	99.23	0.56	0.42	0.15	3.54	30.83	49.12	12.43	79.80	2.56	79.96
25R2	Px 14	51.21	0.50	12.97	0.01	12.57	7.17	0.22	12.94	0.65	0.14	98.39	2.45	0.72	0.01	12.81	26.77	20.64	20.29	50.43	0.05	89.96

[a] Grain Label: Refers to the correlated images and graphs in Figures 2.4, 2.6, and 2.8 as well as Supplemental Figure A.3.

[b] Samples: U1439C-25R-2-W 18-19 (25R2), U1439C-15R-1-W 8-10 (15R1), U1439C-19R-2-W 46-48 (19R2), U1439C-2R-3-W 2-3 (2R3).

[c] Pyroxene Quadrilateral Components: Enstatite (En), Wollastonite (Wo), Ferrosilite (Fs).

[d] Pyroxene Non-Quadrilateral Components: Jadeite (Jd), Ti-Tschermak (CaTiTs), Cr-Tschermak (CaCrTs), Ca-Tschermak (CaTs).

[e] µm= Refers to the Distance along the transect line which can be seen as the red arrow on the images in Figure A.3.

[f] Mg#=100*(Mg/(Mg+Fe)), Cr#=100*(Cr/(Cr+Al)).

Table A.4. Zoned Pyroxenes Point Analysis

Sample	SiO2 (wt%)	TiO2 (wt%)	Al2O3 (wt%)	Cr2O3 (wt%)	FeO (wt%)	MgO (wt%)	MnO (wt%)	NiO (wt%)	CaO (wt%)	Na2O (wt%)	K2O (wt%)	Total (wt%)	Jd	CaTiTs	CaCrTs	CaTs	Wo	En	Fs	Mg#
25R2-C3	56.14	0.12	0.51	1.07	8.29	32.25	0.25	0.00	3.19	0.02	0.01	101.84	0.07	0.16	1.42	-0.39	5.94	81.11	11.70	79.54
25R2-C3Z2	47.46	0.67	12.01	0.04	12.10	8.30	0.27	0.00	18.21	0.27	0.14	99.46	1.22	1.19	0.07	14.99	29.00	29.44	24.08	40.69
25R2-C7Z2	53.95	0.18	3.83	0.09	8.16	18.65	0.24	0.00	16.66	0.16	0.00	101.93	0.60	0.26	0.13	3.67	29.44	52.91	12.99	69.56
25R2-C8	56.51	0.11	1.01	0.28	9.70	30.25	0.10	0.04	2.18	0.05	0.00	100.23	0.18	0.15	0.40	0.63	3.22	80.88	14.54	75.73
25R2-C8Z1	52.21	0.53	4.11	0.17	7.95	17.69	0.10	0.01	16.19	0.21	0.03	99.19	0.79	0.79	0.26	3.48	29.29	52.22	13.17	68.98
25R2-C9	55.03	0.16	1.43	0.58	8.32	26.12	0.10	0.03	7.23	0.07	0.00	99.07	0.25	0.22	0.85	0.78	13.07	71.97	12.86	75.85
25R2-C9Z1	48.10	0.25	13.49	0.02	16.95	7.10	0.13	0.00	13.45	0.38	0.10	99.97	1.89	0.48	0.03	18.84	15.56	27.01	36.18	29.52
25R2-C10	56.57	0.00	1.27	0.51	9.60	29.99	0.12	0.04	2.88	0.04	0.00	101.02	0.14	0.00	0.71	0.91	4.44	79.53	14.27	75.76
25R2-C10Z1	53.16	0.25	3.04	0.25	7.69	18.51	0.12	0.01	17.03	0.16	0.00	100.23	0.60	0.36	0.38	2.56	31.25	52.59	12.25	70.66
25R2-C10Z2	50.17	0.35	5.88	0.05	8.24	14.70	0.10	0.01	19.66	0.24	0.00	99.39	0.92	0.52	0.07	5.93	34.84	43.91	13.81	64.08
25R2-C11	55.41	0.15	1.46	0.50	8.45	28.60	0.28	0.00	7.09	0.06	0.00	101.99	0.19	0.20	0.68	0.85	11.92	73.91	12.25	77.20
25R2-C11Z1	53.24	0.46	2.94	0.32	8.00	20.98	0.24	0.00	13.84	0.14	0.00	100.15	0.49	0.66	0.47	2.12	24.67	58.97	12.61	72.39
25R2-C11Z2	54.43	0.31	1.44	0.55	7.85	27.30	0.27	0.00	8.15	0.08	0.00	100.37	0.26	0.41	0.77	0.58	14.22	72.12	11.63	77.67
25R2-C11Z3	51.72	0.57	4.31	0.10	7.73	19.30	0.24	0.00	16.41	0.16	0.01	100.53	0.57	0.80	0.15	3.64	28.22	54.39	12.23	71.39
15R1-C1	57.15	0.00	0.97	0.50	7.82	32.52	0.06	0.00	1.22	0.03	0.00	100.27	0.09	0.00	0.70	0.61	1.61	85.46	11.53	80.61
15R1-C1Z1	49.94	0.53	6.11	0.00	10.36	14.64	0.08	0.00	19.09	0.17	0.00	100.93	0.66	0.78	0.00	5.96	32.74	42.85	17.00	58.57
15R1-C2	56.51	0.00	1.08	0.56	8.29	32.09	0.07	0.00	1.47	0.00	0.02	100.08	0.00	0.00	0.78	0.73	2.04	84.24	12.21	79.47
15R1-C2Z1	50.46	0.21	5.50	0.00	8.82	15.07	0.09	0.00	19.08	0.17	0.01	99.40	0.64	0.31	0.00	5.82	33.88	44.68	14.67	63.08
15R1-C3	55.79	0.08	0.99	0.47	8.17	33.52	0.20	0.00	1.77	0.01	0.00	100.99	0.02	0.10	0.63	0.56	2.52	84.60	11.56	80.41
15R1-C3Z1	42.03	0.96	13.76	0.00	16.13	6.89	0.29	0.00	19.32	0.30	0.04	99.72	1.33	1.63	0.00	15.95	27.66	23.11	30.33	29.94
15R1-C4	55.93	0.06	0.75	0.55	6.90	36.32	0.18	0.00	1.23	0.01	0.01	101.93	0.03	0.08	0.70	0.27	1.75	87.80	9.36	84.03
15R1-C4Z1	48.06	0.44	6.06	0.00	10.16	15.42	0.27	0.00	20.30	0.17	0.00	100.88	0.63	0.63	0.00	5.77	33.83	43.19	15.96	60.28
15R1-C5	56.80	0.06	1.07	0.56	7.05	31.16	0.09	0.09	1.73	0.09	0.01	98.69	0.30	0.09	0.81	0.51	2.50	85.01	10.78	81.56
15R1-C5Z1	50.11	0.26	5.49	0.00	9.82	14.85	0.28	0.04	17.93	0.17	0.01	98.96	0.65	0.40	0.00	5.81	31.91	44.65	16.57	60.19
15R1-C6	56.94	0.01	0.74	0.35	7.44	31.55	0.16	0.08	1.47	0.02	0.00	98.76	0.05	0.02	0.50	0.49	2.30	85.34	11.29	80.91
15R1-C6Z1	49.57	0.17	6.32	0.02	8.92	13.94	0.18	0.01	19.71	0.17	0.00	99.00	0.67	0.25	0.03	6.94	34.92	42.09	15.11	60.98
15R1-C7	56.70	0.07	1.03	0.44	7.57	31.68	0.14	0.11	1.53	0.07	0.01	99.35	0.23	0.10	0.63	0.57	2.06	85.03	11.40	80.71
15R1-C7Z1	54.96	0.04	2.03	0.36	7.48	24.25	0.19	0.04	9.70	0.09	0.00	99.15	0.34	0.05	0.54	1.77	17.42	68.10	11.78	76.42
15R1-C7Z2	47.25	0.31	6.89	0.00	11.90	11.85	0.21	0.00	19.64	0.19	0.02	98.25	0.75	0.48	0.00	7.49	34.54	36.30	20.45	49.90

Table A.4. continues

Sample	SiO2 (wt%)	TiO2 (wt%)	Al2O3 (wt%)	Cr2O3 (wt%)	FeO (wt%)	MgO (wt%)	MnO (wt%)	NiO (wt%)	CaO (wt%)	Na2O (wt%)	K2O (wt%)	Total (wt%)	Jd	CaTiTs	CaCrTs	CaTs	Wo	En	Fs	Mg#
15R1- C8	56.72	0.05	1.11	0.57	7.87	31.03	0.10	0.08	1.65	0.04	0.01	99.23	0.15	0.07	0.81	0.64	2.36	84.02	11.95	79.77
15R1- C8 Z1	51.03	0.16	4.19	0.04	8.23	15.61	0.20	0.02	18.80	0.18	0.01	98.45	0.68	0.23	0.07	4.29	34.82	46.23	13.67	65.49
15R1- C10	58.47	0.05	0.92	0.31	8.47	31.62	0.17	0.10	1.84	0.00	0.01	101.94	0.00	0.07	0.43	0.67	2.75	83.53	12.55	78.87
15R1- C10 Z2	47.81	0.56	9.01	0.06	12.81	11.39	0.26	0.00	19.97	0.01	0.01	101.89	0.06	0.86	0.10	9.86	32.75	34.56	21.80	47.07
19R2- C1	58.66	0.06	0.95	0.48	7.90	31.37	0.23	0.02	2.19	0.00	0.00	101.85	0.00	0.08	0.68	0.58	3.53	83.36	11.78	79.87
19R2- C1 Z1	49.64	0.49	7.39	0.03	8.79	13.60	0.24	0.02	20.20	0.02	0.00	100.42	0.08	0.74	0.05	8.03	35.05	41.12	14.92	60.72
19R2- C2	58.97	0.05	0.79	0.52	7.15	32.31	0.21	0.03	1.83	0.00	0.00	101.86	0.00	0.07	0.72	0.39	3.00	85.23	10.59	81.87
19R2- C2 Z1	51.47	0.45	5.29	0.04	7.38	14.89	0.20	0.01	20.22	0.00	0.00	99.96	0.00	0.68	0.07	5.51	37.07	44.34	12.33	66.87
19R2- C3 Z1	53.82	0.28	3.66	0.09	6.01	16.61	0.18	0.02	20.77	0.00	0.02	101.45	0.00	0.40	0.14	3.67	38.63	47.52	9.64	73.45
19R2- C3 Z2	51.22	0.39	6.35	0.04	7.32	14.32	0.17	0.00	21.16	0.00	0.01	101.00	0.01	0.59	0.06	6.83	37.75	42.55	12.20	66.17
19R2- C4	58.07	0.04	1.13	0.78	7.23	29.88	0.28	0.06	3.82	0.01	0.02	101.32	0.03	0.06	1.11	0.57	6.73	80.56	10.93	80.52
19R2- C4 Z1	52.08	0.49	6.03	0.08	7.42	15.16	0.21	0.00	19.89	0.01	0.00	101.36	0.04	0.74	0.12	6.27	35.43	45.04	12.37	67.14
19R2- C5	58.39	0.23	4.69	0.38	7.70	24.22	0.21	0.00	4.83	0.31	0.24	101.18	1.24	0.35	0.62	4.47	4.71	75.20	13.41	75.88
19R2- C5 Z1	50.21	0.38	6.57	0.06	7.98	14.07	0.20	0.00	20.67	0.26	0.02	100.42	1.02	0.58	0.10	6.63	36.20	42.09	13.39	63.82
19R2- C6	57.45	0.06	1.14	0.75	7.32	30.90	0.15	0.00	2.19	0.09	0.00	100.06	0.32	0.08	1.07	0.43	3.42	83.56	11.10	80.85
19R2- C6 Z1	53.02	0.31	4.33	0.15	6.81	17.15	0.23	0.00	17.89	0.20	0.04	100.12	0.75	0.47	0.23	4.10	32.61	50.59	11.26	71.59
2R3- C1	57.86	0.06	1.80	0.62	8.51	30.12	0.24	0.09	2.52	0.00	0.00	101.81	0.00	0.09	0.88	1.39	3.41	81.34	12.89	77.97
2R3- C1 Z1	51.31	0.34	5.47	0.03	9.47	14.51	0.22	0.00	19.51	0.00	0.03	100.88	0.00	0.50	0.05	5.86	35.05	42.84	15.70	60.49
2R3- C2	56.84	0.04	1.65	0.32	9.61	27.66	0.23	0.10	4.69	0.00	0.02	101.16	0.00	0.06	0.46	1.49	7.67	75.58	14.74	74.20
2R3- C2 Z1	50.51	0.34	6.81	0.02	10.25	13.82	0.23	0.01	19.71	0.00	0.02	101.72	0.00	0.51	0.03	7.45	34.02	40.96	17.04	57.42
2R3- C3 Z1	51.22	0.25	6.10	0.03	9.46	14.44	0.21	0.02	19.67	0.00	0.01	101.41	0.02	0.37	0.05	6.71	34.61	42.60	15.65	60.42
2R3- C3 Z2	45.85	0.44	12.11	0.00	16.95	9.28	0.33	0.03	14.64	0.00	0.07	99.69	0.00	0.76	0.00	15.58	19.57	31.65	32.44	35.37
2R3- C4	54.93	0.00	2.07	0.42	9.84	28.50	0.36	0.00	4.17	0.04	0.00	100.33	0.13	0.00	0.60	1.83	6.09	76.53	14.82	74.34
2R3- C4 Z1	51.65	0.00	5.06	0.09	8.24	16.59	0.23	0.00	17.49	0.11	0.00	99.47	0.43	0.00	0.14	5.63	31.10	49.04	13.66	66.82

[a] Some pyroxene core or zone analysis are missing due bad point analysis

[b] Core and Zone Labels: C#= Pyroxene core number in a sample, Z#= Zone zumber associated with a core (Z1 is in contact with the core).

[c] Samples: U1439C-25R-2-W 18-19 (25R2), U1439C-15R-1-W 8-10 (15R1), U1439C-19R-2-W 46-48 (19R2), U1439C-2R-3-W 2-3 (2R3).

[d] Pyroxene Quadrilateral Components: Enstatite (En), Wollastonite (Wo), Ferrosilite (Fs).

[e] Pyroxene Non-Quadrilateral Components: Jadeite (Jd), Ti-Tschermak (CaTiTs), Cr-Tschermak (CaCrTs), Ca-Tschermak (CaTs).

Table A.5. Zoned Olivine Transects

Sample	Grain Label	SiO2 (wt%)	TiO2 (wt%)	Al2O3 (wt%)	Cr2O3 (wt%)	FeO (wt%)	MgO (wt%)	MnO (wt%)	CaO (wt%)	Na2O (wt%)	K2O (wt%)	Total (wt%)	Fo	Fa	µm
25R2	Ol 1	42.04	0.00	0.02	0.07	9.11	47.79	0.16	0.22	0.00	0.00	99.41	90.34	9.66	23.88
25R2	Ol 1	41.93	0.00	0.02	0.07	8.89	47.89	0.15	0.19	0.02	0.00	99.17	90.57	9.43	35.82
25R2	Ol 1	42.06	0.01	0.01	0.07	8.38	48.12	0.13	0.15	0.00	0.00	98.94	91.10	8.90	47.76
25R2	Ol 1	42.16	0.00	0.02	0.10	7.92	49.15	0.13	0.13	0.01	0.01	99.61	91.71	8.29	59.71
25R2	Ol 1	42.13	0.01	0.02	0.10	7.67	49.37	0.13	0.11	0.01	0.01	99.55	91.98	8.02	71.65
25R2	Ol 1	42.64	0.00	0.47	0.08	7.85	48.00	0.13	0.19	0.02	0.04	99.42	91.59	8.41	83.59
25R2	Ol 1	42.21	0.01	0.03	0.09	8.29	48.89	0.12	0.13	0.01	0.00	99.78	91.32	8.68	95.53
25R2	Ol 1	42.32	0.01	0.02	0.10	8.88	48.66	0.13	0.13	0.00	0.00	100.27	90.71	9.29	107.47
25R2	Ol 1	42.21	0.01	0.02	0.09	9.48	48.28	0.16	0.13	0.00	0.00	100.40	90.07	9.93	119.41
25R2	Ol 1	41.53	0.01	0.01	0.07	10.13	47.35	0.15	0.13	0.01	0.01	99.40	89.29	10.71	131.35
25R2	Ol 1	41.75	0.00	0.02	0.06	10.78	46.98	0.19	0.13	0.02	0.00	99.93	88.59	11.41	143.29
25R2	Ol 1	41.14	0.01	0.02	0.07	10.63	46.95	0.17	0.16	0.00	0.00	99.15	88.74	11.26	155.23
25R2	Ol 1	41.22	0.00	0.05	0.16	10.41	46.83	0.18	0.16	0.01	0.00	99.03	88.92	11.08	167.17
25R2	Ol 1	41.68	0.00	0.02	0.05	10.27	47.50	0.15	0.16	0.00	0.00	99.84	89.18	10.82	179.12
25R2	Ol 1	41.27	0.00	0.02	0.06	11.32	46.28	0.18	0.19	0.01	0.00	99.33	87.94	12.06	191.06
25R2	Ol 2	41.55	0.01	0.08	0.06	11.64	45.04	0.20	0.20	0.02	0.02	98.83	87.34	12.66	97.15
25R2	Ol 2	41.47	0.01	0.02	0.07	9.68	46.64	0.16	0.14	0.03	0.01	98.23	89.57	10.43	113.35
25R2	Ol 2	41.83	0.01	0.17	0.04	10.92	46.27	0.17	0.19	0.01	0.02	99.64	88.31	11.69	178.11
25R2	Ol 2	41.46	0.00	0.03	0.07	10.23	46.38	0.17	0.14	0.00	0.01	98.49	88.99	11.01	194.31
25R2	Ol 2	41.77	0.01	0.02	0.07	9.28	47.60	0.12	0.13	0.01	0.01	99.02	90.14	9.86	210.50
25R2	Ol 2	42.05	0.00	0.02	0.14	8.54	47.80	0.13	0.14	0.01	0.01	98.85	90.89	9.11	226.69
25R2	Ol 2	42.11	0.00	0.03	0.10	8.09	48.46	0.12	0.12	0.03	0.01	99.07	91.44	8.56	259.07
25R2	Ol 2	41.93	0.00	0.02	0.09	8.20	47.91	0.14	0.13	0.02	0.01	98.44	91.24	8.76	275.27
25R2	Ol 2	43.54	0.00	0.70	0.10	8.76	45.69	0.13	0.24	0.14	0.11	99.39	90.29	9.71	291.46
25R2	Ol 2	42.11	0.00	0.03	0.08	8.73	48.32	0.14	0.14	0.01	0.01	99.57	90.79	9.21	307.65
25R2	Ol 2	41.84	0.00	0.03	0.09	8.98	47.74	0.15	0.15	0.00	0.00	98.98	90.46	9.54	323.84
25R2	Ol 2	41.67	0.00	0.02	0.07	9.32	47.22	0.15	0.14	0.02	0.01	98.63	90.03	9.97	340.04
25R2	Ol 2	41.55	0.01	0.03	0.06	9.87	46.69	0.14	0.14	0.01	0.01	98.51	89.40	10.60	356.23
25R2	Ol 2	41.55	0.01	0.02	0.06	10.24	46.68	0.17	0.14	0.00	0.00	98.88	89.05	10.95	388.61
25R2	Ol 2	41.59	0.00	0.02	0.07	9.79	46.98	0.15	0.15	0.02	0.01	98.79	89.53	10.47	421.00
25R2	Ol 2	41.47	0.00	0.03	0.05	11.63	46.27	0.17	0.18	0.04	0.00	99.86	87.64	12.36	437.19

Sample	Grain Label	SiO2 (wt%)	TiO2 (wt%)	Al2O3 (wt%)	Cr2O3 (wt%)	FeO (wt%)	MgO (wt%)	MnO (wt%)	CaO (wt%)	Na2O (wt%)	K2O (wt%)	Total (wt%)	Fo	Fa	µm
25R2	Ol 3	40.88	0.00	0.02	0.05	11.93	44.81	0.21	0.18	0.02	0.00	98.11	87.00	13.00	46.96
25R2	Ol 3	42.07	0.00	0.01	0.09	9.42	48.01	0.16	0.15	0.01	0.00	99.93	90.09	9.91	70.44
25R2	Ol 3	41.76	0.01	0.03	0.12	9.69	47.54	0.14	0.16	0.00	0.01	99.46	89.74	10.26	93.91
25R2	Ol 3	41.82	0.00	0.06	0.05	11.54	45.87	0.20	0.15	0.02	0.01	99.71	87.64	12.36	140.87
25R2	Ol 3	41.70	0.01	0.02	0.05	11.18	46.37	0.17	0.15	0.00	0.00	99.65	88.09	11.91	211.31
25R2	Ol 3	42.15	0.01	0.06	0.05	10.79	46.61	0.16	0.18	0.01	0.01	100.03	88.51	11.49	234.79
25R2	Ol 3	41.41	0.01	0.01	0.04	11.03	45.88	0.19	0.16	0.05	0.02	98.80	88.12	11.88	281.74
25R2	Ol 3	41.57	0.01	0.01	0.05	10.19	46.85	0.15	0.15	0.01	0.01	99.01	89.13	10.87	328.70
25R2	Ol 3	41.64	0.00	0.03	0.09	9.68	47.15	0.14	0.15	0.02	0.01	98.90	89.67	10.33	352.18
25R2	Ol 3	41.72	0.01	0.02	0.10	9.25	47.48	0.15	0.15	0.00	0.01	98.89	90.15	9.85	375.66
25R2	Ol 3	41.66	0.00	0.02	0.09	9.33	47.23	0.15	0.14	0.00	0.00	98.62	90.02	9.98	399.14
25R2	Ol 3	41.46	0.01	0.19	0.07	11.92	45.09	0.17	0.20	0.01	0.02	99.13	87.09	12.91	422.62
25R2	Ol 4	41.48	0.00	0.10	0.09	11.18	45.80	0.20	0.19	0.02	0.02	99.09	87.95	12.05	10.70
25R2	Ol 4	41.77	0.00	0.01	0.14	11.08	46.39	0.18	0.17	0.02	0.01	99.76	88.18	11.82	21.41
25R2	Ol 4	41.25	0.00	0.02	0.13	12.84	44.64	0.20	0.17	0.01	0.01	99.27	86.11	13.89	32.11
25R2	Ol 4	41.32	0.01	0.02	0.05	12.00	45.63	0.18	0.15	0.00	0.01	99.37	87.15	12.85	64.22
25R2	Ol 4	41.19	0.01	0.01	0.05	12.28	45.10	0.19	0.17	0.03	0.01	99.03	86.75	13.25	74.92
25R2	Ol 4	41.09	0.00	0.02	0.04	12.58	44.98	0.20	0.17	0.01	0.01	99.10	86.44	13.56	96.33
25R2	Ol 4	41.40	0.00	0.01	0.09	10.64	46.35	0.17	0.17	0.03	0.01	98.88	88.59	11.41	107.03
25R2	Ol 4	41.88	0.01	0.03	0.07	10.69	47.51	0.19	0.17	0.02	0.00	100.57	88.79	11.21	117.74
25R2	Ol 5	42.37	0.01	0.28	0.04	10.26	45.30	0.16	0.22	0.03	0.04	98.71	88.72	11.28	10.37
25R2	Ol 5	44.66	0.13	3.97	0.07	9.31	35.21	0.16	5.89	0.27	0.03	99.71	87.09	12.91	20.74
25R2	Ol 5	41.60	0.02	0.02	0.07	10.22	46.83	0.15	0.18	0.00	0.00	99.09	89.09	10.91	31.12
25R2	Ol 5	41.52	0.00	0.09	0.04	10.85	45.90	0.18	0.22	0.03	0.02	98.86	88.29	11.71	41.49
25R2	Ol 5	41.59	0.00	0.04	0.05	10.58	46.74	0.20	0.18	0.01	0.01	99.40	88.74	11.26	51.86
25R2	Ol 5	41.71	0.01	0.02	0.04	10.49	46.95	0.18	0.20	0.01	0.01	99.62	88.86	11.14	62.23
25R2	Ol 5	41.73	0.00	0.02	0.05	10.46	46.89	0.16	0.20	0.01	0.00	99.52	88.88	11.12	72.60
25R2	Ol 5	41.70	0.01	0.02	0.04	10.38	46.84	0.17	0.20	0.01	0.01	99.37	88.94	11.06	82.97
25R2	Ol 5	41.75	0.01	0.02	0.05	10.65	47.05	0.18	0.19	0.01	0.00	99.90	88.74	11.26	93.35
25R2	Ol 5	41.62	0.00	0.01	0.05	10.74	46.64	0.14	0.19	0.01	0.01	99.42	88.56	11.44	103.72
25R2	Ol 5	41.33	0.00	0.02	0.04	10.97	45.97	0.18	0.18	0.02	0.01	98.72	88.19	11.81	114.09
25R2	Ol 5	41.44	0.00	0.01	0.05	11.02	46.36	0.17	0.19	0.01	0.00	99.25	88.23	11.77	124.46
25R2	Ol 5	41.70	0.00	0.02	0.09	9.38	47.35	0.17	0.15	0.00	0.00	98.86	90.00	10.00	145.20

Table A.5. continues

Sample	Grain Label	SiO2 (wt%)	TiO2 (wt%)	Al2O3 (wt%)	Cr2O3 (wt%)	FeO (wt%)	MgO (wt%)	MnO (wt%)	CaO (wt%)	Na2O (wt%)	K2O (wt%)	Total (wt%)	Fo	Fa	µm
25R2	Ol 6	41.36	0.00	0.02	0.06	10.98	46.01	0.16	0.14	0.00	0.01	98.75	88.19	11.81	92.44
25R2	Ol 6	41.31	0.01	0.35	0.04	13.07	43.29	0.19	0.20	0.02	0.10	98.59	85.51	14.49	103.99
25R2	Ol 6	41.58	0.01	0.02	0.06	10.16	47.49	0.15	0.14	0.00	0.00	99.63	89.28	10.72	127.10
25R2	Ol 6	41.72	0.02	0.01	0.05	9.29	47.80	0.15	0.15	0.02	0.00	99.22	90.17	9.83	138.66
25R2	Ol 6	41.94	0.00	0.01	0.07	8.78	48.11	0.14	0.15	0.02	0.01	99.24	90.71	9.29	150.21
25R2	Ol 6	41.72	0.00	0.03	0.07	8.71	47.96	0.14	0.15	0.02	0.01	98.81	90.75	9.25	161.77
25R2	Ol 6	41.81	0.00	0.02	0.07	8.74	47.86	0.13	0.15	0.01	0.00	98.79	90.70	9.30	173.32
25R2	Ol 6	41.79	0.00	0.03	0.05	8.81	48.21	0.15	0.15	0.00	0.01	99.20	90.70	9.30	184.88
25R2	Ol 6	41.94	0.00	0.02	0.06	8.83	48.05	0.13	0.15	0.00	0.00	99.20	90.65	9.35	196.43
25R2	Ol 6	41.58	0.00	0.01	0.05	8.84	47.70	0.12	0.16	0.02	0.00	98.48	90.58	9.42	207.99
25R2	Ol 6	41.67	0.00	0.02	0.06	9.36	47.47	0.13	0.13	0.01	0.01	98.87	90.04	9.96	219.54
25R2	Ol 6	42.50	0.00	0.73	0.04	12.24	43.56	0.18	0.25	0.05	0.15	99.70	86.38	13.62	254.21
25R2	Ol 6	41.12	0.00	0.59	0.06	10.82	46.41	0.19	0.27	0.10	0.14	99.71	88.43	11.57	265.76
25R2	Ol 6	40.55	0.00	0.12	0.05	11.92	45.89	0.19	0.28	0.04	0.01	99.04	87.28	12.72	277.32
25R2	Ol 6	41.30	0.00	0.02	0.05	10.94	46.05	0.17	0.18	0.02	0.00	98.73	88.24	11.76	288.87
25R2	Ol 6	41.21	0.00	0.19	0.05	10.85	45.26	0.15	0.23	0.03	0.05	98.02	88.14	11.86	311.98

Table A.5. continues

[a] Grain Label: Refers to the correlated images and graphs in Figure A.5 and Supplemental Figures A.4 & A.5.

[b] Samples: U1439C-25R-2-W 18-19 (25R2).

[c] Olivine End-member Components: Forsterite (Fo), Fayalite (Fa).

[d] µm= Refers to the Distance along the transect line which can be seen as the red arrow on the images in Figure A.4.

Date

Name

Address

Dear Ciprian Stremtan:

I am in the process of preparing my thesis in the Geoscience department at Utah State University. I hope to complete my degree program in Geology. I am requesting your permission to include the attached material as shown. I will include acknowledgments and/or appropriate citations to your work as shown and copyright and reprint rights information in a special appendix. Please advise me of any changes you require. Please indicate your approval of this request by signing in the space provided, attaching any other form or instruction necessary to confirm permission. If you have any questions, please call me at the number below.

Thank you for your cooperation,

Jesse Scholpp

813-766-6629

I hereby give permission to Jesse Scholpp to reprint the following material in his thesis.

(Petrologic Evolution Of Boninite Lavas From The IBM Fore-Arc, IODP Expedition 352: Evidence For Open-System Processes During Early Subduction Zone Magmatism)

Signed: _____

Date 14.7.2020

Name Martin Rittner

Address TOFWERK AG, Schorenstrasse 39, 3645 Thun, Switzerland

Dear Martin Rittner:

I am in the process of preparing my thesis in the Geoscience department at Utah State University. I hope to complete my degree program in Geology. I am requesting your permission to include the attached material as shown. I will include acknowledgments and/or appropriate citations to your work as shown and copyright and reprint rights information in a special appendix. Please advise me of any changes you require. Please indicate your approval of this request by signing in the space provided, attaching any other form or instruction necessary to confirm permission. If you have any questions, please call me at the number below.

Thank you for your cooperation,

Jesse Scholpp

813-766-6629

I hereby give permission to Jesse Scholpp to reprint the following material in his thesis.

(Petrologic Evolution Of Boninite Lavas From The IBM Fore-Arc, IODP Expedition 352: Evidence For Open-System Processes During Early Subduction Zone Magmatism)

Signed: _____

July 13, 2020

Antonio J. Luna
1103 Soaring Osprey Way
Valrico, FL 33594

Dear Antonio Luna:

I am in the process of preparing my thesis in the Geoscience department at Utah State University. I hope to complete my degree program in Geology. I am requesting your permission to include the attached material as shown. I will include acknowledgments and/or appropriate citations to your work as shown and copyright and reprint rights information in a special appendix. Please advise me of any changes you require. Please indicate your approval of this request by signing in the space provided, attaching any other form or instruction necessary to confirm permission. If you have any questions, please call me at the number below.

Thank you for your cooperation,

Jesse Scholpp

813-766-6629

I, Antonio Luna, hereby give permission to Jesse Scholpp to reprint the following material in his thesis.

(Petrologic Evolution of Boninite Lavas from the IBM Fore-Arc, IODP Expedition 352: Evidence for Open-System Processes during Early Subduction Zone Magmatism)

Signed: _____ Date: July 13, 2020

Printed: Antonio Luna

Date

Name

Address

Dear Stephen Hill:

I am in the process of preparing my thesis in the Geoscience department at Utah State University. I hope to complete my degree program in Geology. I am requesting your permission to include the attached material as shown. I will include acknowledgments and/or appropriate citations to your work as shown and copyright and reprint rights information in a special appendix. Please advise me of any changes you require. Please indicate your approval of this request by signing in the space provided, attaching any other form or instruction necessary to confirm permission. If you have any questions, please call me at the number below.

Thank you for your cooperation,

Jesse Scholpp

813-766-6629

I hereby give permission to Jesse Scholpp to reprint the following material in his thesis.

(Petrologic Evolution Of Boninite Lavas From The IBM Fore-Arc, IODP Expedition 352: Evidence For Open-System Processes During Early Subduction Zone Magmatism)

Signed:

Date

Name

Address

Dear Zachary Atlas:

I am in the process of preparing my thesis in the Geoscience department at Utah State University. I hope to complete my degree program in Geology. I am requesting your permission to include the attached material as shown. I will include acknowledgments and/or appropriate citations to your work as shown and copyright and reprint rights information in a special appendix. Please advise me of any changes you require. Please indicate your approval of this request by signing in the space provided, attaching any other form or instruction necessary to confirm permission. If you have any questions, please call me at the number below.

Thank you for your cooperation,

Jesse Scholpp

813-766-6629

I hereby give permission to Jesse Scholpp to reprint the following material in his thesis.

(Petrologic Evolution Of Boninite Lavas From The IBM Fore-Arc, IODP Expedition 352: Evidence For Open-System Processes During Early Subduction Zone Magmatism)

Signed: _____ 7/10/20

Zachary D. Atlas, Ph.D.

Date 10 Jul 20

Name Bradford Mack

Address 3463 High Hampton Cir,
Tampa, FL 33610

Dear Bradford Mack:

I am in the process of preparing my thesis in the Geoscience department at Utah State University. I hope to complete my degree program in Geology. I am requesting your permission to include the attached material as shown. I will include acknowledgments and/or appropriate citations to your work as shown and copyright and reprint rights information in a special appendix. Please advise me of any changes you require. Please indicate your approval of this request by signing in the space provided, attaching any other form or instruction necessary to confirm permission. If you have any questions, please call me at the number below.

Thank you for your cooperation,

Jesse Scholpp

813-766-6629

I hereby give permission to Jesse Scholpp to reprint the following material in his thesis.

(Petrologic Evolution Of Boninite Lavas From The IBM Fore-Arc, IODP Expedition 352: Evidence For Open-System Processes During Early Subduction Zone Magmatism)

Signed: 10 Jul 20